

# Modelling of a monostatic borehole radar antenna



*Thesis presented in partial fulfilment of the requirements for the degree  
**Master of Science in Engineering (Electronic Engineering  
with Computer Science)** in the Department of Electrical and  
Electronic Engineering at the University of Stellenbosch.*

Supervisors:

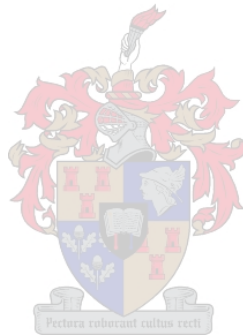
Prof. J. H. Cloete and Prof. K. D. Palmer

April 2006

– Declaration –

“I, the undersigned, hereby declare that the work contained in this thesis is my own original work, unless stated otherwise, and that I have not previously, in its entirety or in part, submitted it at any university for a degree.”

.....  
Marcel Gouws  
March 9, 2006



# Abstract

The successful operation of a pulsed monostatic borehole radar system requires that current on the antenna due to transmitter pulses subsides quickly. Deterioration of the radar antenna feed-point current settling times when deployed in water-filled boreholes showed that the radar system's performance is highly environmentally sensitive. Electromagnetic models are used to investigate this effect, since measuring the feed-point and radiative characteristics of an insulated antenna deployed in a borehole is practically impossible at present.

A transmission line model for insulated antennas is utilized to model the borehole radar antenna in electrically dense media. Predicted input impedance values however do not correspond well to those from numerical field simulation software and the model is shown to be inadequate for modelling insulated antennas in environments of low conductivity. Radiated field results are however found to be accurate.

A study of the feed-point and radiative characteristics of the borehole radar antenna in a range of different borehole environment is performed using electromagnetic field simulation software. Results confirm that the borehole radar antenna has longer feed-point current settling times and degraded radiated pulse waveforms when deployed in water-filled boreholes.

Simple lumped element networks with driving-port impedances approximately equal to antenna input impedances are synthesized from simulated input impedance results for a range of borehole environments. This allows diagnostics on the radar system to be performed in the laboratory, with the antenna load appearing as if the system were deployed in a borehole.

The use of an antenna with distributed resistive *and* capacitive loading is proposed as a modification that would result in improved feed-point characteristics in water-filled boreholes. Results from simulations and experiments are presented that confirm that the new antenna design substantially reduces feed-point current settling times after the transmitter fires.

# Opsomming

Die werking van 'n monostatiese boogtradarstelsel berus daarop dat die stroom op die antenna vanweë senderpulsse vinnig moet wegsterf. Verlengde wegsterftye van die antenna voerpuntstroom word waargeneem wanneer die antenna in watergevulde boogate ontplooi word, en die stelsel is gevolglik grootliks omgewings sensitief. Elektromagnetiese modelle word aangewend om laasgenoemde effek te ondersoek, siende dat meting van die voerpunt- en stralingseienskappe van die antenna tans onmoontlik is wanneer die stelsel in 'n boogate ontplooi is.

'n Transmissielynmodel van geïsoleerde antennas word aangewend om die boogtradarantenna te modelleer in elektries digte media. Die voorspelde intree-impedansie stem egter nie goed ooreen met waardes vanaf numeriese simulasië programmatuur nie en daar word getoon dat die model nie geskik is vir die modellering van geïsoleerde antennas in omgewings van lae geleidingsvermoë nie. Stralingsveld resultate van die model is egter akkuraat.

'n Studie word gemaak van die voerpunt- en stralingseienskappe van die antenna in 'n reeks van boogatomgewings deur middel van die gebruik van numeriese simulasië programmatuur. Resultate verifieer dat die wegsterftye van die antenna se voerpuntstroom langer is in water-gevulde boogate.

Puntelementnetwerke met voerpuntimpedansies benaderd gelyk aan die antenna intree-impedansie word gesintetiseer vanaf gesimuleerde intree-impedansie resultate vir 'n reeks boogatomgewings. Die netwerke laat toe dat die stelsel in die laboratorium ontleed kan word met 'n antennalase wat vertoon asof die stelsel in 'n boogate ontplooi is.

Die gebruik van 'n antenna met resistiewe *en* kapasitiewe belading word voorgestel as 'n modifikasie wat die antenna se voerpunteienskappe in water-gevulde boogate sal verbeter. Resultate van simulasië en eksperimente word gebied wat aantoon dat die nuwe antenna-ontwerp die wegsterftye van die voerpuntstroom beduidend verminder.

# Contents

<b>Abstract</b>	<b>ii</b>
<b>Opsomming</b>	<b>iii</b>
<b>1 Introduction</b>	<b>1</b>
1.1 Background . . . . .	1
1.2 Overview of the monostatic BHR system . . . . .	2
1.3 Limitations of the monostatic BHR . . . . .	7
1.4 Thesis outline . . . . .	8
<b>2 Electromagnetic modelling of the BHR antenna</b>	<b>9</b>
2.1 Introduction . . . . .	9
2.2 Simulation models . . . . .	10
2.2.1 CST Microwave Studio . . . . .	10
2.2.2 FEKO . . . . .	12
2.2.3 Comparison of simulation packages . . . . .	15
2.3 The transmission line model of insulated antennas . . . . .	17
2.3.1 Formulation of transmission line parameters . . . . .	17
2.3.2 Current distribution, input impedance and far field . . . . .	22
2.3.3 Evaluation of WKG model . . . . .	25
2.3.4 Evaluation of Chen and Warne's model . . . . .	25
2.4 Conclusions . . . . .	29
<b>3 Parametrical studies</b>	<b>32</b>
3.1 General comments on current distribution . . . . .	33
3.2 Input impedance . . . . .	35
3.3 Feed-point current . . . . .	37
3.3.1 Feed-point current recovery . . . . .	37
3.3.2 Output voltage recovery . . . . .	41
3.4 Radiated field . . . . .	44
3.5 Conclusions . . . . .	48

<b>4</b>	<b>Feed-point models</b>	<b>49</b>
4.1	Introduction . . . . .	49
4.2	Driving-port impedance synthesis methods . . . . .	50
4.2.1	Complex curve fitting of input impedance data . . . . .	50
4.2.2	Positive real rational functions . . . . .	51
4.2.3	Overview of synthesis from arbitrary impedance functions . . . . .	52
4.2.4	Synthesis of RC impedances . . . . .	56
4.3	Lumped element models for a range of different borehole environments . . . . .	58
4.3.1	Equivalent circuits for water-filled boreholes . . . . .	59
4.3.2	Equivalent circuits for air-filled boreholes . . . . .	61
4.4	Evaluation of synthesized networks . . . . .	62
<b>5</b>	<b>Improved linear impedance loaded antennas for water-filled boreholes in hard rock</b>	<b>65</b>
5.1	Introduction . . . . .	65
5.2	The Wu-King non-reflecting impedance loading profile . . . . .	67
5.2.1	Profile definition . . . . .	67
5.2.2	The complex expansion parameter $\Psi$ . . . . .	69
5.2.3	Wu-King profiles for wide-band applications . . . . .	70
5.2.4	Feed-point characteristics . . . . .	70
5.2.5	Level of loading on the borehole antenna . . . . .	72
5.3	Feed-point characteristics of Wu-King dipoles in electrically dense media . . . . .	72
5.3.1	Wu-King dipoles designed for electrically dense media . . . . .	73
5.3.2	The free space Wu-King dipole in electrically dense media . . . . .	75
5.3.3	Inadequacy of the resistive Wu-King profile . . . . .	79
5.4	The resistive/capacitive Wu-King dipole as a loading profile for electrically dense media . . . . .	79
5.5	Design of a resistive/capacitive loading profile for an insulated borehole antenna . . . . .	82
5.5.1	The Wu-King profile modified for insulated antennas . . . . .	82
5.5.2	A Wu-King profile for a cylindrically stratified medium . . . . .	84
5.5.3	Practical design considerations . . . . .	87
5.6	Evaluation of the resistive/capacitive profile . . . . .	88
5.6.1	Simulations . . . . .	89
5.6.2	Field experiments . . . . .	94
5.6.3	Conclusions . . . . .	98
<b>6</b>	<b>Conclusions and future work</b>	<b>100</b>
6.1	Conclusions . . . . .	100

6.2 Future work . . . . .	101
<b>Bibliography</b>	<b>103</b>
<b>A Borehole antenna geometry</b>	<b>106</b>
<b>B Transmission line model derivations</b>	<b>110</b>
B.1 Exact solution . . . . .	110
B.1.1 Electromagnetic field of the insulated antenna . . . . .	110
B.1.2 Transmission line parameters . . . . .	113
B.2 Approximate field solution . . . . .	115
B.2.1 Approximate electromagnetic field of the insulated antenna . . . . .	115
B.2.2 Transmission line parameters . . . . .	117
B.3 Combined effects of multiple insulation layers . . . . .	118
<b>C Current distribution on an insulated dipole</b>	<b>120</b>
<b>D Current distribution on a general insulated antenna</b>	<b>122</b>
<b>E The radiated field of a general insulated antenna</b>	<b>124</b>
<b>F Failure of Chen and Warne's transmission line model</b>	<b>126</b>
<b>G The scaled Wu-King impedance profile</b>	<b>129</b>
<b>H A non-reflecting impedance loading profile for insulated antennas</b>	<b>131</b>

# List of Figures

1.1	Schematic representation of the monostatic radar system . . . . .	2
1.2	A simplified schematic of the monostatic BHR transmitter configuration . . . . .	3
1.3	Measured voltage across the antenna feed-point as the transmitter fires . . . . .	3
1.4	Transfer function of the T/R-switch in through-mode . . . . .	4
1.5	Input impedance of the T/R-switch in through mode, terminated in a 200 $\Omega$ resistor . . . . .	4
1.6	A schematic of the monostatic BHR receiver gain stage . . . . .	5
1.7	Time dependent total gain of the gain stage . . . . .	5
1.8	A typical deployment configuration for the monostatic radar probe . . . . .	6
1.9	Experimental radar traces from air-filled and water-filled boreholes with diameter 75 mm . . . . .	8
2.1	Longitudinal cross-section of the borehole antenna model implemented in CST Microwave Studio . . . . .	11
2.2	Details of CST Microwave Studio model feedpoint section using coaxial feed . . . . .	12
2.3	Geometry of the two-layer and single layer insulated conductors, mathematically equivalent by equation 2.1 . . . . .	14
2.4	Details of the borehole antenna model implemented in FEKO . . . . .	14
2.5	Comparison of input impedance and directivity of the BHR antenna obtained with CST Microwave Studio and FEKO . . . . .	16
2.6	Longitudinal and axial cross-sections of the assumed geometry of the coaxial transmission line model of the insulated antenna . . . . .	18
2.7	Equivalent circuits for the transmission line model of insulated antennas . . . . .	20
2.8	The insulated dipole antenna and its equivalent transmission line model . . . . .	23
2.9	The borehole radar antenna and its equivalent transmission line model . . . . .	24
2.10	Comparison of input impedance from the WKG model and FEKO of the BHR antenna in water . . . . .	26
2.11	Comparison of input impedance from Chen and Warne's model with that of FEKO for an insulated dipole antenna in different ambient media . . . . .	27
2.12	Comparison of input impedance from Chen and Warne's model with that of FEKO for an insulated dipole antenna with different insulation diameters . . . . .	28

2.13	Comparison of input impedance from Chen and Warne's model with that of FEKO for the BHR antenna in different borehole environments . . . . .	30
2.14	Comparison of borehole antenna directivity predicted by FEKO and the transmission line model of insulated antennas . . . . .	31
3.1	The CST Microwave Studio model of the BHR antenna inside a borehole . . . . .	32
3.2	The current distribution simulated in CST Microwave Studio for an air-filled borehole and a water-filled borehole both of diameter 75 mm . . . . .	34
3.3	Input impedance of the borehole radar antenna in air-filled boreholes of varying diameter . . . . .	36
3.4	Input impedance of the borehole radar antenna in water-filled boreholes of varying diameter . . . . .	36
3.5	Input impedance of the borehole radar antenna in 75 mm diameter air-filled and water-filled boreholes with differing water conductivity . . . . .	37
3.6	The simplified model of the BHR receiver circuit in ADS . . . . .	38
3.7	Recovery of current after transmitter firing for 75 mm air-filled and water-filled boreholes . . . . .	39
3.8	Recovery of current after transmitter firing for selected air-filled boreholes . . . . .	40
3.9	Recovery of current after transmitter firing for selected water-filled boreholes . . . . .	40
3.10	Recovery of the instantaneous power at the feed-point for selected water-filled boreholes . . . . .	41
3.11	A schematic of the gain stage after the T/R-switch . . . . .	41
3.12	The total time-dependent gain of the amplifier stage . . . . .	42
3.13	Simulated radar traces for 75 mm air- and water-filled boreholes . . . . .	43
3.14	Measured and simulated drain voltage . . . . .	45
3.15	Radiated electric field at a distance of 10 m at broadside for selected air-filled boreholes from CST Microwave Studio simulations . . . . .	45
3.16	Radiated electric field at broadside of selected water-filled boreholes . . . . .	46
3.17	Radiated electric field at broadside of a 75 mm air-filled and a water-filled boreholes . . . . .	47
3.18	Variation of directivity with frequency in 75 mm air-filled and water-filled boreholes . . . . .	47
3.19	Variation of directivity with borehole diameter at a given frequency . . . . .	48
4.1	Comparison of fitted curves using different order impedance functions . . . . .	51
4.2	Realization of series or shunt branches as a single step in iterative order reduction . . . . .	53
4.3	Series impedance branches realized by removing poles at $s = 0$ , $s = \infty$ and $s = \pm j\omega_i$ from an impedance function . . . . .	54

4.4	Series impedance branches realized by removing poles at $s = 0$ , $s = \infty$ and $s = \pm j\omega_i$ from an admittance function . . . . .	54
4.5	Network corresponding to the Foster 2 expansion of an RC admittance . . . . .	58
4.6	Network synthesized using a 3 <sup>rd</sup> order impedance function . . . . .	60
4.7	Network synthesized using a 2 <sup>nd</sup> order impedance function . . . . .	61
4.8	Comparison of input impedance and feed-point discharge current from the synthesized antenna load and the simulated load for an air- and water-filled 75 mm borehole . . . . .	63
4.9	Comparison of current measured with an experimental current probe in 150 mm water-filled borehole with simulations using synthesized load . . . . .	64
5.1	The simplified model of the antenna receiver circuit in ADS with the implemented high-pass filter at the feed-point . . . . .	66
5.2	Characteristics of the feed-point current filter . . . . .	66
5.3	Real and imaginary parts of $\Psi$ for $h = 0.6$ m and $a = 1.5$ mm . . . . .	69
5.4	Comparison of RC approximation to input impedance with that of the MoM FEKO model for Wu-King dipole with $h = 0.6$ m and $a = 1.5$ mm in free space . . . . .	71
5.5	Input impedance of Wu-King dipoles in different media from FEKO MoM calculations . . . . .	73
5.6	Feed-point current step response of resistive Wu-King dipoles in different ambient media computed numerically from simulated input admittance data . . . . .	74
5.7	Comparison of approximations to input impedance of the free space Wu-King dipole of dimensions $h = 0.6$ m and $a = 1.5$ mm in free space and dense media with corresponding results from the FEKO MoM model . . . . .	77
5.8	Comparison of the free space Wu-King dipole input impedance in $\epsilon_r = 4$ and $\epsilon_r = 9$ with that of correctly designed Wu-King dipoles for the corresponding media from FEKO MoM calculations . . . . .	78
5.9	The feed-point current step response of a free space Wu-King dipole in $\epsilon_r = 4$ and 9 in comparison with Wu-King dipoles designed for the respective media computed numerically with ADS from input impedance data . . . . .	78
5.10	Comparison of feed-point characteristics of resistive/capacitive free space Wu-King dipoles to a resistive free space Wu-King dipole in media with $\epsilon_r = 1, 4$ and 9, from FEKO MoM and ADS simulations . . . . .	81
5.11	The effective relative permittivity corresponding to the propagation speed of zeroth order current waves along the borehole antenna loaded arm in several borehole environments . . . . .	84
5.12	The required resistive loading at $z = 0$ for the borehole antenna loaded arm in homogeneous rock ( $\epsilon_{r4} = 9$ ) and homogeneous water ( $\epsilon_{r4} = 81$ ) . . . . .	85

5.13	Comparison of the required loading at $z = 0$ for the homogeneous and stratified Wu-King profiles for a insulated dipole with the cross-sectional geometry of the borehole antenna loaded arm and $h = 0.6$ m in homogeneous rock ( $\epsilon_r = 9$ ) . . . . .	86
5.14	Comparison of borehole antenna input impedance with different impedance loading profiles from CST Microwave Studio simulations . . . . .	90
5.15	Comparison of borehole antenna feed-point current discharge curves for different impedance loading profiles shown in linear and logarithmic scales . . . . .	92
5.16	Comparison of borehole antenna gain patterns for different impedance loading profiles in different borehole environments . . . . .	95
5.17	Comparison of borehole antenna time-domain radiated electric field at broadside at a range of 10 m for differing loading profile for 75 mm air- and water-filled boreholes . . . . .	96
5.18	Radar traces from the SRGT09 borehole for the resistive and 400% R/C antenna configurations . . . . .	97
5.19	Radar traces from the Finch 304 borehole for the different antenna configurations . . . . .	98
5.20	Comparison of the quality of the radar data obtained using the feed-point current filter implementation with that using the R/C antenna from the 75 mm water-filled borehole F304 at De Beers Finsch Diamond Mines . . . . .	99
A.1	The monostatic borehole radar system with and without PVC casing . . . . .	106
A.2	Detail of the loaded arm near the feed-point with insulation layers cut open . . . . .	107
A.3	A longitudinal cross-section of the modeled BHR antenna . . . . .	107
A.4	Detail of the longitudinal cross-section of the loaded arm . . . . .	107
A.5	Cross sections of the loaded and conductive antenna arms . . . . .	108
B.1	Circular cylindrical coordinate system . . . . .	111

# List of Tables

- 3.1 Simulated recovery times in different borehole environments . . . . . 43
- 4.1 Elements values in Figure 4.6 for a water-filled borehole . . . . . 60
- 4.2 Elements values in Figure 4.7 for a water-filled borehole . . . . . 60
- 4.3 Elements values in Figure 4.7 for an air-filled borehole . . . . . 61
- 5.1 Proposed loading profiles for the insulated borehole antenna . . . . . 88
- 5.2 Recovery times for antennas with different loading profiles in several borehole environments . . . . . 93
- A.1 The resistor values and positions for the 12-element discrete implementation of the resistive Wu-King loading profile . . . . . 108



# Chapter 1

## Introduction

### 1.1 Background

Ground penetrating radar (GPR) refers to the use of electromagnetic radiation in the radio and microwave bands to detect subsurface structures without physically probing the ground surface. Borehole radar (BHR) is a specialized form of GPR where transmission and reception of radar signals occur below the surface, utilizing antennas positioned inside boreholes drilled into the host rock of interest. The primary application of BHR is in the mining industry, where it is establishing itself as a promising tool in geophysical exploration, greatly extending other survey techniques.

Accurate delineation of ore bodies and potentially hazardous structures such as fractures and faults increases the efficiency and safety of a mining operation. With prior knowledge of the position of an ore body and where it is disrupted, mining activities may be planned ahead to reach the targeted ore body in the most economical manner. Risk of accidents may be reduced with advance knowledge of the positions of hazardous geological structures through adequate planning before such a structure is encountered.

The radar system studied in this project is one operated by Geomole Pty Ltd<sup>1</sup> for use in geophysical surveys. The first radar operated by Geomole was a bistatic system pioneered by Claassen [5] and Hargreaves [10] at Oxford University in early 1990's. The bistatic radar could previously be partitioned into 5 subsystems: the transmitter (Tx) probe, the receiver (Rx) probe, a fibre-optic spacer section connecting the Tx and Rx probes, a surface located data acquisition (DAQ) system and a fibre-optic cable connecting the latter with the Rx probe<sup>2</sup>.

The deployment of the system was a cumbersome process. Conducting measurements

---

<sup>1</sup>[www.geomole.com](http://www.geomole.com)

<sup>2</sup>The DAQ subsystem has since been integrated into the Rx probe, eliminating the need for the surface located DAQ and the fibre-optic cable.

required the transportation and setup of a large amount of equipment. The optical connectors utilized in the system were sensitive to dirt and mechanical misalignment. The use of the surface located DAQ and the optical spacer section furthermore complicated the setup and operation of the system.

The survey tool clearly needed to be simplified for its use to become established in the mining industry. A proposed simplification was the co-location of the Tx and Rx subsystems in a single probe with both systems sharing the antenna – hence, the design of a monostatic radar. Subsequent investigations by P. J. vd Merwe [27] and B. K. Woods [30] contributed to the development of the first monostatic BHR survey tool. A short overview of the monostatic BHR system as it was at the start of this project is given in the following section.

## 1.2 Overview of the monostatic BHR system

The monostatic BHR system may be described as an ultra wide band, VHF (10 MHz – 100 MHz), pulsed radar. It may be partitioned into four subsystems: a transmitter block, receiver block, T/R-switch and an antenna, interconnected as illustrated diagrammatically in Figure 1.1. The systems operates at a characteristic impedance of  $200\Omega$ .

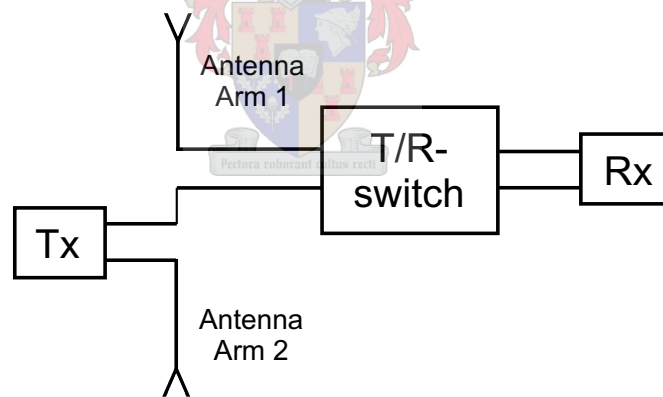


**Figure 1.1:** *Schematic representation of the monostatic radar system*

A short overview of each component is given below.

### Transmitter

The transmitter configuration is illustrated in Figure 1.2. A high voltage generator creates a potential of 400 V between the antenna terminals, one of which is held at ground potential. When the signal from the driver is high, the MOSFET in the circuit switches to the low impedance state, connecting the antenna feed to ground. The antenna terminals discharge rapidly through the feed-point, giving rise to a pulse that propagates along

the antenna and radiates into the surrounding medium. The measured MOSFET drain voltage (which is also the voltage across the antenna feed) at the time the transmitter fires ( $t=0$ ) is shown in Figure 1.3. The voltage has a fall time smaller than 10 ns and a Fourier analysis shows that the pulse has significant spectral components up to 100 MHz and higher.

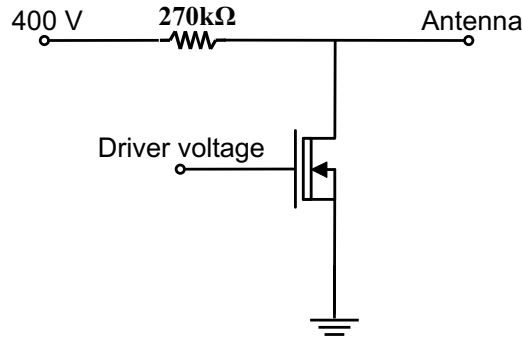


**Figure 1.2:** A simplified schematic of the monostatic BHR transmitter configuration

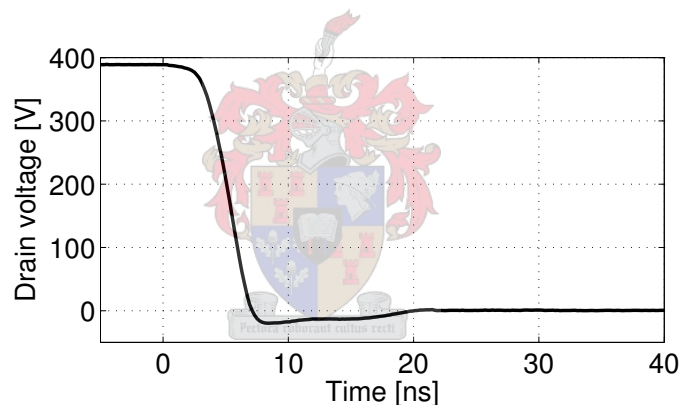


**Figure 1.3:** Measured voltage across the antenna feed-point as the transmitter fires

The MOSFET returns to the high impedance state after 3  $\mu\text{s}$  and the high-voltage generator slowly re-charges the MOSFET drain capacitance through a 270 k $\Omega$  resistor to 400 V. This charging of the antenna terminals hence occurs much slower (settling time of  $\sim 50$  ns) than the discharge and the voltage pulse does hence not have significant spectral content in the frequency band of interest (10 – 100 MHz).

After 100  $\mu\text{s}$  the antenna is again charged to 400 V and the transmitter fires again (the MOSFET goes to low impedance state). The PRF of the radar is hence  $1/(100 \mu\text{s}) = 10$  kHz.

### T/R switch

The T/R-switch isolates the receiver from the antenna feed-point for a period of  $\sim 100$  ns after the firing of the transmitter to prevent receiver saturation. It also implements a

shunt input 2<sup>nd</sup>-order Bessel-Thompson band pass filter when in through mode. Figure 1.4 shows the transfer function of the T/R-switch when it is in through-mode and terminated in a 200  $\Omega$  resistance, calculated from a circuit simulation.

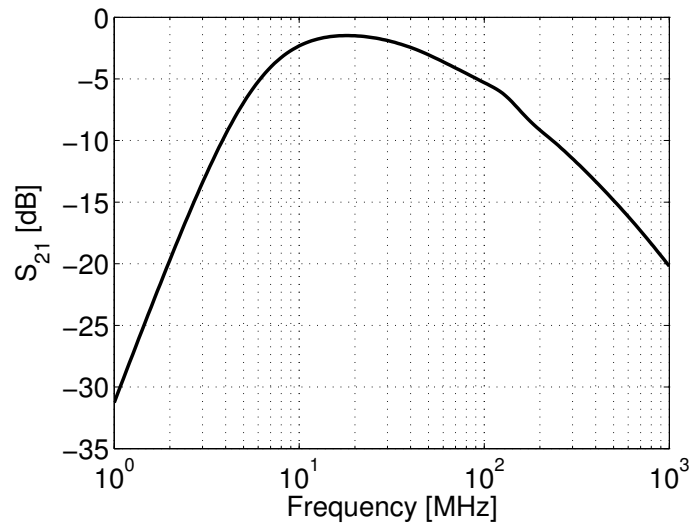


**Figure 1.4:** *Transfer function of the T/R-switch in through-mode*

The switch provides isolation that varies from 60 to 80 dB over the frequency band of interest when in isolation-mode.

The input impedance of the receiver in through-mode is shown in Figure 1.5. The input resistance of the switch in the 10 – 100 MHz band is acceptably close to the characteristic impedance of the circuit, 200  $\Omega$ . The input impedance when the circuit is in isolate-mode is negligible.

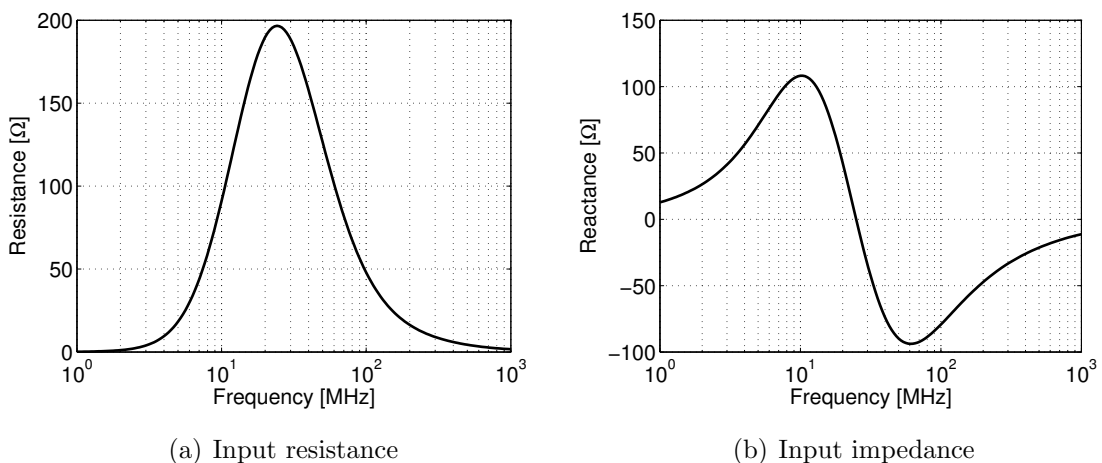


**Figure 1.5:** *Input impedance of the T/R-switch in through mode, terminated in a 200  $\Omega$  resistor*

## Receiver

The receiver gain stage is illustrated schematically in Figure 1.6. The receiver consists of a LNA providing 20 dB gain, STC amplifier providing a time dependent gain of 11 to 46 dB and an analog to digital converter (ADC) that digitizes the amplified signal. A resistive matching network between the STC amplifier and the ADC furthermore acts as a 6 dB attenuator.

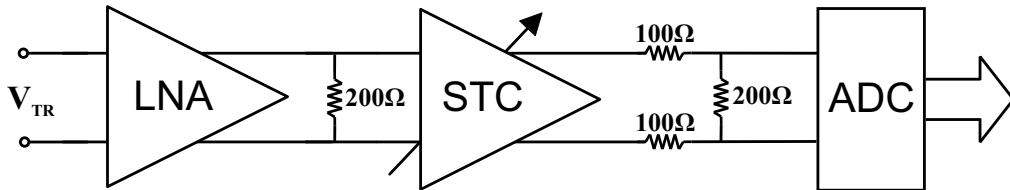


**Figure 1.6:** A schematic of the monostatic BHR receiver gain stage

The total gain from the output of the T/R-switch to the ADC input is shown in Figure 1.7.

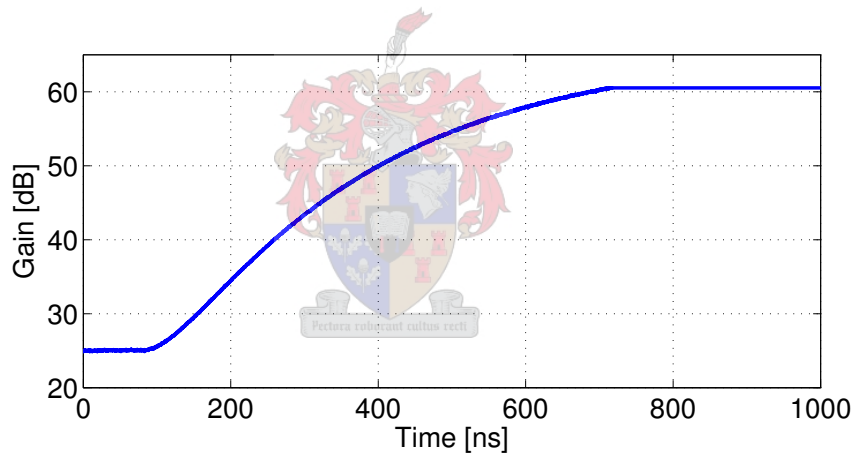


**Figure 1.7:** Time dependent total gain of the gain stage

A 8-bit ADC digitizes the amplified signal at a sampling period of 4 ns. 512 8-bit words are stored to give a total radar trace length of 2.048  $\mu$ s. The ADC implements a process called *stacking*, in which a preset number of traces are averaged to improve the signal to noise ratio. Only the eventual averaged trace is stored. In the case of the monostatic BHR system, stacking is performed over  $2^{14}$  traces, a process hence taking  $\sim 1.6$  s to complete. Data from the ADC is stored in flash memory, from where may be retrieved after a survey via wireless transmission using the Bluetooth protocol.

## Probe structure

The antenna is an asymmetric linear dipole with a resistively loaded arm and a conductive arm with total length of approximately 1.6 m. The conductive arm is a copper cylinder

of diameter 28 mm and length 910 mm that acts as the housing of the batteries and the transmitter and receiver electronics. The resistively loaded arm, length 600 mm is a copper strip conductor loaded with a 12-element discrete implementation of the Wu-King impedance loading profile [31], that creates a non-reflective current distribution along the antenna arm. The resistor values of the discrete Wu-King resistive profile and their positions along the antenna are indicated in table A.1.

The loaded arm is immersed in a potting material encased in a Perspex cylinder of inner diameter 20 mm and outer diameter 28 mm. The entire antenna is furthermore isolated from the external medium by a PVC casing, giving the probe an outer diameter of 32 mm. A more detailed account of the geometry of the monostatic BHR antenna is given in appendix A.

### Deployment and operation

Figure 1.8 shows the typical deployment configuration for the BHR antenna in a vertical borehole.

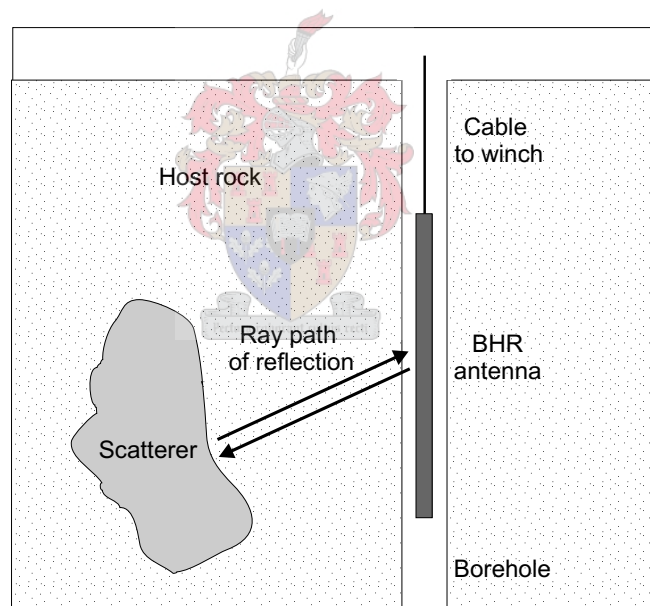


**Figure 1.8:** *A typical deployment configuration for the monostatic radar probe*

The BHR probe is attached with a non-metallic cable to a motorized winch at the surface and is lowered into the borehole.

Radar boreholes are typically drilled in host rocks which are reasonably translucent to radio waves in the HF and VHF bands [22]. An electromagnetic pulse radiated by the antenna hence travels through the host rock until it reaches a discontinuity. It is then scattered due to the contrast between the electric permittivity of the target and the host rock. The scattered signal propagates back to the antenna, where it is received, amplified and logged.

When taking measurements, the radar must move at a constant speed inside the borehole, to ensure that the stored radar traces can be mapped to regular spacial intervals along the borehole. The motorized winch raises or lowers the BHR probe in the borehole at the relatively slow speed of 10 m/minute, as required by the stacking process.

### 1.3 Limitations of the monostatic BHR

A complication inherent to monostatic radar systems is that the receiver must be isolated from the antenna when the transmitter fires and remain isolated until currents from the transmitter pulse have subsided. These steps must be taken to avoid saturation of amplifier stages in the receiver chain.

Signals reflected from radar targets will not be logged by the system if they arrive before the T/R switch has switched to through-mode and currents from the antenna discharge have not subsided sufficiently. A loss of radar data hence occurs for objects that are closer than a certain radius to the antenna. The T/R-switch of the BHR system investigated here places the antenna in receive-mode  $\sim 100$  ns after the transmitter has fired. For a typical propagation speed of EM-waves in hard rock,  $100.10^6$  m.s<sup>-1</sup>, data about the structure of the surrounding medium within a radius of 5 m from the antenna is lost.

The receiver of the experimental monostatic radar here studied may however still saturate if residual feed-point current from the transmitter pulse has not subsided sufficiently before the T/R-switch switches to through-mode. The closest range at which targets may be observed is hence determined by the time when the transmitter pulse currents are sufficiently dissipated to allow the receiver amplifier stages to leave saturation.

Radar traces from initial experiments using the monostatic BHR system in 75 mm air- and water-filled boreholes at De Beers Finsch diamond mines are shown in Figure 1.9. Traces from water-filled boreholes unexpectedly showed prolonged saturation leading to substantial close range and even total data loss.

The behaviour of the antenna in different borehole environments, notably in water-filled boreholes was not well understood and needed to be assessed. There was also a need for lumped networks with driving-point impedance similar to that of the radar antenna in certain borehole environments. This enables diagnostic measurements on the radar system to take place on the laboratory workbench, with the antenna load appearing as if it were the BHR antenna immersed in a certain borehole. Lastly, the time that the receiver remains saturated in a water-filled borehole must be reduced, in order to reduce the loss of radar data at close range. The latter was eventually achieved through simple modifications to the receiver circuit, as described in Chapter 5. The thesis also proposes an alternative solution to the slow settling time of feed-point current, namely the use of

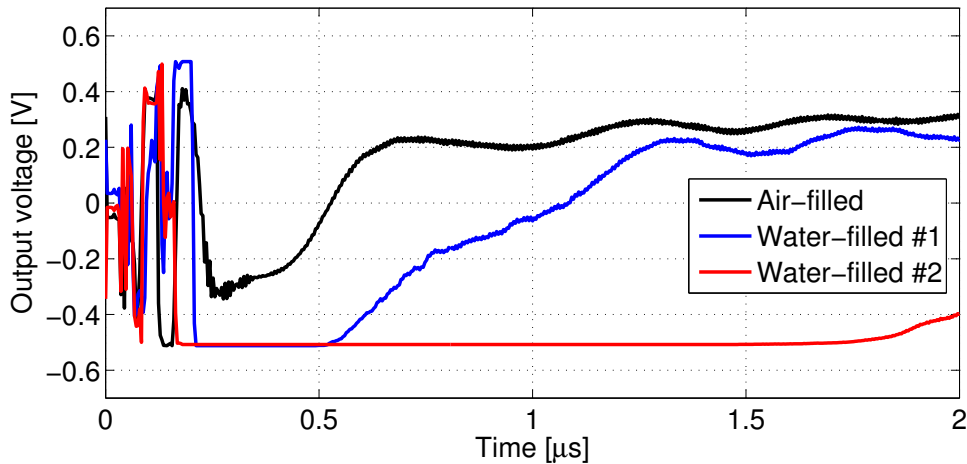


**Figure 1.9:** *Experimental radar traces from air-filled and water-filled boreholes with diameter 75 mm*

a resistive/capacitive profile to load the loaded arm of the BHR antenna.

## 1.4 Thesis outline

Measuring the feed-point and radiative characteristics of an insulated antenna deployed in a borehole is practically impossible at present. The project's initial focus is hence the accurate modelling of the BHR antenna in typical borehole environments. Theoretical and numerical models for the investigation of the monostatic BHR antenna are investigated in Chapter 2.

A model best suited for the investigation into the BHR antenna is selected and applied to model the antenna in air- and water-filled boreholes of differing diameter. The performance of the antenna in differing borehole environments and its interaction with the radar circuitry is investigated using this model in Chapter 3.

Chapter 4 investigates the synthesis of lumped element networks with driving-port impedance equivalent to the input impedance of the BHR antenna in different media, as simulated in Chapter 3, for use as dummy loads in laboratory diagnostics of the radar system.

The properties of Wu-King impedance loaded antennas in electrically dense media are investigated in Chapter 5. The use of an antenna with distributed resistance *and* capacitance as loading is proposed as a modification that would result in improved feed-point characteristics in water-filled boreholes. Results from simulation and experiment are presented that confirm that the new antenna design substantially reduces residual current levels after the transmitter fires.

# Chapter 2

## Electromagnetic modelling of the BHR antenna

### 2.1 Introduction

The BHR antenna is classified as an insulated antenna due to the presence of insulation layers around the central conductors of the antenna. An accurate theoretical description of insulated antennas in typical borehole environments is complicated and often no analytical solution to the field distribution exists. An investigation into the properties of the borehole radar antenna hence requires the application of numerical and simplified theoretical models.

Two commercial electromagnetic field simulation software packages, namely *CST Microwave Studio* and *FEKO*, utilized for the numerical modelling of the borehole radar antenna, are introduced in this chapter. A short description of the employed simulation method and the implementation of a borehole antenna model in each package is given. Numerical results of antenna input impedance and directivity from the two packages are shown to be in good agreement.

The chapter also describes a simplified model of insulated antennas in which the antenna is modelled as a simple transmission line and illustrates how it is applied to create an accurate model of the borehole radar antenna. Limitations of the transmission line model are discussed and input impedance and directivity computed from the model is compared with that from the simulation models.

The models will implement simplified forms of the borehole antenna geometry as specified in Appendix A. Measurements of hard rock samples by M. Rütchlin [22] showed that host rock environments encountered in borehole radar are generally of low loss with propagation speeds of  $\sim 100 \cdot 10^6$  m.s<sup>-1</sup>. The ambient medium in the all the models is hence taken as non conductive ( $\sigma = 0$ ) with  $\epsilon_r = 9$ .

## 2.2 Simulation models

### 2.2.1 CST Microwave Studio

#### Simulation method

CST Microwave Studio<sup>TM</sup> is an electromagnetic field simulation software package developed by Computer Simulation Technology (CST). The package implements four different simulation methods, namely a transient, frequency domain, eigenmode and modal analysis solver, all based on the Finite Integration Technique (FIT) [6]. Unlike the FDTD and FEM methods, FIT discretizes the integral form of Maxwell's equations rather than their differential form. Structures of arbitrary shape may be simulated. A finite calculation domain enclosing the modelled structure is defined and discretized. The method of spacial discretization is universal and applicable to electromagnetic problems in the time and frequency domain, for DC to high-frequency calculations.

CST Microwave Studio allows wide-band frequency domain data to be generated from a single time-domain simulation by applying the Discrete Fourier Transform to simulation time-signals. Time-domain signals such as antenna feed-point current and farfield waveforms as well as frequency domain radiation patterns and S-parameter data, may hence be calculated from a single simulation.

#### The borehole antenna model in CST Microwave Studio

CST Microwave Studio allows detailed modelling of the antenna as specified in Appendix A, however, some simplifications are introduced to the model, mainly to reduce simulation time. The detail of the antenna model as implemented in *CST Microwave Studio* is shown in Figure 2.1.

The potting and perspex layers surrounding the loaded arm and the PVC insulation surrounding the antenna, as illustrated in Figure 2.1(b), are modelled with dimensions and material properties as described in Appendix A.

The central conductor of the loaded antenna arm, physically implemented as a narrow copper strip, is modelled as a perfectly conducting wire. This simplification causes the borehole antenna model to possess circular symmetry around its longitudinal axis, which may be exploited to drastically reduce simulation time. It may be shown that the equivalent radius of a narrow conducting strip is one-fourth its width [3]. The width of the strips used to physically implement the loaded antenna arm is approximately 6 mm and an equivalent radius is hence chosen as 1.5 mm.

Lumped resistors creating the discrete Wu-King profile on the loaded arm have values and positions as given in Table A.1 in Appendix A.

The conducting arm is modelled as a perfectly electric conducting (PEC) solid cylin-

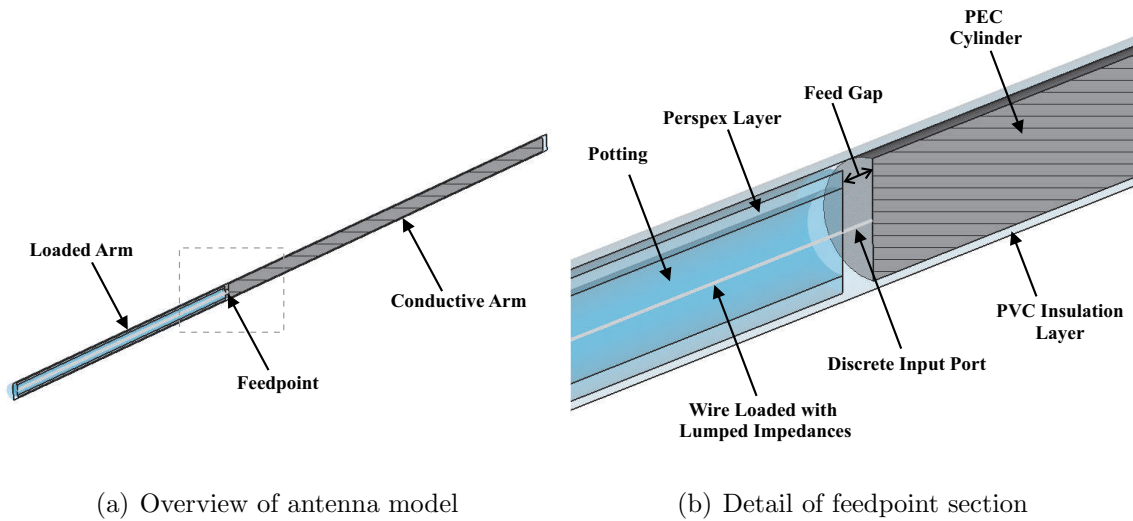


**Figure 2.1:** *Longitudinal cross-section of the borehole antenna model implemented in CST Microwave Studio*

der, which is a valid simplification since, at the frequencies of interest, the skin-depth of copper is several orders smaller than the thickness of the copper cylinder constituting the conductive arm. No meshing occurs inside PEC volumes and hence this simplification reduces simulation time. The TNC connectors connecting the two antenna arms are absorbed into the length of the conducting cylinder, since their outer surfaces are conductive and in ohmic contact with the copper cylinder. A feed gap length of 10 mm was chosen to correspond to the distance between the TNC connector and the start of the loaded conducting strip on the loaded arm.

CST Microwave Studio presents two different methods of feeding the antenna structure: the use of either the so-called discrete port or a waveguide port. The discrete port, shown in Figure 2.1(b), has two pins that connect the two antenna arms and realizes either a ideal voltage or current source, or a current source with an internal impedance that allows S-parameter calculation.

The discrete port was found to be inadequate for the calculation of S-parameters, since results do not converge with iterative denser meshing of the antenna model. It is still however adequate excitation for the determination of radiation patterns and time-domain far field waveforms. The discrete voltage port in particular will be utilized in the aforementioned calculation by simulating the voltage discharge waveform between the antenna arms that occurs when the transmitter fires.

To extract accurate antenna S-parameters, the feeding mechanism of the antenna must be modelled accurately. The antenna is hence fed through a  $50 \Omega$  coaxial waveguide embedded in the conductive antenna arm, as illustrated in Figure 2.2. The coaxial feed

is excited by a TEM wave generated by a waveguide port, shown in Figure 2.2(b).  $S_{11}$ -parameters are measured with respect to a reference plane set to the output side of the coaxial feed, as shown in Figure 2.2(b).

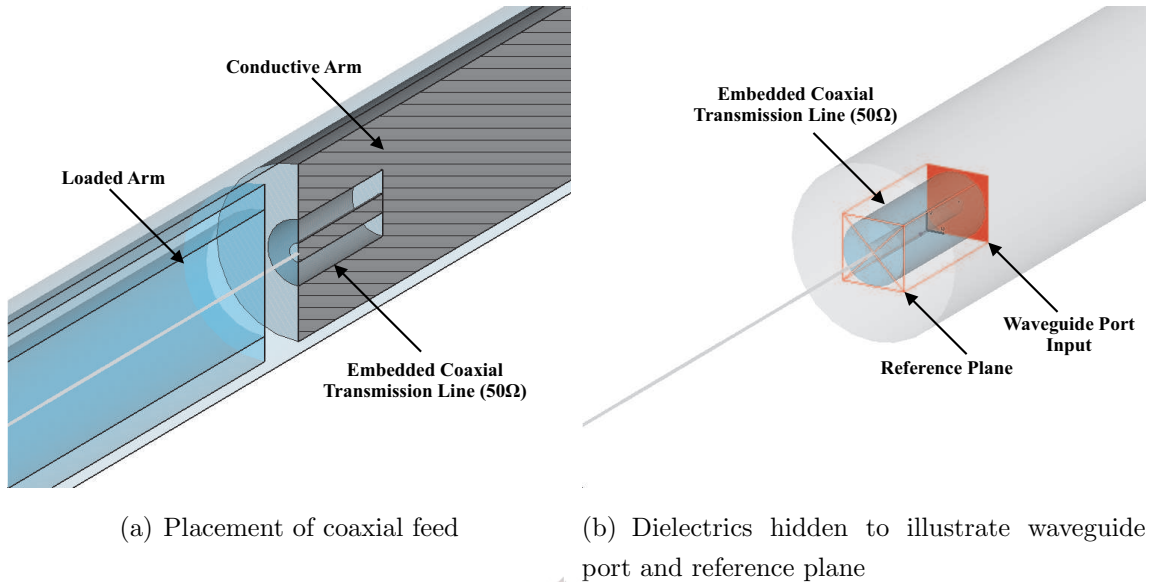


**Figure 2.2:** Details of CST Microwave Studio model feedpoint section using coaxial feed

## 2.2.2 FEKO

### Simulation method

FEKO is a Method of Moments (MoM) based electromagnetic simulation package developed by EM Software and Systems. FEKO can be used for the electromagnetic analysis of objects of arbitrary shape. The electromagnetic fields are obtained by first calculating the electric surface currents on conducting surfaces and equivalent electric and magnetic surface currents on the surfaces of dielectric solids. The electromagnetic fields and parameters such as input impedance and directivity are then calculated from these current distributions.

MoM is a frequency domain method and hence, unlike in CST Microwave Studio, numerous calculations have to be made to obtain wide-band data.

### A borehole antenna model in FEKO

Defining all the respective dielectric insulation layers in the FEKO model was found to lead to long calculation times when obtaining wide-band data, and it was decided to construct a further simplified model of the antenna insulation.

The geometry may be simplified by replacing the potting, perspex and PVC layers on the loaded arm with a single equivalent dielectric insulation layer, with outer radius

being that of the PVC layer. King *et al.* have shown [33, 17] that the 2-layer dielectric insulation, permittivities  $\epsilon_2$  and  $\epsilon_3$ , of the insulated conductor in Figure 2.3(a) is equivalent to a single insulation layer with permittivity  $\epsilon_{2e}$  shown in Figure 2.3(b), where

$$\epsilon_{2e} = \epsilon_2 \left[ \frac{\ln(c/a)}{\ln(b/a) + n_{23}^2 \ln(c/b)} \right] \quad (2.1)$$

with  $n_{23} = k_2/k_3$  and  $k_2 = \omega\sqrt{\mu\epsilon_2}$ ,  $k_3 = \omega\sqrt{\mu\epsilon_3}$ . Equation 2.1 holds only if the inequalities  $|k_2b| \ll 1$ ,  $|k_3c| \ll 1$  and  $a < b < c$  are satisfied and if the wavenumber of the external medium,  $k_4$ , is large compared to  $k_2$  and  $k_3$ . The above equation is derived Appendix B.

Using the above equation to absorb first the Perspex and then the PVC layer, a single insulation layer with equivalent relative permittivity of 3.4 results. This value is within 10% of the conductive arm insulation permittivity, namely 3.1. The model may hence be simplified further by defining a single insulation layer permittivity for both antenna arms, eliminating the need to mesh the junction between the loaded and conductive arm insulations. Subsequent simulation showed that such a simplification has a negligible effect on the results. The resulting antenna model for FEKO is shown in Figure 2.4, where a cutplane was inserted through the dielectric insulation layer for better visualization.

Furthermore, the simplified modelling of the antenna is largely similar to the CST Microwave Studio model as described in section 2.2.1. The loaded arm central conductor is again modelled as a cylindrical wire with radius 1.5 mm. The lumped elements creating the discrete Wu-King distribution on the loaded arm are implemented by loading short wire segments with resistance values and positions as specified in Table A.1 in Appendix A.

The conductive arm is again taken as a PEC cylinder, instead of copper, with the TNC connectors absorbed into the length of the cylinder. Only the surface of the PEC cylinder needs to be discretized when using MoM, as illustrated in Figure 2.4.

A 10 mm source segment separates the two antenna arms and feeds the antenna with a time-harmonic voltage.

### Erroneous computation of directivity and gain

In the simulations conducted in this chapter, FEKO was discovered to have difficulties in correctly calculating directivity and gain of antennas in certain environments. With directivity defined as *the ratio of radiation intensity in a certain direction to the average radiation intensity* [25] it is clear that the directivity must be larger than unity in some spherical direction. FEKO however routinely predicts a maximum directivity of less than unity for the insulated dipoles and borehole radar antenna studied in this chapter. The effect generally occurs at lower frequencies for antennas in ambient media with  $\epsilon_r > 1$ , with the conductivity of the ambient medium also affecting the result.

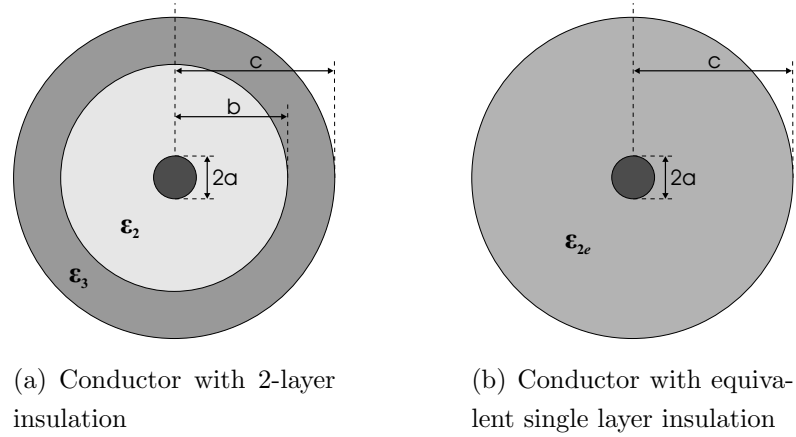


**Figure 2.3:** Geometry of the two-layer and single layer insulated conductors, mathematically equivalent by equation 2.1

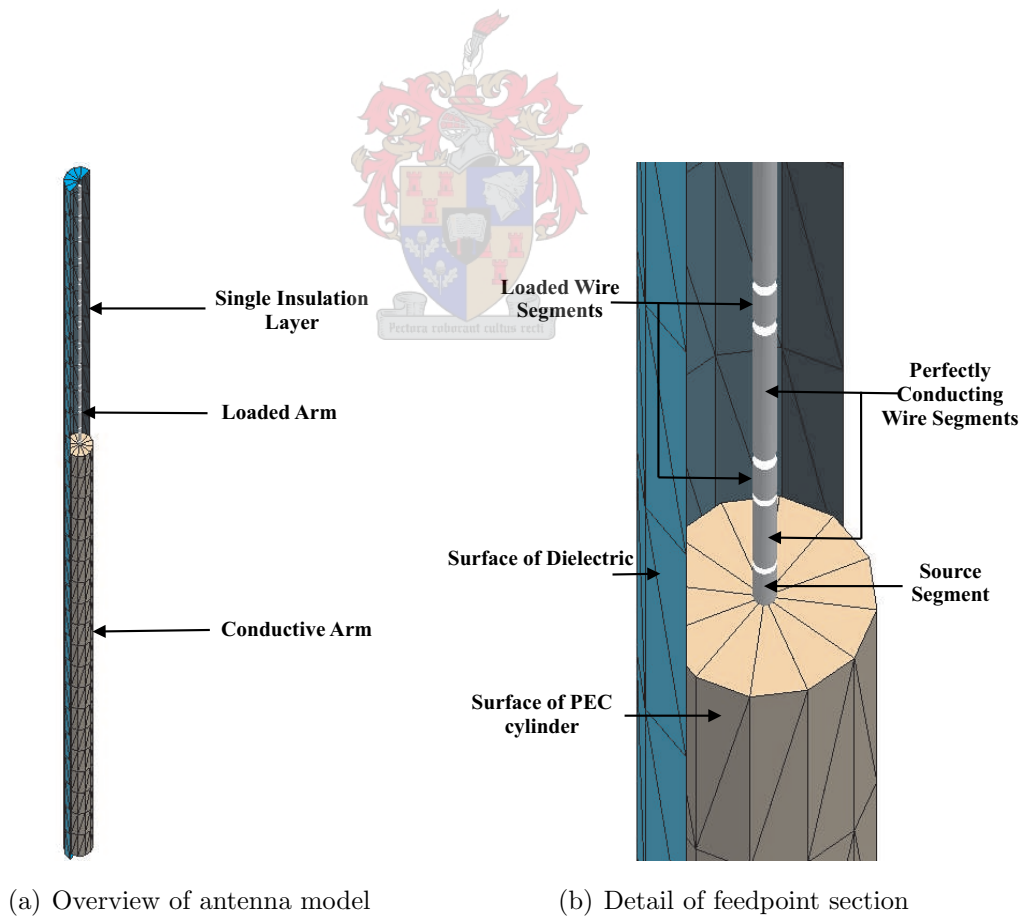


**Figure 2.4:** Details of the borehole antenna model implemented in FEKO

P. Le R. Herselman studied this problem in some detail [12] and developed an algorithm to calculate the directivity and gain off-line from FEKO near field calculations and the currents on wire segments in the simulation model.

It was initially suspected that the radiated electric field computed by FEKO is in error. The radiated field, calculated by FEKO in the form [8]

$$\vec{E}^r(\theta, \phi) = \lim_{R \rightarrow \infty} \frac{R}{e^{-jkR}} \vec{E}(\vec{r}, \theta, \phi) \quad (2.2)$$

was compared to the calculated electric near field for a insulated dipole at a sufficiently large radial distance,  $R \gg 2d^2/\lambda$ , where  $d$  is the maximum dimension of the dipole.<sup>1</sup> It was observed that the radiated field  $\vec{E}^r(\theta, \phi)$ , when scaled by  $\frac{e^{-jkR}}{R}$ , corresponds exactly to the computed near field values in shape and amplitude in lossy and non-conducting ambient media. This confirmed that the calculation of the radiated field is not in error and consequently that the directivity of the antenna may be computed directly from the radiated field  $\vec{E}^r(\theta, \phi)$ .

The directivity of an antenna with a  $\hat{z}$ -directed line source, hence with  $E_\phi^r = 0$ , may be expressed in terms of the radiated electric field as [25]:

$$D(\theta, \phi) = \frac{4\pi |E_\theta^r(\theta, \phi)|^2}{\int_0^{2\pi} \int_0^\pi |E_\theta^r(\theta, \phi)|^2 \sin(\theta) d\theta d\phi} \quad (2.3)$$

In instances where FEKO computed the directivity erroneously, it is hence computed from equation 2.3 in MATLAB using the `trapz` function to perform the integration.

### 2.2.3 Comparison of simulation packages

Simulation results from CST Microwave Studio and FEKO were found to be in good agreement, in spite of the substantially different simulation methods employed in each package. A comparison of the input impedance and directivity calculated from the two simulation packages is shown in Figure 2.5 for the specific case of the borehole radar antenna in a loss free ambient medium with relative permittivity  $\epsilon_r = 9$ . In these simulations the antenna was orientated with the conductive arm along the positive  $z$ -axis (direction  $\theta = 0$ ).

As discussed in section 2.2.2, FEKO has difficulty in calculating directivity in electrically dense media at low frequencies. This was again evident in the initial calculation of directivity at 10 MHz for this illustration, where a maximum directivity of less than unity resulted. The directivity for FEKO at 10 MHz shown in Figure 2.5(c) was hence calculated directly from the simulated radiated electric field from equation 2.3 as described in section 2.2.2.

---

<sup>1</sup>The dimensions of  $\vec{E}^r(\theta, \phi)$  in equation 2.2 is in fact volts and not volts/meter, however it may be viewed as identical to the radiated electric field calculated at a distance of  $R = 1$  m.

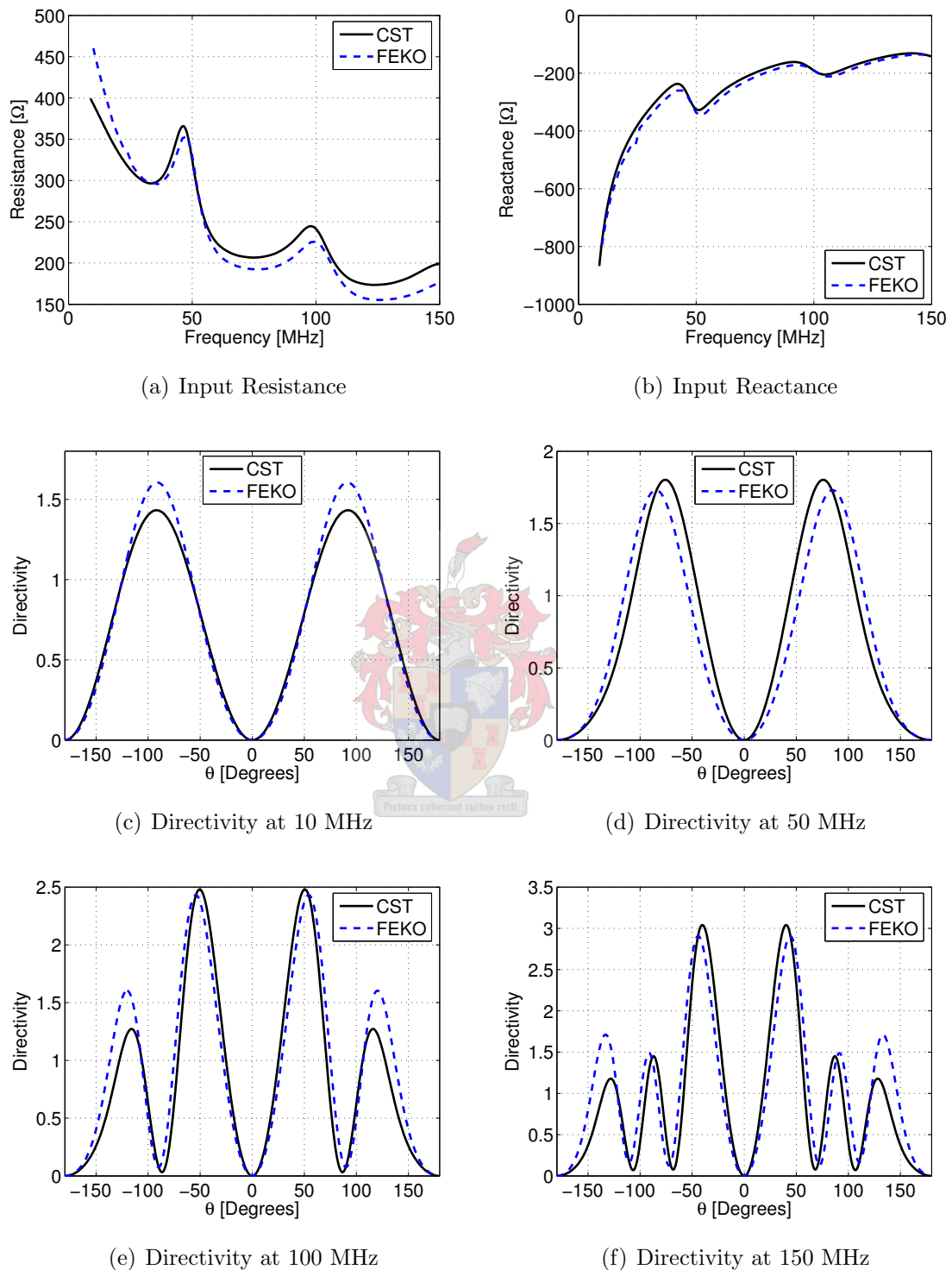


**Figure 2.5:** Comparison of input impedance and directivity of the BHR antenna obtained with CST Microwave Studio and FEKO

The good correspondence between the CST Microwave Studio and FEKO simulation results creates confidence in the validity of the predictions in the absence of experimental measurements of the antenna properties when it is deployed in a borehole.

## 2.3 The transmission line model of insulated antennas

The host media in which the borehole radar antenna are deployed generally have electric permittivities higher than that of the antenna insulation and may be conductive. The properties of such insulated antennas, namely where the wavenumber of the ambient medium is large compared to that of the insulation, was initially investigated by Wu, King and Giri [33]. The antenna was found to behave as a transmission line with a lossy outer conductor, with radiation losses included in the series impedance per unit length of the transmission line. This is a useful and surprising result, since radiation is generally dependent on the electrical size of the antenna as a whole, and not simply a property that may be apportioned per unit length of the antenna. Wu, King and Giri subsequently proposed a transmission line model of the insulated antenna in electrically dense media, to be termed the *WKG model* for brevity.

A transmission line model having increased accuracy over the WKG model in environments where the wavenumber of the external medium is not much larger than that of the insulation, was proposed by Smith and King [16] as well as Chen and Warne [4]. This model was used extensively by D.M. Claassen [5] in the modelling of resistively loaded antennas in air-filled boreholes and to a lesser extent by M.D. van Wyk [29]. It was however discovered in this investigation that the latter model gives unphysical input impedance results in certain conditions, an effect that is not well understood and not discussed in literature. This is to be discussed further in section 2.3.4.

The insulated antenna models are introduced in the following section in terms of a generalization of conventional coaxial transmission line theory. The transmission line parameters of the models are derived in Appendix B.

### 2.3.1 Formulation of transmission line parameters

The geometry of the coaxial transmission line model is shown in Figure 2.6. Region 1 in Figure 2.6 is a solid metal conductor, while regions 2 and 3 are dielectric insulation layers. The inclusion of a second insulation layer, layer 3, is a practical consideration, since the inner insulation layer may be a fluid requiring containment in a plastic tube. Region 4, the surrounding medium, is assumed to be infinite, homogeneous and isotropic.

A permittivity  $\epsilon_i$ , permeability  $\mu_i$  and conductivity  $\sigma_i$  is associated with each medium.

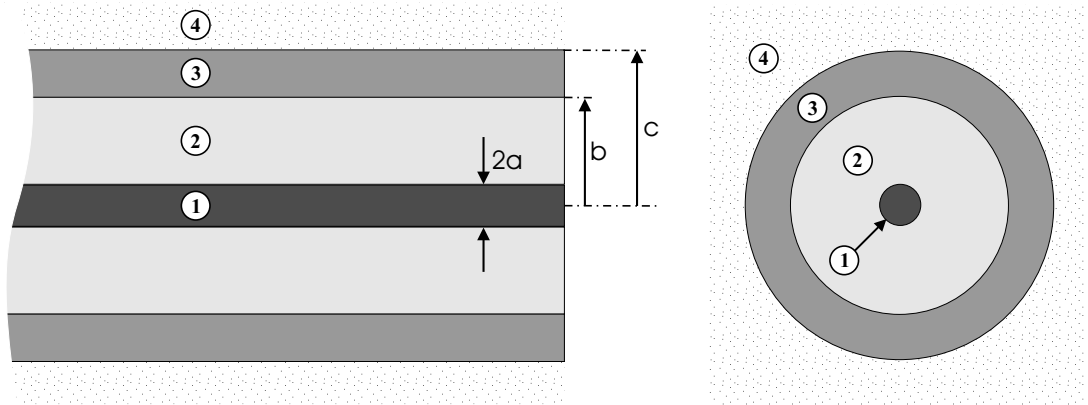


**Figure 2.6:** Longitudinal and axial cross-sections of the assumed geometry of the coaxial transmission line model of the insulated antenna

All materials are assumed to be nonmagnetic with permeabilities given by  $\mu_i = \mu_0$ , where  $\mu_0 = 4\pi \times 10^{-7}$  henry/m is the permeability of free space. The complex wavenumber for each medium is given by

$$k_i = \omega \sqrt{\tilde{\epsilon}_i \mu_0}, \quad i = 1, 2, 3, 4 \quad (2.4)$$

where  $e^{j\omega t}$  time-dependence is assumed and  $\tilde{\epsilon}_i = \epsilon_i + \sigma_i/j\omega$  is the complex permittivity of the medium.

The analysis that follows assumes only a single insulation layer, since the analogy with traditional coaxial transmission lines is more apparent and the arithmetic is simpler. The effect of the second insulation layer may be incorporated into the first at a later stage, using equation 2.1, which is derived in Appendix B.

Assuming that region 1 and 4 are good conductors, that regions 2 is a good insulator ( $\sigma_2 \approx 0$ ) and that region 3 is absent ( $b = c$ ), the model in Figure 2.6 is similar to a coaxial transmission line. The transmission line condition for electrically small cross-sections must hold, which make higher propagation modes negligible and keep end-effects small [16].

$$k_2 b \ll 1, \quad h \gg b > a \quad (2.5)$$

where  $h$  is the length of the transmission line section. The current on the inner conductor then satisfies the differential equation

$$(d^2/dz^2 + k_L^2)I(z) = 0 \quad (2.6)$$

where the complex wave number<sup>2</sup>  $k_L = \beta_L - j\alpha_L$  is defined as

$$k_L = \sqrt{-z_L y_L} \quad (2.7)$$

<sup>2</sup>Related to the propagation constant  $\gamma_L$  by  $k_L^2 = -\gamma_L^2$ , with the correct root given by  $k_L = -j\gamma_L$

A corresponding characteristic impedance may also be defined:

$$Z_c = \sqrt{\frac{z_L}{y_L}} \quad (2.8)$$

where  $z_L$  is the series impedance per unit length of the transmission line and  $y_L$  is the shunt admittance.

### The WKG model

Wu, King and Giri [33] proposed a series impedance for the transmission line model consisting of three parts:

$$z_L = z_1 + z_2 + z_4 \quad (2.9)$$

where  $z_1$  and  $z_4$  are the internal, or surface impedances of the inner and outer conductors respectively, while  $z_2$  is the impedance per unit length of the insulation layer, or layers. These impedances are defined by the expressions [16]:

$$z_1 = \frac{1}{\pi a^2 \sigma_1} \frac{k_1 a J_0(k_1 a)}{2 J_1(k_1 a)} \quad (2.10)$$

$$z_2 = \frac{j\omega\mu}{2\pi} \ln(b/a) \quad (2.11)$$

$$z_4 = \frac{j\omega\mu}{2\pi} \frac{H_0^{(2)}(k_4 b)}{k_4 b H_1^{(2)}(k_4 b)} \quad (2.12)$$

$J_n$  is the Bessel function of the first kind of order  $n$ .  $H_n^{(2)}$  is the Hankel function of the second kind of order  $n$ . The expressions for  $z_2$  and  $z_4$  are derived in Appendix B. It was found that  $z_1$  generally has a negligible contribution to the series impedance if region 1 is a good conductor. The analysis in Appendix B consequently assumes a PEC central conductor, hence  $z_1 = 0$ , to simplify the analysis.

In the single insulation layer environment, the shunt admittance per unit length of the WKG model is simply given by

$$y_L = y_2 = \frac{j2\pi k_2^2}{\omega\mu \ln(b/a)} \quad (2.13)$$

as derived in Appendix B and given in [16]. When a second insulation layer, layer 3, is present  $y_L$  is given by the series combination of  $y_2$  and  $y_3$ , which leads to

$$y_L = y_2 \left[ \frac{\ln(b/a)}{\ln(b/a) + n_{23}^2 \ln(c/b)} \right] \quad (2.14)$$

as is also shown in Appendix B. Equivalently, the second layer may be *absorbed* into the first by defining a single equivalent insulation layer with a equivalent relative permittivity  $\epsilon_{2e}$  given by equation 2.1 and with outer radius  $c$ .

Wu, King and Giri [33] showed that the transmission line model as defined above is not only applicable when the ambient medium is a good conductor, but even if it is a perfect dielectric. The transmission line properties of the insulated antenna hold both when the ambient medium is a dielectric and energy is lost via radiation and when the ambient medium is conductive and energy is lost through the diffusion of conductive currents.

The model is however only an accurate approximation when  $|k_4^2| \gg |k_2^2|$ . In practice, King and Smith [16], found it to be accurate for  $|k_4^2| > 16|k_2^2|$ , which places great restriction on its usefulness. For the borehole antenna, with insulation permittivity  $\epsilon_{r2} \approx 3$ , inside a borehole environment where the ambient medium, rock, is generally non-conductive with permittivity  $\epsilon_{r4} \approx 9$ , we have  $|k_4^2|/|k_2^2| \approx 3$ . The model would hence be accurate for the borehole antenna immersed in water, but not for the antenna inside a typical borehole environment.

Furthermore, when  $a \rightarrow b$  the insulating layer is eliminated and the conductor is embedded in the ambient medium and we hence expect the wavenumber to approach that of the external medium,  $k_L \rightarrow k_4$ , however the model gives  $k_L \rightarrow \infty$  in this limit.

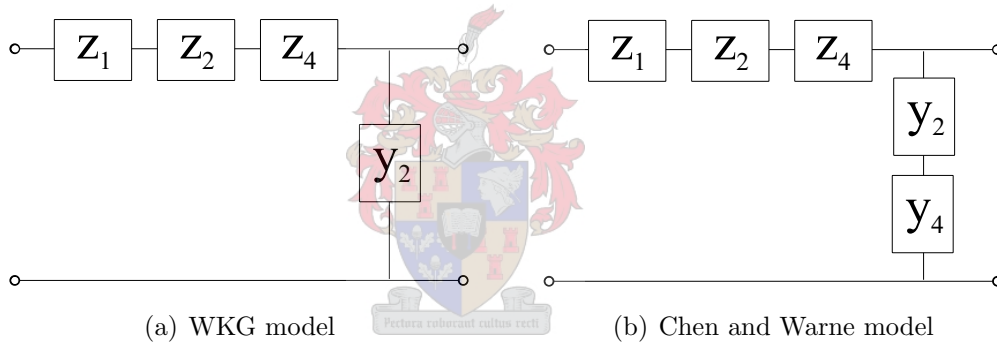


**Figure 2.7:** *Equivalent circuits for the transmission line model of insulated antennas*

### Chen and Warne's model

To remedy the above problems, Chen and Warne [4] introduced an ambient medium admittance  $y_4$  into the model, such that  $k_L \rightarrow k_4$  in the limit  $a \rightarrow b$ . This uniquely defines  $y_4$  as

$$y_4 = \frac{2\pi j k_4^2 k_4 c H_1^2(k_4 c)}{\omega \mu H_0^2(k_4 c)} \quad (2.15)$$

which is added in series to the admittance of region 2 so that the new equivalent shunt admittance per unit length of the transmission line becomes:

$$y_L = \frac{y_2 y_4}{y_2 + y_4} \quad (2.16)$$

The expression for  $y_4$  also satisfies the relation  $k_4 = \sqrt{-z_4 y_4}$  and is derived by different means in Appendix B.

King and Smith [16] also proposed a more general expression for  $k_L$  and  $Z_c$  [16] for the model for which  $k_L \rightarrow k_4$  in the limit  $a \rightarrow b$  and showed the expression for the wavenumber to be accurate down to  $|k_4^2| > 2|k_2^2|$ .

$$k_L = k_2 \left[ \frac{k_4^2 [H_0^2(k_4 b) + k_4 b \ln(b/a) H_1^2(k_4 b)]}{k_2^2 H_0^2(k_4 b) + k_4^2 (k_4 b) \ln(b/a) H_1^2(k_4 b)} \right]^{\frac{1}{2}} \quad (2.17)$$

$$Z_c = \frac{\zeta_2 k_L}{2\pi k_2} \left[ \ln(b/a) + \frac{k_2^2 H_0^2(k_4 b)}{k_4^2 k_4 b H_1^2(k_4 b)} \right] \quad (2.18)$$

where  $\zeta_2 = \sqrt{\frac{\mu}{\epsilon_2}}$ . It may be shown that the resulting wavenumber and characteristic impedance using Chen and Warne's approach is exactly equivalent to that proposed by Smith and King above when the central conductor is PEC. The wavenumber of Chen and Warne's model is hence also assumed to be accurate when  $|k_4^2| > 2|k_2^2|$ .

This more general model was unfortunately found to give unphysical input impedance results, namely negative input resistance, when the ambient medium is of low conductivity. Due to this serious flaw, which is not discussed in literature, the model cannot be used reliably even though it gives very accurate results in other circumstances. This is to be investigated in detail in section 2.3.4.

### Modelling of multiple insulation layers and boreholes

The discussion thus far focused on modelling of insulated antennas with one or two insulation layers in homogeneous ambient media. The borehole antenna loaded arm however has 3 distinct insulation layers, while the external medium is cylindrically stratified when the antenna is deployed in a borehole. The model needs to be able to take such geometries into account if it is to be of practical use.

As described in section 2.3.1, two layers of outer radius  $b$  and  $c$  may be absorbed into an equivalent layer with outer radius  $c$ , using equation 2.1. The above process may be applied iteratively to absorb a large number of layers into a single equivalent layer if the wavenumbers of the respective insulation media are much smaller than that of the external medium and the diameter of the eventual equivalent layer remains electrically small. The two innermost insulation layers are absorbed first, after which the adjacent, third layer is absorbed into the newly defined equivalent layer, and so forth.

Air-filled boreholes may conveniently be viewed as an extra insulation layer and be absorbed into an equivalent layer as such, since it has a wavenumber much smaller than that of typical host rock environment.

Water-filled boreholes may however not be treated as an insulation layer in this respect, since the wavenumber in water is much larger than that of the typical host rock

environment. Attempts to extend the transmission line model to make modelling of water-filled boreholes possible were made in attempting to find analytical approximations to the field solution of an infinite linear wire centered in a 3-layer cylindrically stratified medium under certain reasonable assumptions, in analogy with the 2-layer derivations in Appendix B. These attempts were as yet unsuccessful, with the consequence that the transmission line model in its present form may only model the BHR antenna in homogeneous rock and air-filled boreholes.

The inability to model antennas in water-filled boreholes is a major drawback of the transmission line model, since the modelling the behaviour of the borehole antenna in latter environment will be a priority in the following chapters.

### 2.3.2 Current distribution, input impedance and far field

The transmission line parameters for the insulated antenna model may be applied to specific insulated antenna geometries to compute the antenna current distribution, input impedance and far field patterns.

Much of the literature on the transmission line model of insulated antennas concentrates on the input impedance of insulated dipole antennas. The current distribution for the dipole will hence be derived to provide a base for comparison with literature and previous work using the transmission line model.

The main interest is however the creation of an accurate model of the BHR antenna. The antenna will have to be modelled as a non-uniform transmission line, since the cross-sectional geometries of the two antenna arms differ and will hence have different transmission line parameters. The specific discrete resistive loading profile implemented on the loaded arm will also have to be modelled. The current distribution is hence computed by treating the antenna as several transmission line sections connected in series.

#### Insulated dipoles

The insulated dipole considered will have a halflength  $h$  and be driven at the center by a voltage source  $V_O$ . This corresponds to the series connection of two identical open circuited coaxial transmission lines, as illustrated in Figure 2.8, driven at the center,  $z = 0$ , by a delta-gap voltage source  $V_O$ .

In Appendix C it is shown that the current distribution that solves the differential equation 2.6 for the insulated dipole is

$$I(z) = \frac{jV_O \sin[k_L(h - |z|)]}{2Z_c \cos(k_L h)} \quad (2.19)$$

and it follows that the input impedance is

$$Z_{in} = -2jZ_c \cot(k_L h) \quad (2.20)$$

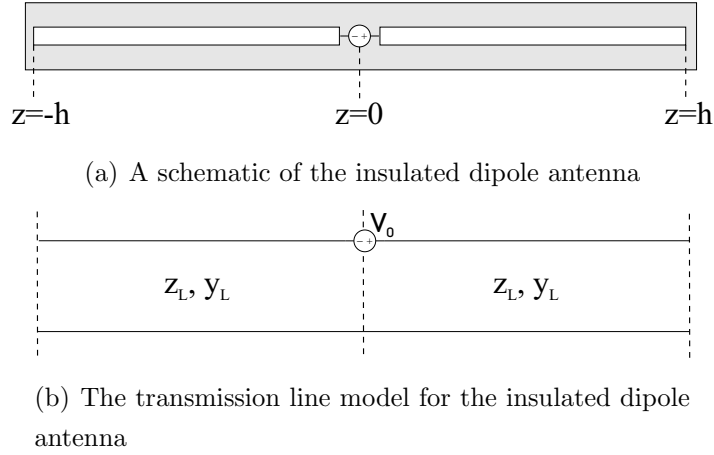


**Figure 2.8:** *The insulated dipole antenna and its equivalent transmission line model*

King and Smith [16] calculated the radiated electric field of the insulated dipole as

$$E_{\theta}^r(\mathbf{r}) = \frac{j\omega\mu I(0)}{2\pi k_4 r} e^{-jk_4 r} \left[ J_0(k_4 b \sin \theta) - k_4 b \ln(b/a) [(k_L/k_2)^2 - 1] \right. \\ \left. \times J_1(k_4 b \sin \theta) / \sin \theta \right] F_0(\theta, k_4 h, k_L h) \quad (2.21)$$

where

$$F_0(\theta, k_4 h, k_L h) = \frac{[\cos(k_4 h \cos \theta) - \cos(k_L h)] \sin \theta}{[(k_L/k_4) - (k_4/k_L) \cos^2 \theta] \sin(k_L h)} \quad (2.22)$$

The same result may be obtained by applying the equation for calculating the radiated field of the multiple section antenna presented in the next section.

### General insulated linear antennas

The borehole antenna will be modelled as a number of transmission line sections connected in series, or a discontinuous transmission line as illustrated in Figure 2.9. A method to compute the current on such a multiple section transmission line is presented in Appendix D. The method is almost identical to that presented by Claassen [5], with minor differences that will be outlined below.

The antenna is modelled as  $N$  series connected transmission line sections, with allowance that sections may be connected through a voltage source and/or series impedance. The current and voltage distribution on each section is given by:

$$I_m(z) = A_m \cos[k_{Lm}(h_m - z)] + B_m \sin[k_{Lm}(h_m - z)] \quad (2.23)$$

$$V_m(z) = jA_m Z_{cm} \sin[k_{Lm}(h_m - z)] - jB_m Z_{cm} \cos[k_{Lm}(h_m - z)] \quad (2.24)$$

with  $m = 1 \dots N$  and  $h_{m-1} < z < h_m$ .  $A_m$  and  $B_m$  are unknown coefficients to be determined by the application of boundary and continuity equations. In Appendix D,

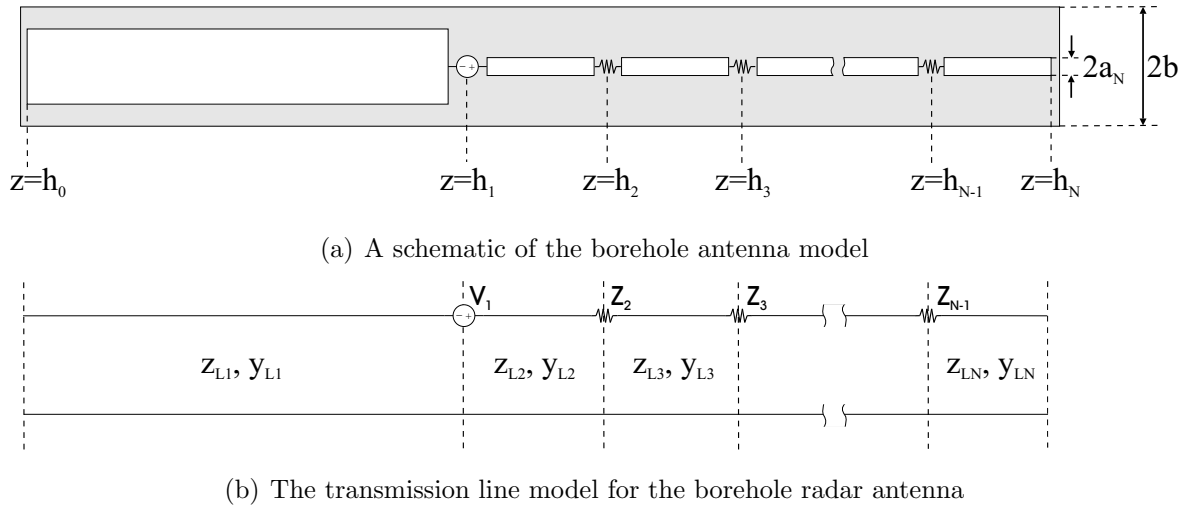


**Figure 2.9:** *The borehole radar antenna and its equivalent transmission line model*

these are written as simultaneous equations in matrix form  $\mathbf{M}\mathbf{U} = \mathbf{S}$ , where  $\mathbf{S}$  is a source vector,  $\mathbf{M}$  a square boundary condition matrix, and  $\mathbf{U}$  the vector of unknown coefficients. The unknown coefficients are found by computing  $\mathbf{U} = \mathbf{M}^{-1}\mathbf{S}$ .

The input impedance seen by a voltage source  $V_m^e$  at  $z = h_m$  is simply

$$Z_{in} = \frac{V_m^e}{I_m(h_m)} = \frac{V_m^e}{A_m} \quad (2.25)$$

The method used in Appendix D differs from that of Claassen mainly in the definition of the voltage continuity condition between adjacent sections. It is assumed that a series impedance may be present between adjacent sections, so that the exact discrete Wu-King loading profile implemented on the borehole radar antenna may be implemented. Claassen implemented loading profiles by lowering the conductivity of the central conductor of the loaded arm in a stepwise fashion. The approach used in Appendix D is somewhat simpler and allows general impedance (resistive *and* reactive) profiles to be implemented.

This general method is applied to the borehole antenna model shown in Figure 2.9, using  $N = 14$  sections. The leftmost section is the conductive arm, connected to the rest of the structure through a voltage source. The loaded arm is modelled as 13 sections connected through 12 resistors that constitute the discrete Wu-King profile as specified in Appendix A. The lengths of the sections correspond exactly to the geometry of the antenna as specified.

The radiated field of the multiple section transmission line model is derived in Appendix E from radiated field equations for a insulated dipole derived by Smith [16]. The method of derivation followed was identical to that used by Claassen [5].

The expression for the radiated electric field for the  $z$ -directed antenna in spherical coordinates is found to be

$$E_{\Theta}^r = \frac{j\omega\mu_0}{4\pi r} e^{-jk_4(r+h_S \cos \Theta)} \sum_{m=1}^N \left[ \sin \Theta J_0(k_4 b \sin \Theta) - k_4 b \ln \left( \frac{b}{a_m} \right) \left( \frac{k_{Lm}^2}{k_{2m}^2} - 1 \right) \right. \\ \left. \times J_1(k_4 b \sin \Theta) \right] \int_{h_{m-1}}^{h_m} e^{jk_4 z' \cos \Theta} I_m(z') dz' \quad (2.26)$$

with

$$\int_{h_{m-1}}^{h_m} e^{jk_4 z' \cos \Theta} I(z') dz' = \frac{e^{jk_4 h_{m-1} \cos \Theta}}{k_{Lm}^2 - k_4^2 \cos^2 \Theta} \left[ e^{jk_4 \Delta h_m \cos \Theta} \left( A_m j k_4 \cos \Theta + B_m k_{Lm} \right) \right. \\ \left. - j k_4 \cos \Theta \left( A_m \cos[k_{Lm} \Delta h_m] + B_m \sin[k_{Lm} \Delta h_m] \right) \right. \\ \left. + k_{Lm} \left( A_m \sin[k_{Lm} \Delta h_m] - B_m \cos[k_{Lm} \Delta h_m] \right) \right] \quad (2.27)$$

where  $h_S$  is the distance of the source to  $z = 0$  and  $\Delta h_m = h_m - h_{m-1}$ .

This completes the theoretical derivations for current distribution, input impedance and radiated field for the model of insulated antennas. The performance of the theoretical models are to be compared to that of the simulation models in the following sections.

### 2.3.3 Evaluation of WKG model

As noted in section 2.3.1, the WKG transmission line model is only a good approximation when the wavenumber of the ambient medium is much larger than that of the insulation of the antenna to be modelled, or in quantitative terms, when  $|k_4^2| > 16|k_2^2|$ . The model cannot be applied to model the borehole antenna when deployed in a typical host rock environment and it consequently not be studied in much detail.

The only physically significant instance in which the WKG model may model the borehole antenna accurately, is when it is immersed in an ambient medium of homogeneous water. A comparison of the modelled input impedance of the borehole antenna in water ( $\epsilon_r = 81$ ,  $\sigma = 4S$ ) to that in FEKO is shown in Figure 2.10.

There is clearly good correspondence between the MoM model of the antenna and the transmission line model in this instance. To model the antenna in rock, we must however turn to the model proposed by Chen and Warne, which is less restrictive.

### 2.3.4 Evaluation of Chen and Warne's model

King and Smith showed that the wavenumber for this model is accurate down to  $|k_4^2| > 2|k_2^2|$  [16] and it may hence be applied in the modelling of the borehole radar antenna in the host rock environments in which it is generally employed, where  $|k_4^2|/|k_2^2| \approx 3$ .

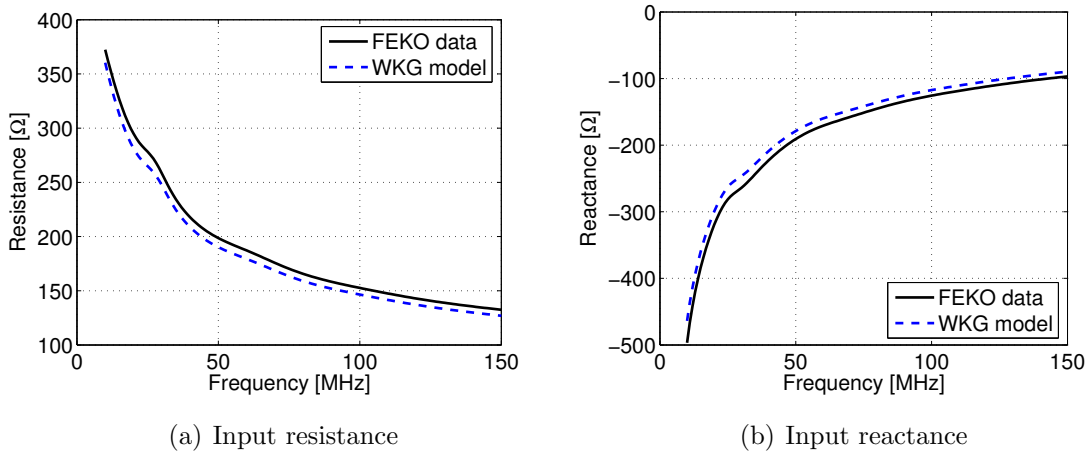


**Figure 2.10:** Comparison of input impedance from the WKG model and FEKO of the BHR antenna in water

The input impedance predicted by the model was unfortunately found to be erroneous in environments of low ambient medium conductivity – unphysical input impedance results (negative input resistance) are produced at low frequencies as well as near resonant frequencies when the ratio of insulation to conductor radius  $\frac{b}{a}$  is small. This failure occurs regardless of the transmission line conditions of equation 2.5 or the condition  $|k_4^2| \gg |k_2^2|$  being met and is not discussed in literature.

Appendix F illustrates analytically that Chen and Warne’s model may give negative input resistance results for the case of an insulated dipole in a non-conductive ambient medium at low frequencies, confirming that the observed effect is not due to numerical inaccuracies or computational errors.

In spite of the model’s failure in this respect, input impedance results from Chen and Warne’s transmission line model presented in Claassen’s PhD dissertation [5] and M.D. van Wyk’s MSc thesis [29] were reproduced successfully. Results from King and Smith’s [16, Chapter 8] modelling of the insulated dipole in water using the equivalent model of equations 2.17 and 2.18 could also be reproduced successfully. In the above cases the antennas were modelled in regions where  $|k_4^2| \gg |k_2^2|$  and at higher frequencies, where the model generally does not produce erroneous input impedance results. No other instances of the modelling of insulated antennas using Chen and Warne’s model could be found in literature.

The failure of the model prompted the derivation of the transmission line parameters, presented in Appendix B, in an exact and an approximate form (under the assumption  $|k_4^2| \gg |k_2^2|$ ), the latter yielding and hence confirming the transmission line parameters as given by Chen and Warne [4]. The input impedance of insulated dipoles calculated using the exact form of the transmission line parameters (requiring the calculation of  $k_L$  from

a transcendental equation) correspond closely to that calculated from the approximate parameters for  $|k_4^2| > 2|k_2^2|$ ; also displaying unphysical input impedance results. No apparent error could hence be found in the expressions for the transmission line parameters and the failure of the model is subject to further investigation.

The model does however produce correct input impedance results when the conductivity of the ambient medium is of order 1 mS/m and higher. In the subsequent studies of the transmission line model of insulated antennas in lossless ambient media, a small conductivity was hence artificially added to the modelled ambient medium to avoid the occurrence of non-physical input impedance results.

Although the expression for the wavenumber  $k_L$  is accurate down to  $|k_4^2| > 2|k_2^2|$ , the assumption that a transmission line current distribution exists on the antenna is still only valid when  $|k_4^2| \gg |k_2^2|$  [16]. The accuracy of the modelled input impedance in environments where the value of the ratio  $|k_4^2|/|k_2^2|$  is low is hence uncertain. Before attempting to model the borehole radar antenna, the accuracy of the modelled input impedance in these environments will be ascertained through comparison with results from FEKO MoM simulations for simple insulated dipoles.

Figure 2.11 compares the modelled input impedance and that from FEKO simulations for a insulated dipole with  $a = 1$  mm,  $b = 8$  mm and half-length  $h = 1$  m in a non-conductive ambient medium (although the modelled ambient medium was given a conductivity of 1 mS/m to avoid the appearance of unphysical input impedance results). Insulation permittivity of the dipole is  $\epsilon_{r2} = 1$ , with the ambient medium permittivity varying as  $\epsilon_{r4} = 32, 16$  and 8, respectively resulting in values of  $|k_4^2|/|k_2^2| = 32, 16$  and 8.

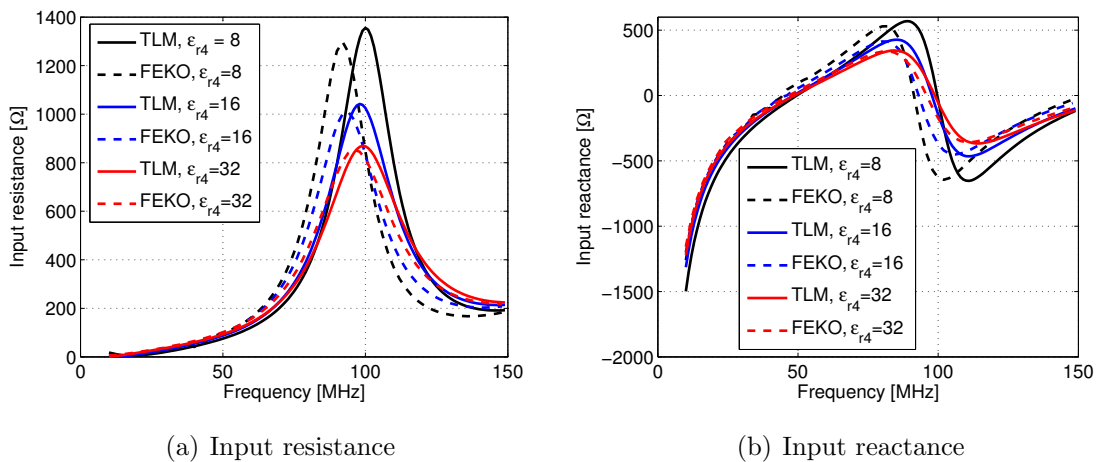


**Figure 2.11:** Comparison of input impedance from Chen and Warne’s model with that of FEKO for an insulated dipole antenna in different ambient media

There is good correspondence between FEKO and the transmission line model for higher values of  $|k_4^2|/|k_2^2|$ , however the values of the dipole’s resonant frequency pre-

dicted by the numerical and theoretical models start to diverge considerably (by 10%) at  $|k_4^2|/|k_2^2| = 8$ .

The accuracy of the modelled input impedance was also seen to diminish as the ratio of outer to inner conductor radius,  $\frac{b}{a}$ , decreases. This is illustrated in Figure 2.12 for an insulated dipole with half-length  $h = 1$  m,  $b = 8$  mm and a variable inner conductor radius with values  $a = 2, 4$  and 6 mm. The insulation permittivity was again taken as  $\epsilon_{r2} = 1$  with an external medium of permittivity  $\epsilon_{r4} = 32$ .

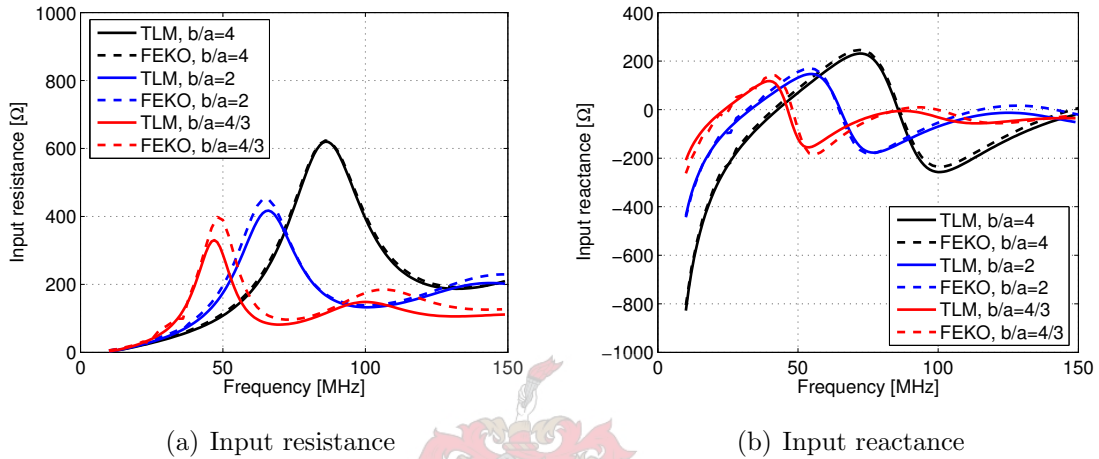


**Figure 2.12:** Comparison of input impedance from Chen and Warne's model with that of FEKO for an insulated dipole antenna with different insulation diameters

The modelled input impedance is hence not very accurate when  $|k_4^2|/|k_2^2|$  is much below 8 and the ratio of insulation to inner conductor radii  $\frac{b}{a}$  is small. The BHR antenna in a typical host rock environment has  $|k_4^2|/|k_2^2| \approx 3$ , while the conductive arm of the antenna has  $\frac{b}{a} = \frac{8}{7}$ . It is hence expected that the input impedance calculated from Chen and Warne's transmission line model will not correspond well to simulation results in the latter environment.

Figure 2.13 compares the input impedance from the transmission line model of the borehole radar antenna for environments of homogeneous water ( $\epsilon_{r4} = 81, \sigma_4 = 10$  mS/m), homogeneous rock ( $\epsilon_{r4} = 9, \sigma_4 = 0$ ) and a 50 mm diameter air-filled borehole in typical host rock ( $\epsilon_{r4} = 9, \sigma_4 = 0$ ). In the lossless environment of typical host rock, a small conductivity was again added to the transmission line model's ambient medium to avoid the occurrence of unphysical input impedance results.

The modelled input impedance and the simulation data agree to great accuracy in homogeneous water, however the amplitudes and resonant frequency values differ considerably in homogeneous rock and the air-filled borehole. The transmission line model predicts the resonance that occurs in the latter environments to have a higher Q-factor than predicted by the MoM results. Figures 2.13(c) and 2.13(d) illustrate that only when

the transmission line model's ambient medium conductivity is substantially increased ( $\sigma_4 = 10 \text{ mS/m}$ ) does the resonance become sufficiently damped to be comparable with the MoM results. The model hence performs as expected, corresponding well to simulated results in water, but having diminished accuracy in typical host rock environments.

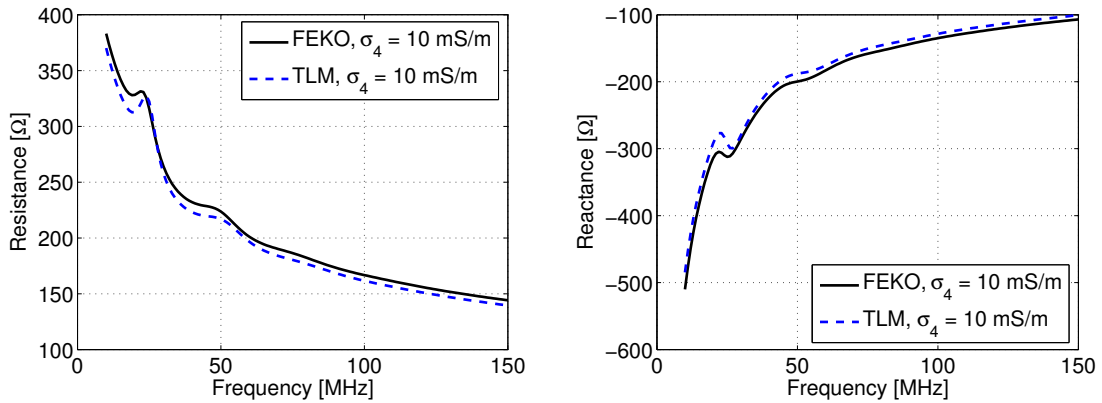
Although the input impedance results from the transmission line model are generally not accurate predications, the converse was found to be true for the predicated radiated electric fields. The directivity of the borehole radar antenna predicted by FEKO and the transmission line model for the latter three environments are compared in Figure 2.14. It is seen that the results are virtually identical.

## 2.4 Conclusions

The transmission line model of insulated antennas was shown to have several drawbacks. Firstly, it cannot be used to model water-filled boreholes. Chen and Warne's transmission line model was furthermore shown to give unphysical input impedance results with lossless ambient media and cannot give accurate predictions of the input impedance of the BHR antenna in typical host rock environments. The transmission line model is hence unsuitable for a study of the variation of input impedance of the borehole antenna in air- and water-filled boreholes and the numerical models CST Microwave Studio or FEKO will have to be utilized for this purpose.

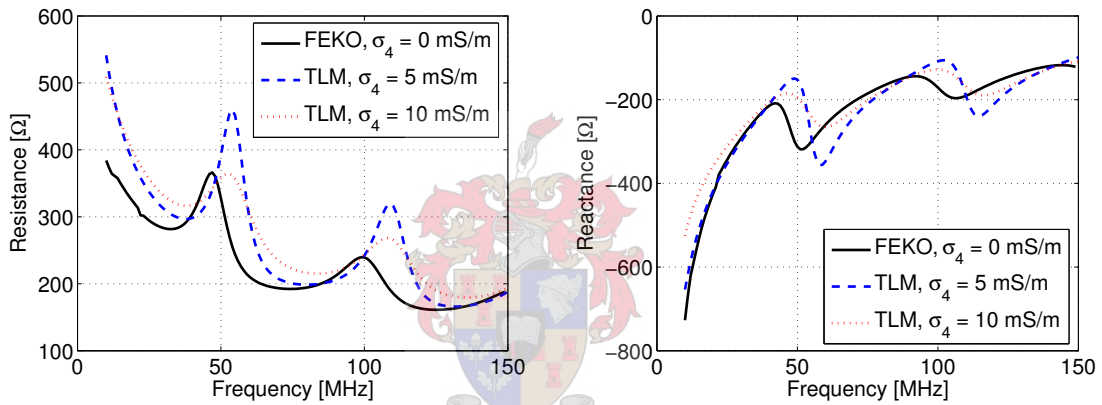
The radiated electric field predicted by both the numerical models and the transmission line model were however found to be in good agreement, giving confidence in the validity of the results.

CST Microwave Studio holds the advantage that it contains a time-domain solver, while the transmission line model and the MoM implemented in FEKO are frequency domain solutions. Quantities such as current distribution and radiated field may hence be calculated directly in the time-domain, while the precise form of the time-domain excitation may be specified. For this reason CST Microwave studio is most suited for the study of the time- and frequency domain behaviour of the antenna in different borehole environments.



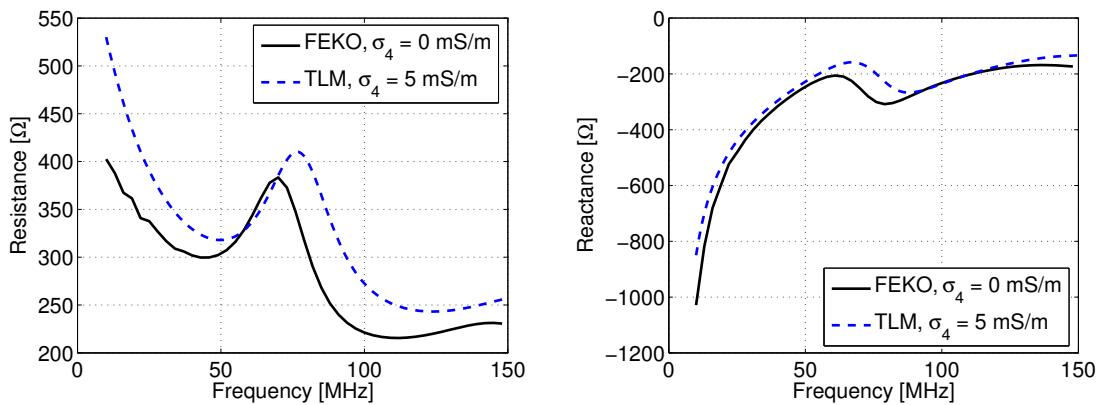
(a) Input resistance, homogeneous water

(b) Input reactance, homogeneous water



(c) Input resistance, homogeneous rock

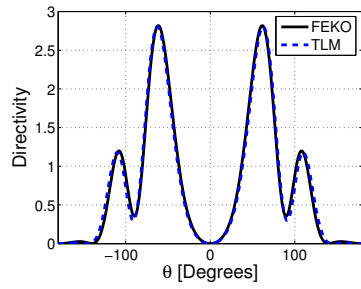
(d) Input reactance, homogeneous rock



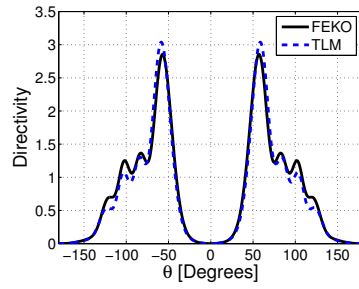
(e) Input resistance, 50 mm air-filled borehole

(f) Input reactance, 50 mm air-filled borehole

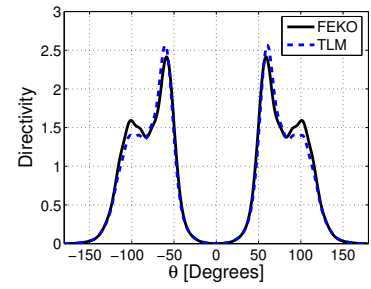
**Figure 2.13:** Comparison of input impedance from Chen and Warne’s model with that of FEKO for the BHR antenna in different borehole environments



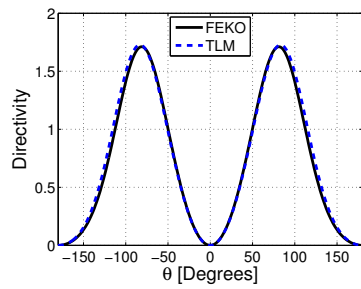
(a) Homogeneous water, 50 MHz



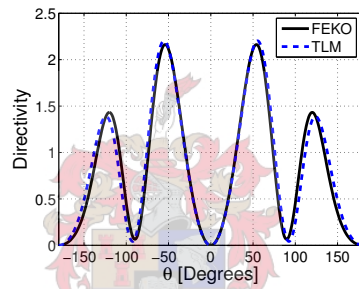
(b) Homogeneous water, 100 MHz



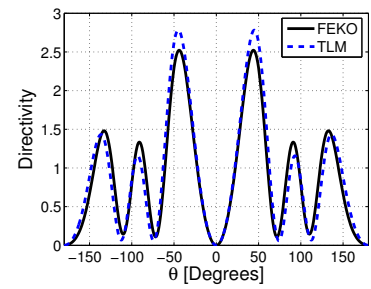
(c) Homogeneous water, 150 MHz



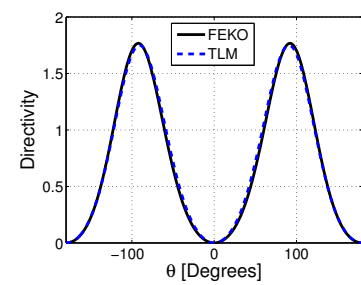
(d) Homogeneous rock, 50 MHz



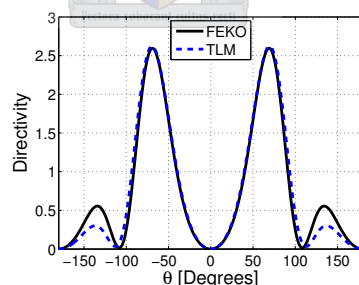
(e) Homogeneous rock, 100 MHz



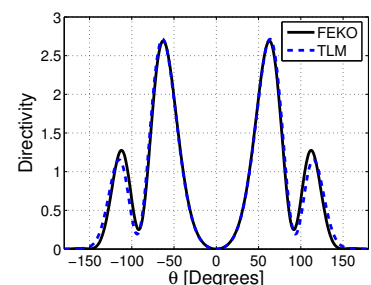
(f) Homogeneous rock, 150 MHz



(g) 50 mm air-filled borehole, 50 MHz



(h) 50 mm air-filled borehole, 100 MHz



(i) 50 mm air-filled borehole, 150 MHz

**Figure 2.14:** Comparison of borehole antenna directivity predicted by FEKO and the transmission line model of insulated antennas

# Chapter 3

## Parametrical studies

The performance of the BHR antenna in different borehole environments will now be assessed through studying its feed-point and radiation characteristics.

An accurate representation of the antenna input impedance inside different borehole environments is needed and, due to the failure of the Smith and King Transmission Line model in this respect, the only resort is the use of simulation models, namely either FEKO or CST Microwave Studio as introduced in Chapter 2. CST Microwave studio was chosen as the most suitable simulation environment, due to its capability to simulate directly in the time-domain.

The model of the BHR antenna in CST Microwave Studio is as described in section 2.2.1. The antenna model is furthermore immersed in a cylindrical layer of material representing the borehole. This cylinder need not be longer than the antenna itself, since, at the frequencies of interest, the cylinder cannot support any propagation modes in the absence of a central conductor.

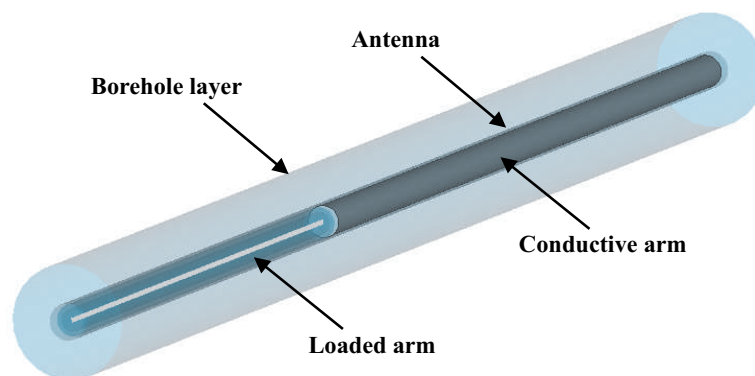


**Figure 3.1:** *The CST Microwave Studio model of the BHR antenna inside a borehole*

### 3.1 General comments on current distribution

Insight into the BHR antenna's behaviour in different media may be gained in considering its time-domain current distribution obtained via simulation. The antenna was driven with Gaussian voltage pulse of length 5 ns using a discrete port with a  $1 \Omega$  internal impedance. The simulated current distribution on the borehole radar was extracted by probing the axial H-field at regular intervals along the antenna. The results from a 75 mm air-filled and a 75 mm water-filled borehole is shown in Figure 3.2. The antenna feed-point is located at  $z=0$ , with the resistive arm positioned along the positive  $z$ -axis.

In both the air-filled and the water-filled borehole, the Gaussian pulse at  $t \approx 0$  is seen to propagate outward on the antenna arms. Current along the resistively loaded arm is attenuated, with no reflections occurring at its end-point. Current along the unloaded arm is not attenuated significantly and is reflected from the unloaded arm end-point back to the feed-point. The reflected pulse is again partially reflected at the feed-point, with some current being transmitted through to the loaded arm. Multiple end-point / feed-point reflections occur, especially in the case of the water-filled borehole, until the current is dissipated through radiative or conductive losses.

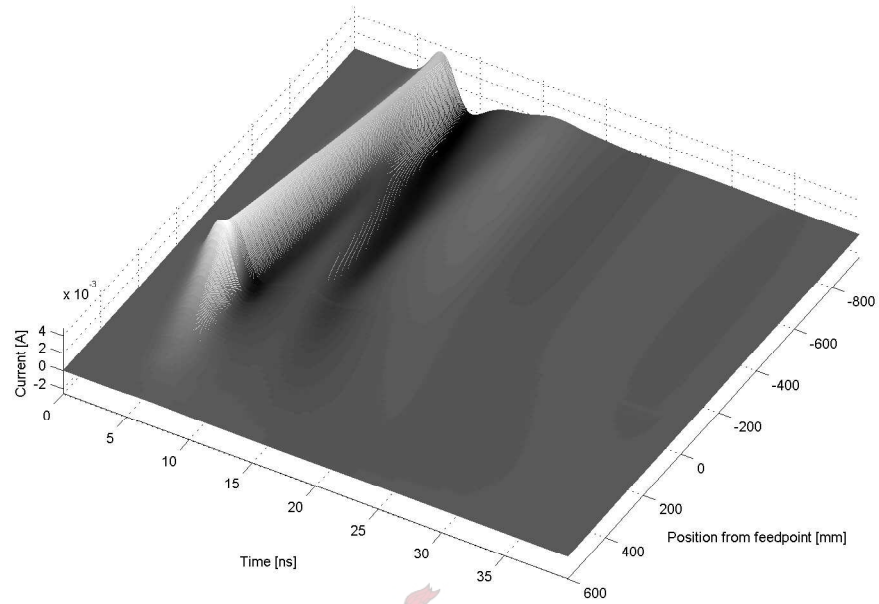
The most noticeable difference between the current distributions of the air-filled and water-filled borehole in Figure 3.2 is the difference in group velocity of the current wave traveling along the conductive antenna arm. An equivalent permittivity corresponding to the pulse's group velocity,  $\epsilon_{eq} = (c/v_g)^2$  may be defined. The value of  $\epsilon_{eq}$  is high when the material in close proximity to the antenna is of high permittivity and *vice versa*. Pulse velocities will hence be slower in water-filled than air-filled boreholes. Furthermore, the current pulse velocities in air-filled boreholes will be lower the narrower the borehole, while in water-filled boreholes the velocity will be lower the wider the borehole.

Recovery of the current at the feed-point will be slower in environments where the pulse group velocity along the antenna is low, due the longer times taken for reflected current pulses to return to the feed-point. Figure 3.2 illustrates that in water-filled boreholes the pulse dissipation occurs more slowly than in air, allowing multiple end-point/feed-point reflections and consequently leading to a slower feed-point current recovery.

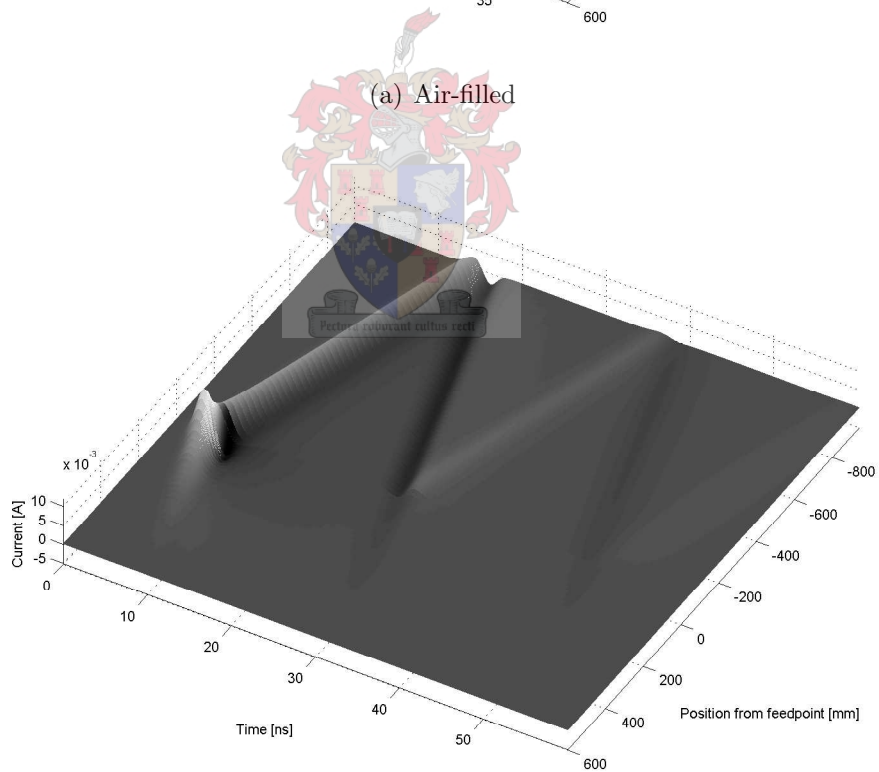
Reflection of current from the end-point of the conductive arm implies that the effects of resonance will be present in antenna frequency domain characteristics such as input impedance, radiation efficiency and radiation patterns. As the time between the arrival of reflected pulses at the feed-point increases (due a decreasing group velocity), the frequency intervals between the occurrence of resonance will decrease.

It is known that, classically, radiation is caused by the acceleration of charge. The BHR antenna's radiation mechanisms are therefore:

- (a) Separation of charge at the feed-point by an external source



(a) Air-filled



(b) Water-filled

**Figure 3.2:** *The current distribution simulated in CST Microwave Studio for an air-filled borehole and a water-filled borehole both of diameter 75 mm*

- (b) Deposition of charge on the continuous resistively loaded arm as current pulses propagate along its length [19]
- (c) Reflection of current pulses from the conductive arm end-point and the antenna feed-point

When prolonged end-point/feed-point reflections occur, such as in water-filled boreholes as illustrated in Figure 3.2(b), the radiated field pulse is hence expected to be severely stretched in time.

A study of the time-domain current distribution hence suggests that the use of the radar antenna in electrically dense environments such as water-filled boreholes will have a detrimental effect on the feed-point current recovery and the radiated field of the antenna. The following sections will investigate this in more detail.

## 3.2 Input impedance

The input impedance of the borehole antenna model in CST Microwave studio was computed using the waveguide feed mechanism as described in section 2.2.1. The radius and material properties of the borehole cylinder was varied as to simulate particular borehole environments. The antenna input impedance was obtained for the following set of borehole parameters:

- Borehole diameter: 50 mm, 60 mm, 75 mm, 100 mm, 140 mm, 200 mm
- Borehole material properties:
  - air:  $\epsilon_r = 1$ ;  $\sigma = 0$
  - water:  $\epsilon_r = 81$ ;  $\sigma = 0, 1 \text{ mS/m}, 10 \text{ mS/m}, 100 \text{ mS/m}$

where  $\sigma$  represents the electrical conductivity of the material. The antenna was placed in an ambient medium with  $\epsilon_r = 9$ , representing the relative permittivities of typical host rock environments.

The input resistance from all simulations was seen to increase substantially at lower frequencies, however more notably so in water-filled boreholes. The input reactance appears similar to that of a capacitor, however with resonant effects superimposed at regular intervals. The input reactance furthermore remains negative over the entire band due to the effect of the resistively loaded arm.

A comparison of selected input impedance results for the antenna in air-filled boreholes of differing diameter is shown in Figure 3.3. The velocity of current waves propagating along the unloaded antenna arm is slower the narrower the air-filled borehole, as described in the section 3.1. Time domain current reflections from the unloaded arm will hence

arrive at the feed-point at longer intervals in narrower boreholes, corresponding to lower resonant frequencies in the input impedance data. This is clearly illustrated in Figure 3.3, where the frequency of the first resonance increases with increasing borehole diameter.

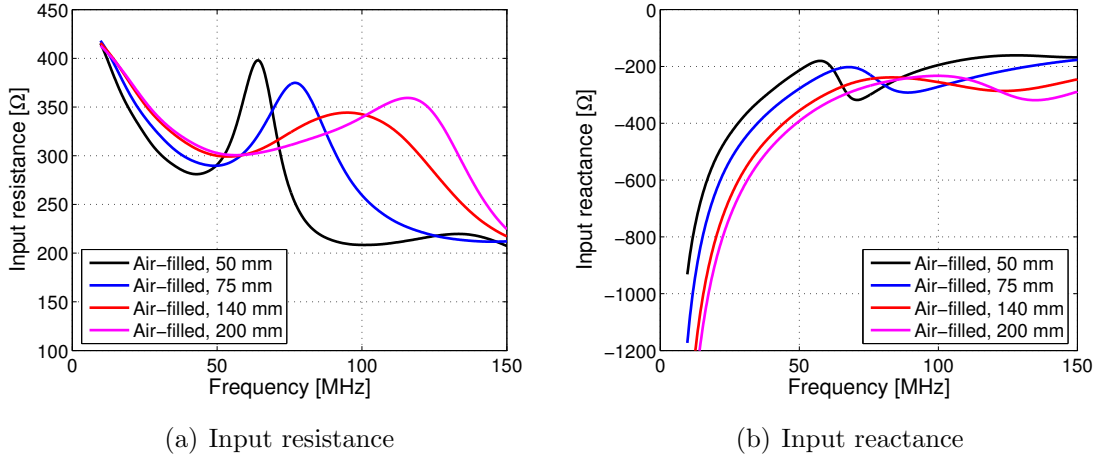


**Figure 3.3:** *Input impedance of the borehole radar antenna in air-filled boreholes of varying diameter*

A comparison of selected input impedance results for the antenna in water-filled boreholes of differing diameter is shown in Figure 3.4. As described in the section 3.1, the group velocity of current waves propagating along the unloaded antenna arm is slower the wider the water-filled borehole. The time domain current reflections from the unloaded arm will arrive at the feed-point in longer intervals in wider boreholes, corresponding to the smaller frequency intervals between resonance as seen in Figure 3.4.

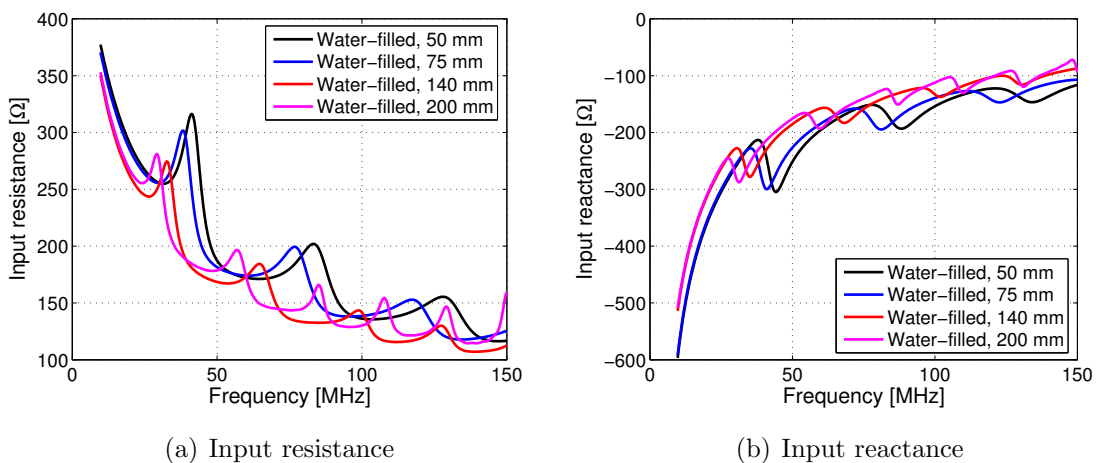


**Figure 3.4:** *Input impedance of the borehole radar antenna in water-filled boreholes of varying diameter*

Figure 3.5 illustrates the substantial difference in input impedance between an air- and water-filled borehole of 75 mm diameter. The equivalent permittivity is substantially higher in the water-filled borehole, leading to smaller group velocities and hence smaller intervals between resonance, as described above. The input resistance and reactance in the water-filled borehole is substantially smaller, as may be expected due to the substantial increase in effective permittivity. Figure 3.5 also illustrates the influence of water conductivity: Higher conductivities lead to damped resonance, however the input impedance remains in essence the same.

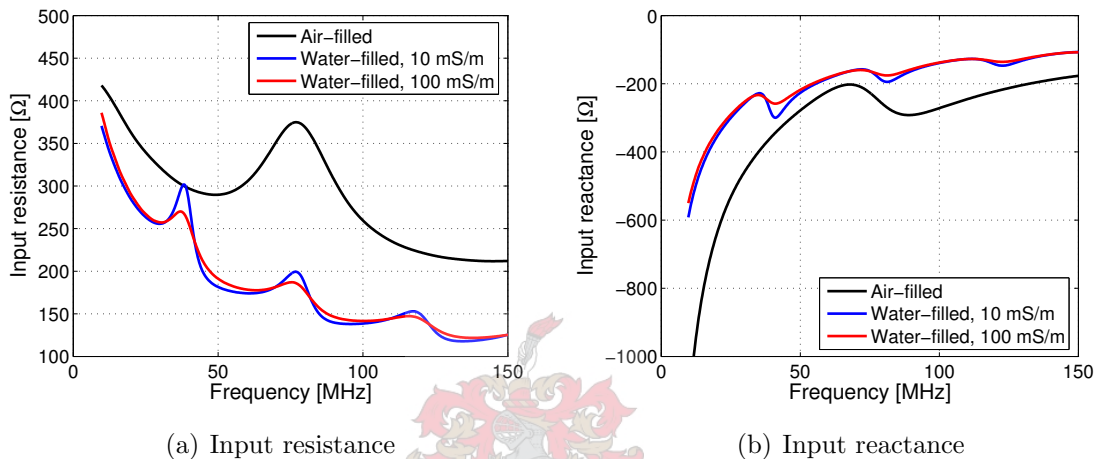


**Figure 3.5:** *Input impedance of the borehole radar antenna in 75 mm diameter air-filled and water-filled boreholes with differing water conductivity*

### 3.3 Feed-point current

#### 3.3.1 Feed-point current recovery

Long feed-point current recovery times after the transmitter firing was suspected to be the main cause of loss of close range radar data due to saturation of the radar receiver in water-filled boreholes. A study of the antenna feed-point current recovery in different borehole environments is hence of great importance since longer recovery times may impact negatively on the performance of the monostatic radar system.

An on-board current probe utilizing the radar system's existing ADC and data logger was constructed by Paul van der Merwe [28] to investigate the feed-point current recovery in air- and water-filled boreholes. Subsequent measurements confirmed that substantially longer current recovery times are present in water-filled boreholes.

The radar system's ADC however imposed several limitations on the performance of the on-board current probe. The peak discharge current amplitude could not be logged

accurately due to the ADC's 4 ns sampling period. The peak current amplitude and the much smaller amplitudes of current recovery could not be monitored simultaneously due to the limited measuring range and resolution of the ADC. The data was furthermore strongly affected by EMI and calibration showed the probe's measurement to be accurate only after  $\sim 40$  ns after the transmitter firing [28].

This section will consequently also study the variation in feed-point current in different borehole environments through simulation, by integrating the input impedance data from the previous section with an accurate simulation model of the radar circuitry.

Advanced Design System (ADS) from Agilent EEsof<sup>1</sup> was utilized in the detailed modelling of the radar circuitry. The circuit model was simplified by replacing the entire gain stage with a  $200\ \Omega$  resistor, which is essentially the input impedance of the LNA in the frequency band of interest. The circuit model as implemented in ADS is shown in Figure 3.6. Details surrounding the implementation of the T/R-switch are not relevant.

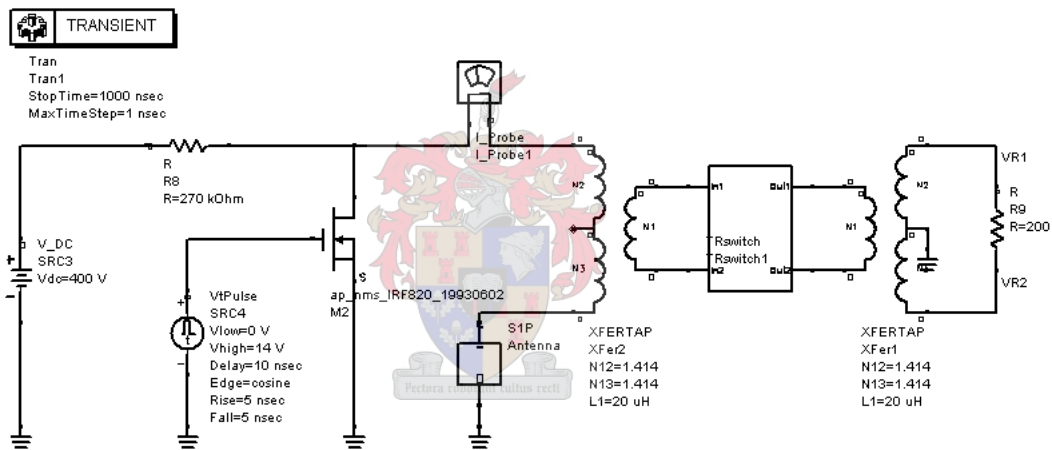


**Figure 3.6:** *The simplified model of the BHR receiver circuit in ADS*

The inclusion of the antenna in the circuit model occurs through specifying its feed-point characteristics using the so-called *1-port S-parameter block* in ADS, labeled 'Antenna' in Figure 3.6. The S-parameter block imports simulated  $S_{11}$  data of the antenna in a specific borehole environment, realizing the antenna in the circuit simulation as a one-port load. The interaction of the antenna and the radar circuitry may be characterized in the time-domain through use of ADS's time domain circuit simulator, allowing detailed study of the feed-point current as the transmitter fires.

Results show the recovery of the feed-point current is generally similar to the exponential discharge of a simple RC circuit. Reflected current pulses from the conductive arm end-point are furthermore clearly superimposed on the exponential curve at regular

<sup>1</sup><http://eesof.tm.agilent.com/>

intervals.

Figure 3.7(a) illustrates the substantial difference between the feed-point current recovery in a 75 mm air-filled and 75 mm water-filled borehole. The peak current amplitude is higher in the water-filled borehole while the current pulses reflected from the conductive arm end-point arrive much later in the water-filled borehole. These differences correspond to an increase in effective permittivity due to the presence of a material of high permittivity in close proximity to the antenna. Figure 3.7(a) also illustrates that the effect of increased water conductivity is to slightly damp the amplitude of the reflected current pulses. The instantaneous power corresponding to the current,  $I(t)^2 R$ , is shown on a logarithmic scale in Figure 3.7(b), normalized to the peak current from the air-filled borehole. On the logarithmic scale it is clear that the residual levels of current long after the firing of the transmitter are much higher in the water-filled borehole.

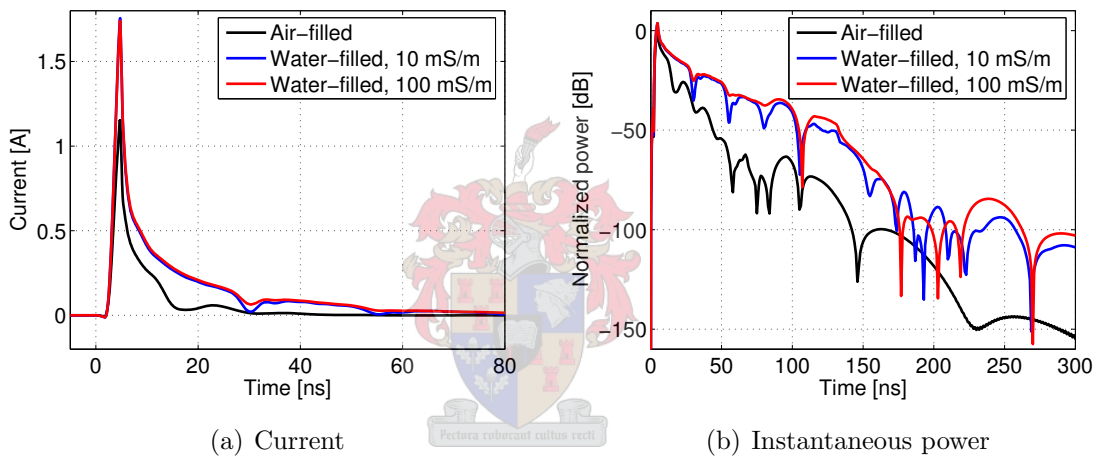


**Figure 3.7:** Recovery of current after transmitter firing for 75 mm air-filled and water-filled boreholes

Feed-point currents of the antenna from selected air-filled boreholes are shown in Figure 3.8(a). The peak current amplitude increases as the borehole diameter decreases and the end-point reflections clearly arrive at the feed-point earlier the wider the air-filled borehole. These changes are consistent with an increase of effective permittivity due to the closer proximity of the electrically dense ambient medium to the antenna. The instantaneous power corresponding to the current is shown on a logarithmic scale in Figure 3.8(b), normalized to the peak current from the 50 mm borehole. On the logarithmic scale it is clear that the residual levels of current long after the firing of the transmitter are higher the narrower the air-filled borehole.

The feed-point current for water-filled boreholes 100 mm and smaller (water conductivity 10 mS/m) are shown in Figure 3.9(a). Results are as expected, with the reflections from the conductive arm arriving sooner the narrower the water-filled borehole,

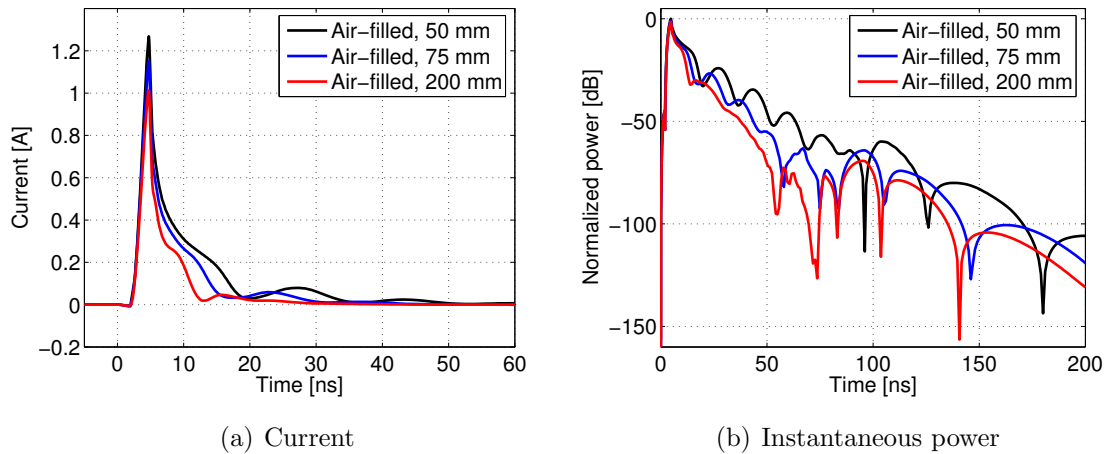


**Figure 3.8:** Recovery of current after transmitter firing for selected air-filled boreholes

corresponding to a decrease in effective permittivity due to less material having a high permittivity being in close proximity to the antenna.

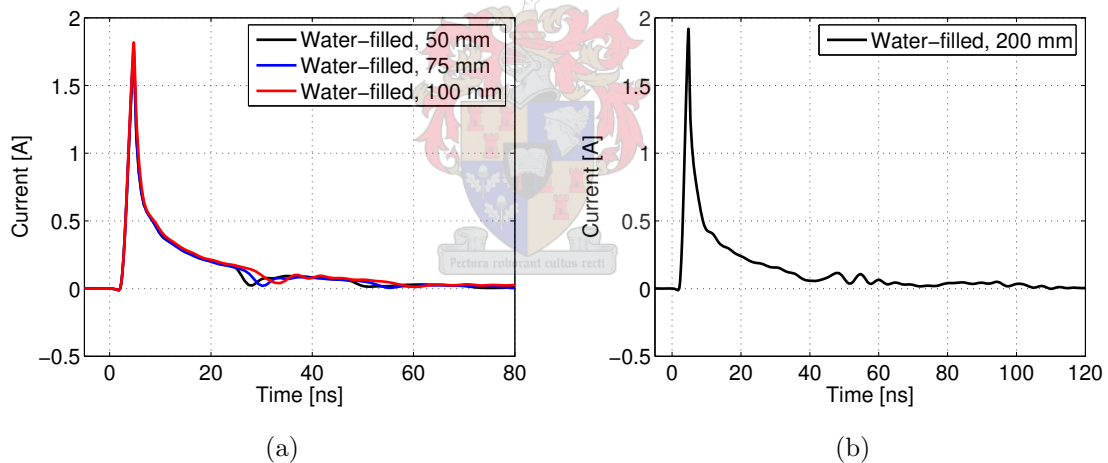


**Figure 3.9:** Recovery of current after transmitter firing for selected water-filled boreholes

In boreholes with diameters larger than 75 mm, a small resonance unexpectedly occurs in the feed-point current data, superimposed at regular intervals on the reflected current pulses, as illustrated for a 200 mm water-filled borehole in Figure 3.9(b). The resonance is seen more clearly in a plot of the instantaneous power level in Figure 3.10, normalized to the peak power of the 50 mm borehole. Figure 3.10 furthermore shows that the residual current levels at times long after the transmitter fired is substantially higher for boreholes of diameter 100 mm and larger. The appearance of the resonance hence coincides with a sudden substantial increase in residual current levels, which may have a negative impact

on the performance of the radar system.

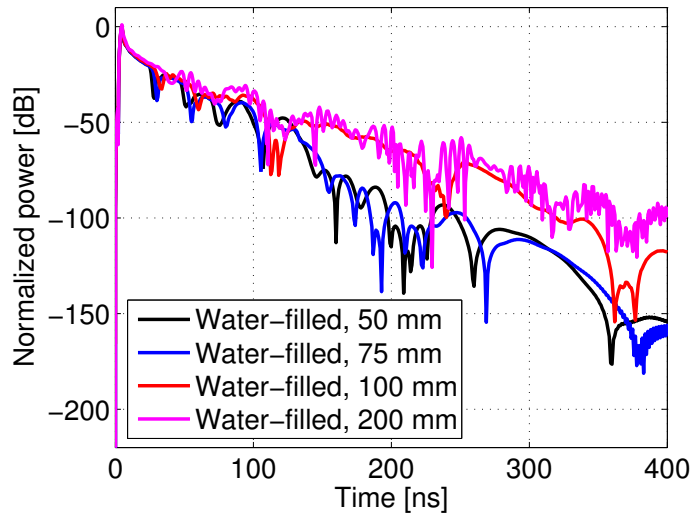


**Figure 3.10:** Recovery of the instantaneous power at the feed-point for selected water-filled boreholes

Simulations of the current distribution along the antenna in such wide water-filled boreholes shows the presence of a new propagation mode along the antenna corresponding to the observed resonance effects as in Figure 3.9(b). The exact mechanism of propagation is however as yet unknown and is subject to further investigation. Evidence of such a propagation mode has furthermore been seen experimentally in wide water-filled boreholes, as will be shown in Chapter 5.

### 3.3.2 Output voltage recovery

A secondary goal of the circuit simulations is to determine when the input voltage to the ADC is within its sampling range, in other words when the ADC's output appears saturated and total data loss occurs. The approximate output voltage waveform from the ADC may be computed by simply scaling the output voltage of the T/R-switch with the total gain from the gain stage between the T/R-switch output and the ADC input. A diagram of the gain stage is shown in Figure 3.11.

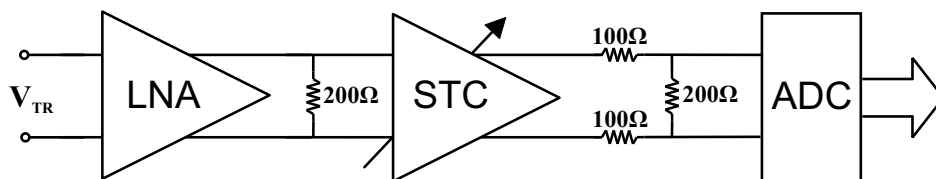


**Figure 3.11:** A schematic of the gain stage after the T/R-switch

The LNA provides a gain of 20 dB while the STC amplifier provides a time-dependent gain of 11 to 46 dB. The STC and the ADC have high input impedances while the STC also has a low output impedance. Resistive matching networks as shown in Figure 3.12 were hence added to minimize reflection of input power. The resistive matching network between the STC and the ADC effectively acts as a 6 dB attenuator due to voltage division. The total gain is hence given by  $A_{dB}(t) = 14 \text{ dB} + A_{STC}(t)$ .  $A_{STC}(t)$ , the time-dependent gain of the STC, was measured experimentally, to give a total gain  $A_{dB}$  that appears in Figure 3.12

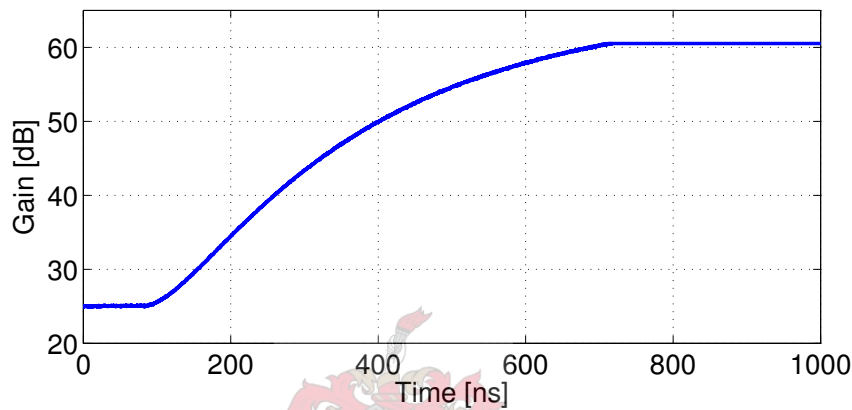


**Figure 3.12:** *The total time-dependent gain of the amplifier stage*

The output voltage  $V_{out}$  may now be computed by numerically scaling the T/R-switch output with the gain illustrated in Figure 3.12; hence

$$V_{out} = V_{TR} 10^{\frac{A_{dB}(t)}{20}}$$

and clipping the resulting voltage at  $\pm 0.5 \text{ V}$ . The simulated output voltage from a 75 mm air- and water-filled borehole is shown in Figure 3.13. Qualitatively the simulated output voltage appears greatly similar to the experimental radar traces. The simulated trace momentarily saturates at time  $t=0$  when the transmitter fires due to the large peak current flowing through the feed-point and the fact that the isolation is not ideal. Saturation occurs again at  $t \approx 80 \text{ ns}$  due to large levels of feed-point current present when the T/R-switch switches to through-mode. The output voltage finally leaves saturation when the T/R-switch stabilizes in through-mode and feed-point current levels are sufficiently diminished. In practice total data loss typically occurs until this point.

The time at which signal comes out of saturation, after which no more data loss occurs, may be taken as a measure of the radar systems performance in the associated medium. This measure will be termed the *recovery time*. The recovery times for numerous air- and water-filled boreholes were determined by simulation of the radar output trace and is listed in Table 3.1.

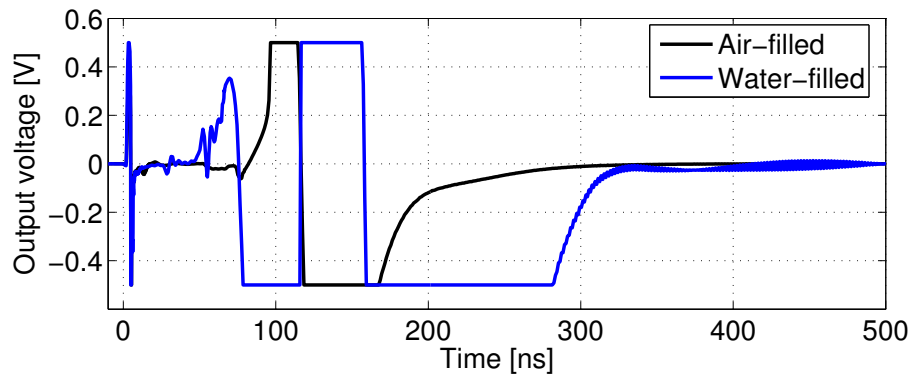


**Figure 3.13:** *Simulated radar traces for 75 mm air- and water-filled boreholes*



**Table 3.1:** *Simulated recovery times in different borehole environments*

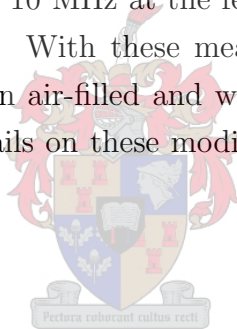
Borehole diameter [mm]	Recovery time [ns]	
	Air-filled	Water-filled, 10 mS/m
50	211	278
60	201	275
75	173	278
100	165	325
140	156	402
200	152	407

The variation of recovery time generally corresponds to that of the level of residual feed-point current on the antenna. In an air-filled borehole the recovery time decreases with an increase in borehole diameter. In water-filled borehole the recovery time is predicted to be relatively constant for boreholes with diameters less than 75 mm and less, while with diameters of 100 mm and above it increases dramatically due to the appearance of the resonance effects described earlier.

The above circuit simulations do predict a dramatic increase in recovery times in water-filled boreholes over air-filled boreholes, however the increase is not sufficient to explain the 2  $\mu$ s (total data loss) observed experimentally in some water-filled boreholes. It is suspected that the increase in residual feed-point current levels compounded existing problems in the receiver system design to lead to total data loss.

Several modifications to the receiver design was made by P.J. van der Merwe as measures to reduce the prolonged saturation observed in water-filled boreholes [28]. The LNA and STC amplifiers were AC-coupled and the onset of the STC gain increase was delayed by 144 ns. A measure that proved most effective was the inclusion of a high-pass current filter with a cut-off frequency of 10 MHz at the feed-point, only allowing high frequency signals through to the receiver. With these measures implemented the BHR antenna could be operated successfully in air-filled and water-filled boreholes without prolonged saturation occurring. More details on these modifications to the receiver system will be presented in Chapter 5.

### 3.4 Radiated field



The antenna was driven with a discrete port with internal impedance of 1  $\Omega$  to compute the time-domain radiated field of the borehole antenna. The discrete port voltage was chosen to mimic the drain voltage of the driver MOSFET that causes the antenna discharge, shown in figure 3.6, as to approximate the time-domain waveforms of the radiated field as closely as possible. The port voltage source is taken as:

$$V_{dp} = \begin{cases} 0 & t < 0 \\ 390(1 - e^{-\frac{t}{10}}) & 0 < t < t_0 \\ 390 \left( \frac{1}{2} - \frac{1}{2} \tanh [0.7(t - t_0 - 5)] \right) & t > t_0 \end{cases} \quad (3.1)$$

with  $t_0 > 0$ . The curve for  $t < t_0$  represents the charging cycle of the antenna and is much quicker than in practice since the only interest in this instance is in the radiated field at the firing of the transmitter, in other words the discharge cycle. It was found that  $t_0 = 300$  ns is sufficient for all transient currents from the charging of the antenna to have subsided. The antenna terminals are charged to a maximum voltage of  $\sim 390$  V. The curve in equation 3.1 for  $t > t_0$  was chosen to fit the drain voltage of the source

FET at the time of the discharge cycle. The correspondence between the measured and approximated curve is shown in Figure 3.14.

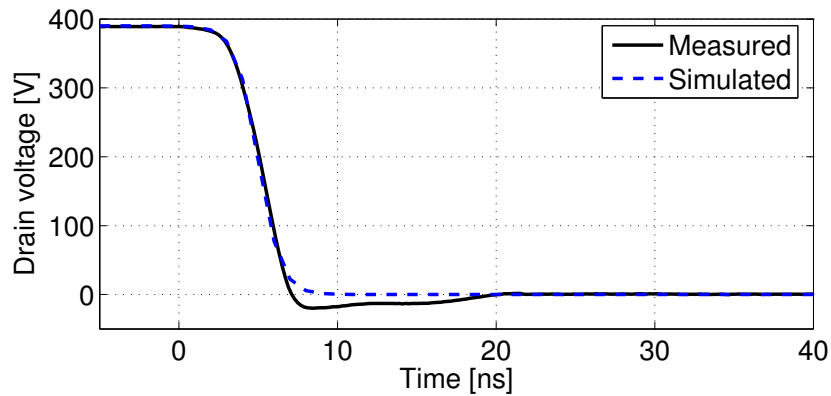


**Figure 3.14:** *Measured and simulated drain voltage*

Only the  $\theta$ -component of the radiated electric field is nonzero since the antenna is  $z$ -directed. The  $\theta$ -component of the radiated electric field at broadside was measured at a distance of 10 m using the radiated electric field probes of CST Microwave Studio.

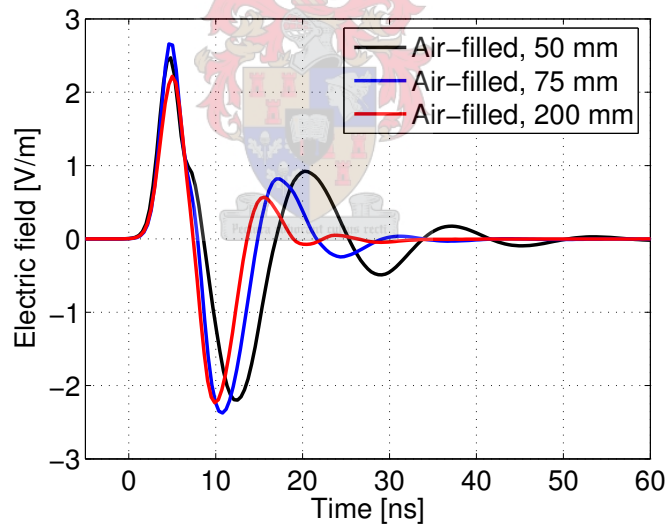


**Figure 3.15:** *Radiated electric field at a distance of 10 m at broadside for selected air-filled boreholes from CST Microwave Studio simulations*

The radiated field from selected air-filled boreholes is shown in Figure 3.15. The radiated pulse is sharper the larger the diameter of the air-filled borehole. In narrower boreholes the pulse is characterized by a prolonged ringing originating from multiple end-point/feed-point reflections on the conductive arm of the antenna, as described in section 3.1.

The radiated field from selected water-filled boreholes is shown in Figure 3.16. The radiated pulses shown are greatly stretched in comparison to that seen in air-filled bore-

holes. The prolonged ringing seen in the radiated pulses is again due to reflections of current pulses at the conductive arm end-point and the feed-point of the antenna. This corresponds to expectations stated in section 3.1 in which current pulses along the conductive arm in water-filled boreholes were seen to have a much slower propagation speed and slower dissipation than in air-filled boreholes. The extra propagation mode that appears in boreholes with diameter larger than 75 mm also has a significant effect on the radiated pulse. The radiated pulses in Figure 3.16(b) for boreholes with large diameters are significantly longer than that of the narrower boreholes in Figure 3.16(a).

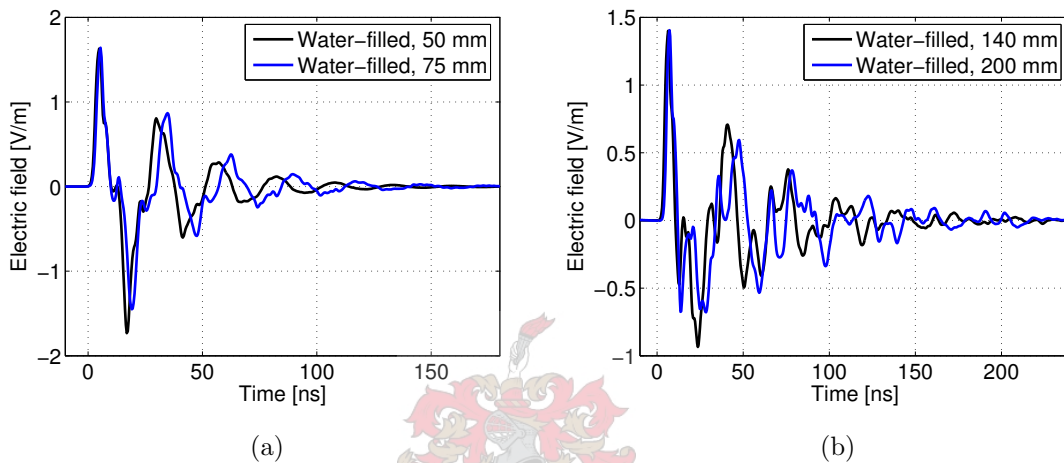


**Figure 3.16:** Radiated electric field at broadside of selected water-filled boreholes

The stretching of the radiated field pulse of the antenna in water-filled boreholes represents a significant limit on the performance of the borehole radar antenna. Figure 3.17 compares the radiated field of a 75 mm air-filled and a 75 mm water-filled borehole of different water conductivities. The pulse in the air-filled borehole is sharp, closely resembling an ideal monocycle pulse. The pulse from the water-filled borehole however is wider by a factor of 3, drastically reducing the effective resolution of the radar system. The radiated pulse is furthermore composed of several distinct pulses originating from radiation occurring from reflections at conductive arm end-point and feed-point. A radiated pulse of latter form may lead to false identification of targets.

The more traditional radiation patterns of the antenna in different borehole environments were also investigated. The antenna is orientated with the loaded arm along the positive  $z$ -axis. Figure 3.18(a) shows the directivity of a 75 mm air-filled borehole for several frequencies. At low frequencies the directivity is similar to that of an infinitesimal dipole. At frequencies higher than 50 MHz the radiation patterns however *squints* to the side of the conductive arm, while a sidelobe forms above 100 MHz with an unwanted null occurring at broadside.

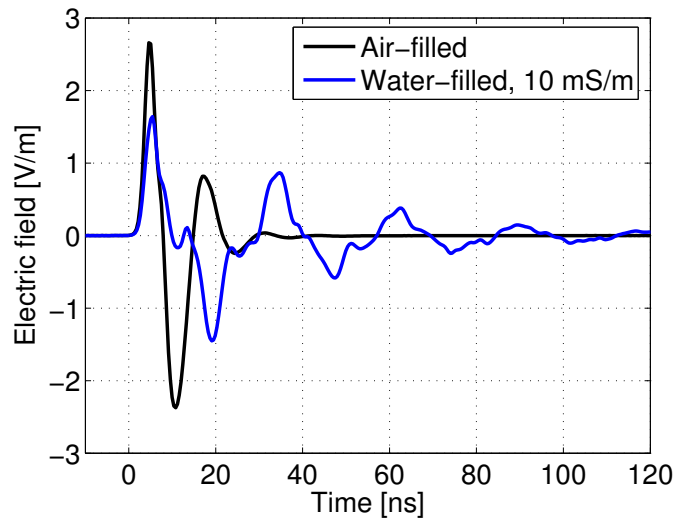


**Figure 3.17:** Radiated electric field at broadside of a 75 mm air-filled and a water-filled boreholes

The frequency dependence of the radiation pattern of the water-filled borehole, shown in Figure 3.18(b) is similar to that of the air-filled borehole, with the difference that the radiation pattern starts to degrade at a much lower frequency. At 10 MHz the field is still similar to that of an electrically small dipole, however a significant sidelobe is already present at 50 MHz, while multiple sidelobes are seen at 100 MHz.

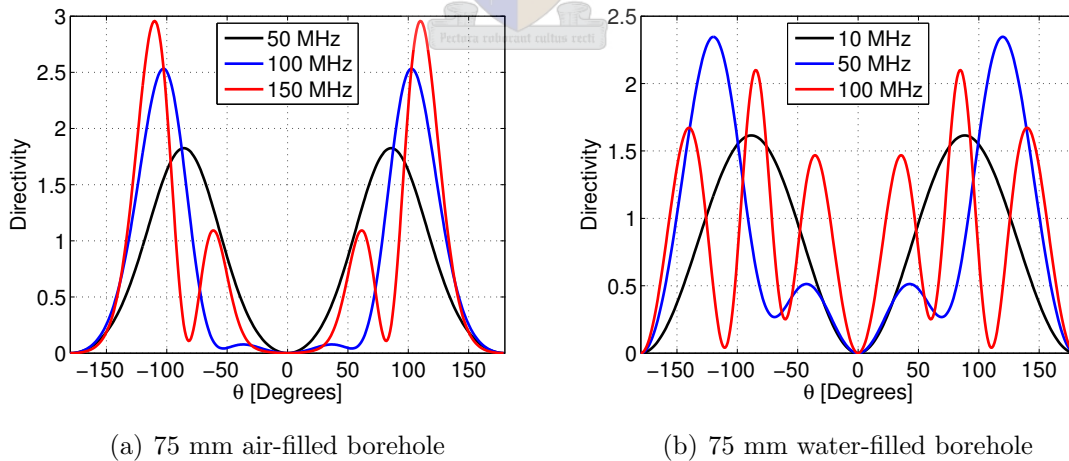


**Figure 3.18:** Variation of directivity with frequency in 75 mm air-filled and water-filled boreholes

The deterioration of the radiation pattern occurs more rapidly with increasing frequency when the borehole antenna is in electrically dense media where propagation speeds of current along the antenna are smaller. This is furthermore illustrated in Figure 3.19(a) for air-filled boreholes of different diameter at 100 MHz. The *squint* of the main lobe

clearly increases with a decrease in diameter of the air-filled borehole, with a significant sidelobe forming at a diameter of 50 mm. Figure 3.19(b) illustrates the same process for water-filled boreholes of different diameter at 50 MHz. In this case the environment becomes electrically denser as the borehole diameter increases, and consequently the radiation pattern degrades with increasing borehole diameter.

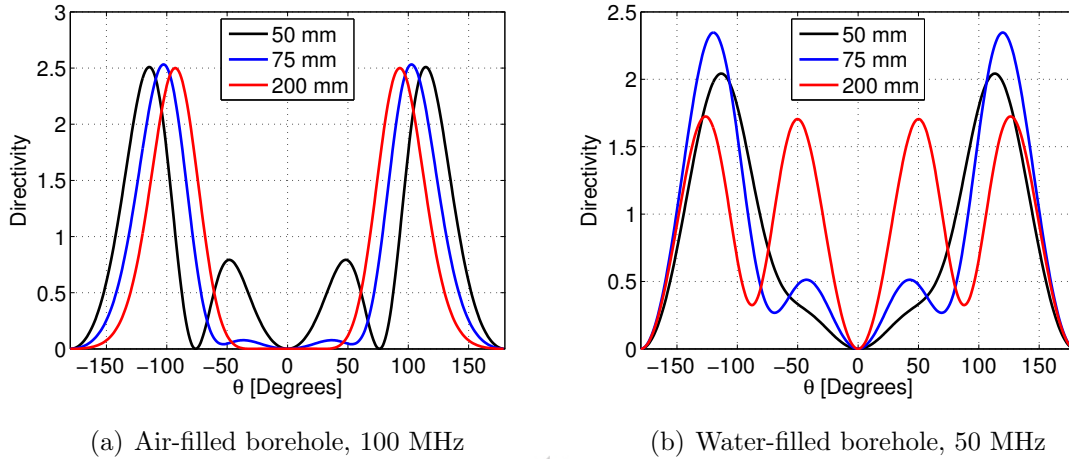


**Figure 3.19:** Variation of directivity with borehole diameter at a given frequency

### 3.5 Conclusions

The simulations performed in this chapter illustrated a drastic deterioration in performance of the BHR antenna in water-filled with respect to air-filled boreholes.

Simulations showed that the antenna discharge current after the firing of the transmitter has a much longer settling time than in air-filled boreholes, confirming observations from measurements of the current in water-filled boreholes. The simulated output of the receiver gain stage furthermore confirmed that the longer discharge current settling times in water-filled boreholes lead to prolonged saturation of gain stage amplifiers and data loss.

The radiated electric field waveform is drastically degraded and stretched in water-filled boreholes, which has dire consequences for the performance in terms of the radar system in terms of resolution.

Based on the simulations conducted in this chapter, the BHR antenna is not ideal for use in water-filled boreholes. The problem of slowly discharging antenna current may be solved without much difficulty, as noted in section 3.3.2 and discussed in more detail in section 5.1. The degraded radiated field waveform is however caused by multiple reflections from discontinuities along the antenna and cannot be improved without physically modifying the structure of the antenna.

# Chapter 4

## Feed-point models

### 4.1 Introduction

It is often necessary to perform diagnostic measurements on a borehole radar system when the antenna load resembles that when the radar is deployed in a borehole environment. However doing this while the system is physically deployed in a borehole is of course impossible. This problem is circumvented by replacing the antenna with a lumped element load mimicking the input impedance of the antenna when in a typical borehole environment. This enables diagnostic measurements to be performed on the laboratory workbench, with the antenna load behaving as if the system were deployed inside a borehole.

Initially, the input impedance of the borehole antenna in a dense medium was expected to be similar in nature to that of a Wu-King dipole<sup>1</sup>, namely a resistance in series with a capacitance [31], the values of which were chosen heuristically. It soon became clear that this model does not hold for an antenna in a water-filled boreholes, as is evident when studying the simulated BHR antenna input impedance in Chapter 3. The need therefore exists for simple lumped element circuits that approximate the antenna input impedance for a range of different air- and water-filled boreholes to a good accuracy over a wide frequency band, namely 0 to 100 MHz.

In this chapter, antenna input impedance data from the *CST Microwave Studio* simulation environment for a range of different boreholes is used together with well known circuit synthesis methods to synthesize simple lumped element circuits. An overview of the network synthesis methods evaluated, and the eventual method used is presented in section 4.2. Equivalent circuits for a range of different boreholes are given in Section 4.3, created from the input impedance data used for the parametric studies in Chapter 3. In section 4.4, the simulated feed-point currents using a synthesized load and the corresponding simulated, numerical load are compared to evaluate the accuracy of the synthesized

---

<sup>1</sup>Introduced in more detail in Chapter 5

load.

## 4.2 Driving-port impedance synthesis methods

The object of driving-port network synthesis is to physically realize a lumped element network with a specified input (driving-port) impedance  $Z(s)$ , a function of the complex frequency variable  $s$ . This section outlines methods to approximate numerical input impedance data with an impedance function  $Z(s)$ , and to synthesize a corresponding one-port network using only resistive, inductive, capacitive and mutual inductive elements.

### 4.2.1 Complex curve fitting of input impedance data

As will be shown in the next section, the impedance to be synthesized,  $Z(s)$ , must be a rational function of  $s$  of form

$$Z(s) = \frac{b_0 + b_1s + b_2s^2 + \dots + b_ms^m}{a_0 + a_1s + a_2s^2 + \dots + a_ns^n} \quad (4.1)$$

to be realizable using only the abovementioned lumped elements.

Synthesizing a circuit with driving-port impedance equivalent to simulated antenna input impedance data, requires that the data must be converted into an approximately equivalent impedance function in the form 4.1. This corresponds to fitting the curve

$$Z(s = j\omega) = \frac{b_0 + b_1(j\omega) + b_2(j\omega)^2 + \dots + b_m(j\omega)^m}{a_0 + a_1(j\omega) + a_2(j\omega)^2 + \dots + a_n(j\omega)^n} \quad (4.2)$$

in complex space to the numerical complex impedance data over the supplied frequency range. The polynomial coefficients  $b_i$  in the numerator and  $a_i$  in the denominator thus have to be determined to minimize the error between the curve 4.2 and the supplied complex impedance data for given polynomial degrees  $m$  and  $n$ . This is of course a least squares problem.

A complex curve fitting algorithm that is essentially a linear least squares method, has been developed by Levi [18]. The algorithm is relatively simple to implement and gives adequate results. However, the algorithm does not guarantee that the resultant curve will correspond to a stable system since it may contain RHP poles and hence not be realizable with a passive network. An algorithm supplied with *Matlab* improves on the above by using an iterative Gauss-Newton-method with the fitting from Levi's algorithm as initial estimate. The algorithm gives a much better fitting and furthermore ensures that the resulting fitted impedance function will only have LHP poles.

The quality of the fit may be manipulated by varying the order of the impedance function, the parameters  $m$  and  $n$  in 4.3. The use of a higher order impedance function is needed for a good fit of the numerical data. Choosing lower values of  $m$  and  $n$  lessens

the accuracy of the fit, effectively smoothing out some of the features in the curve. This is illustrated in Figure 4.1, where  $9^{\text{th}}$  ( $m = n = 9$ ) and  $3^{\text{rd}}$  ( $m = n = 3$ ) order curves were fitted to the simulated antenna input impedance in a 50 mm diameter water-filled borehole. The  $9^{\text{th}}$ -order function fits the first two resonant peaks, while the  $3^{\text{rd}}$ -order function averages out all resonant peaks.

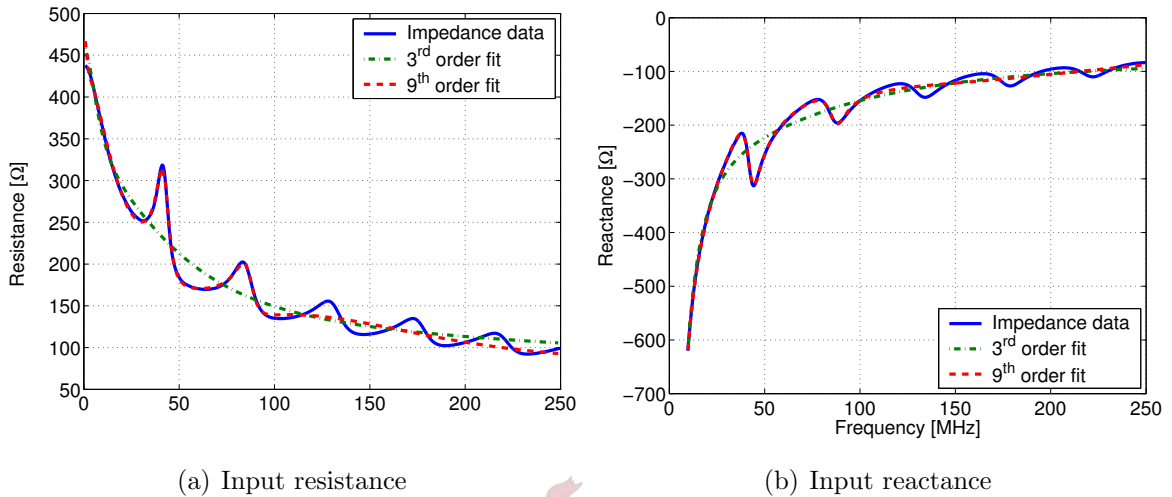


**Figure 4.1:** Comparison of fitted curves using different order impedance functions

The complex curve fitting algorithm supplied by *Matlab* was found to be adequate in generating impedance functions of form 4.1 that approximately correspond to simulated antenna input impedance data. The fitted impedance function  $Z(s)$  must however satisfy certain conditions if it is to be realizable using lumped circuit elements. This is the subject of the next section.

## 4.2.2 Positive real rational functions

In a landmark paper by Otto Brune [2], it is shown that an impedance function  $Z(s)$  is realizable using only resistive, inductive, capacitive and mutual inductive elements *if and only if* the following conditions hold:

- (a)  $Z(s)$  is a real rational function of  $s$ ; that is:

$$Z(s) = \frac{b_0 + b_1s + b_2s^2 + \dots + b_ms^m}{a_0 + a_1s + a_2s^2 + \dots + a_ns^n} \quad (4.3)$$

where all coefficients  $a_i$  and  $b_i$  are real.

- (b) If the real part of  $s$  is nonnegative, then the real part of  $Z(s)$  must also be nonnegative:

$$\text{Re}[s] \geq 0 \implies \text{Re}[Z(s)] \geq 0 \quad (4.4)$$

If a given impedance function  $Z(s)$  satisfies the conditions (a) and (b), it is known as *positive real* (PR). It may be shown that if a impedance  $Z(s)$  is PR, then so is the associated admittance  $Y(s) = \frac{1}{Z(s)}$ . An impedance function must be verified as PR if it is to be successfully synthesized. Testing a function  $Z(s)$  for condition (a) is trivial, unlike condition (b). A set of conditions equivalent to (b), but more convenient for testing, is [26]:

$$(b') \operatorname{Re}[Z(j\omega)] \geq 0 \text{ for all real } \omega$$

(c') All poles of  $Z(s)$  are in the left half complex plane (LHP);  $j\omega$ -axis poles are simple, with positive real residues.

Testing for condition (c') is trivial in an environment like *Matlab*, where the roots of the denominator in 4.3 can be easily determined. Testing for condition (b') is more involved, but may be simplified by rewriting 4.3 as

$$Z(s) = \frac{N_e(s) + N_o(s)}{D_e(s) + D_o(s)} \quad (4.5)$$

where  $N_e$  and  $N_o$  denote the sum of terms respectively containing even and odd powers of  $s$  in the numerator of 4.3, while  $D_e$  and  $D_o$  denote the same for the denominator polynomial. Now, defining:

$$P(\omega^2) = N_e(j\omega)D_e(j\omega) - N_o(j\omega)D_o(j\omega) \quad (4.6)$$

the condition (b') is equivalent to  $P(\omega^2) \geq 0$  for all real  $\omega$ . If we further substitute  $x \equiv \omega^2$  into 4.6, we find:

$$P(x) = c_0 + c_1x + c_2x^2 + \dots + c_nx^n \quad (4.7)$$

For condition (b') to hold, it is sufficient to test that  $c_0$  and  $c_n$  are positive and that  $P(x)$  has no odd-order zeros on the positive x-axis.

Conditions (a) and (b) are now in a form where the PR character of a function  $Z(s)$  may be tested easily in an environment like *Matlab*.

### 4.2.3 Overview of synthesis from arbitrary impedance functions

#### General remarks

The expressions for the  $s$ -plane impedance of lumped circuit elements, such as resistors, capacitors, inductors as well as series and parallel combinations thereof, are well known. If an impedance function  $Z(s)$  is similar to such an expression, it may be synthesized merely by inspection.

$Z(s)$  is however generally too complex to permit synthesis by inspection. In this case the complexity of  $Z(s)$  may be reduced by subtracting the  $s$ -plane impedance expression of a familiar lumped physical component in an attempt to reduce the order of  $Z(s)$ . Similarly the  $s$ -plane admittance of a lumped component may be subtracted from  $Y(s) = \frac{1}{Z(s)}$ . Hence  $Z(s)$  or  $Y(s)$  may be expressed as a sum of two terms:

$$Z(s) = Z_1(s) + Z_R(s) \quad (4.8)$$

$$Y(s) = Y_1'(s) + Y_R'(s) \quad (4.9)$$

where  $Z_1(s)$  ( $Y_1'(s)$ ) represents the impedance (admittance) of some physical component and  $Z_R(s)$  ( $Y_R'(s)$ ) is the remainder function. Subtracting the impedance (admittance) of a lumped element corresponds to the realization of a series impedance (shunt admittance) branch, as illustrated in Figure 4.2.

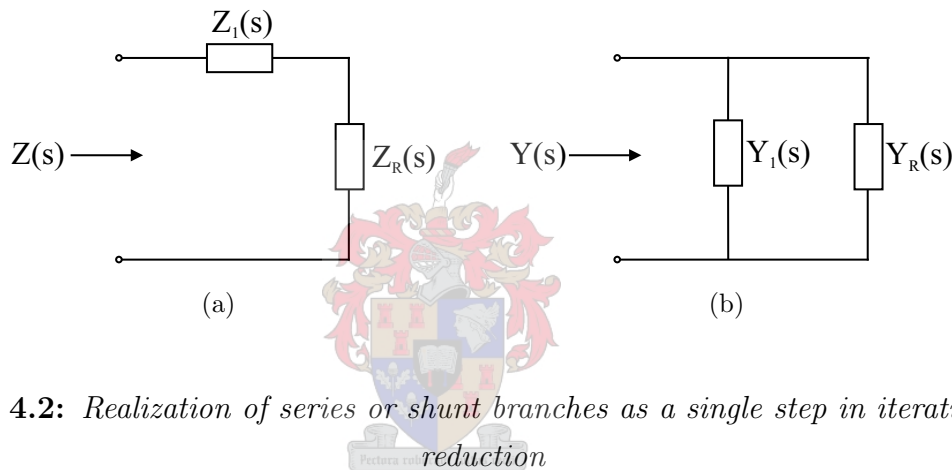


**Figure 4.2:** Realization of series or shunt branches as a single step in iterative order

reduction

Another reduction of order by the above process may be attempted on either one of  $Z_R(s)$  or  $Y_R(s) = \frac{1}{Z_R(s)}$  or either of  $Y_R'(s)$  or  $Z_R'(s) = \frac{1}{Y_R'(s)}$ . It could hence be attempted to completely realize  $Z(s)$  by systematically reducing its order to zero through continued repetitions of this process using the subsequent remainder functions. This will yield a physical realization of the original impedance function if, at all iterative steps:

- (a) the remainder function is PR; and
- (b) the remainder function is of lower order than its predecessor.

In some instances it is possible to express either  $Z(s)$  or  $Y(s)$  directly as a sum of recognizable terms by using the partial fraction expansion method. An example of this is the synthesis of two-element-type networks, which will be discussed in a following section.

### Pole and constant removal

The process of order reduction described above is formalized by Temes and LaPatra [26] in an algorithm where either a constant or a function corresponding to a simple pole at

$s = 0$  or  $s = \infty$ , or complex conjugate poles at  $s = \pm j\omega_i$  is iteratively subtracted from the remainder impedance or admittance function. A removed constant simply corresponds to a resistance when subtracted from an impedance remainder and to a conductance when subtracted from an admittance. Poles that are removed from an impedance function correspond to the circuits and impedance functions shown in 4.3, while those removed from admittance functions shown in Figure 4.4.

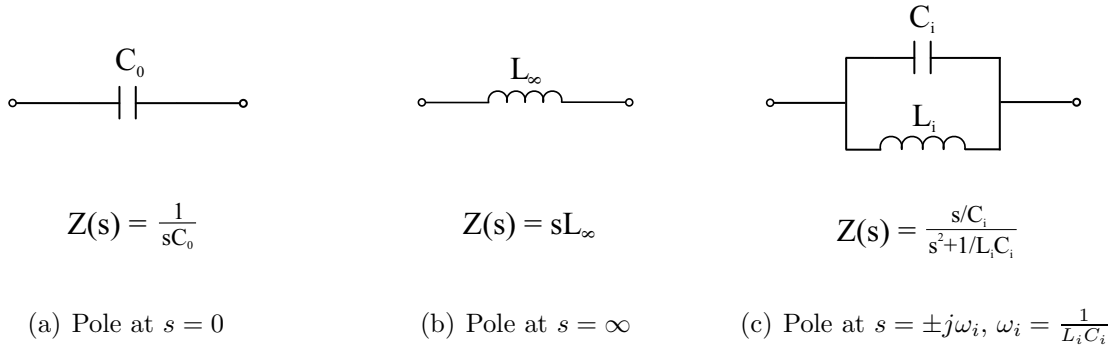


**Figure 4.3:** Series impedance branches realized by removing poles at  $s = 0$ ,  $s = \infty$  and  $s = \pm j\omega_i$  from an impedance function

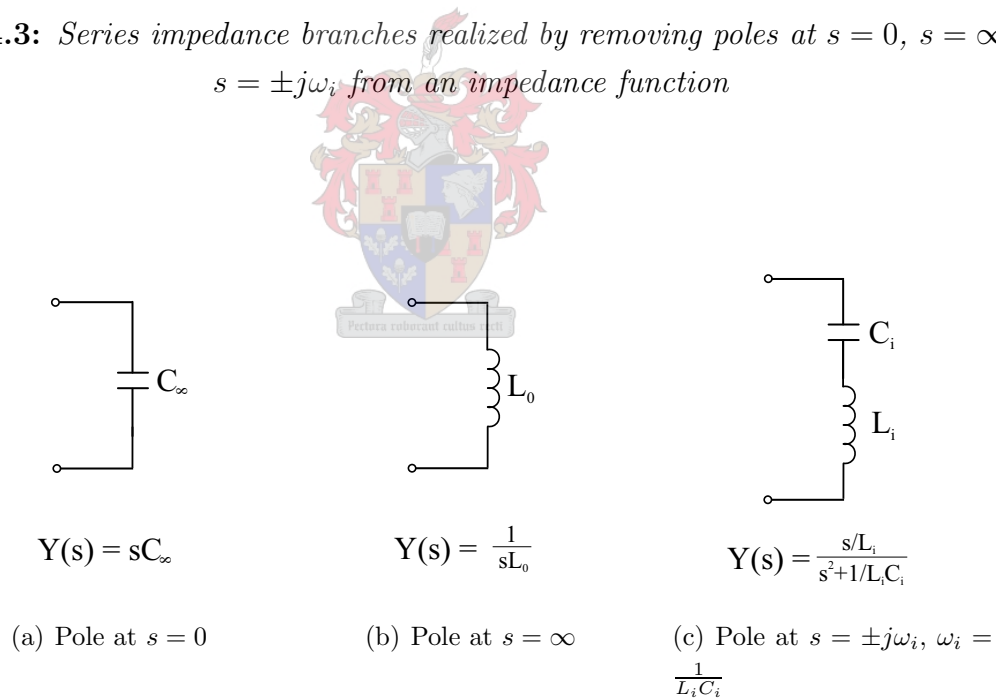


**Figure 4.4:** Series admittance branches realized by removing poles at  $s = 0$ ,  $s = \infty$  and  $s = \pm j\omega_i$  from an admittance function

The residues of the poles of the circuits in Figures 4.3 and 4.4 are computed via the partial fraction expansion method and, by the PR property of  $Z(s)$ , will be real and positive.

The algorithm is given as [26]:

1. Test  $Z(s)$  for poles at  $s = 0$ ,  $s = \infty$  or  $s = \pm j\omega$ . If found, remove by subtracting the corresponding impedance function; thereby realizing a series reactance branch.
2. Test the remainder admittance,  $Y_R(s)$ , for poles at  $s = 0$ ,  $s = \infty$  or  $s = \pm j\omega$ . If found, remove by subtracting the corresponding admittance function; thereby realizing a shunt reactance branch. Return to step 1 and iteratively repeat steps 1 and 2 until the remainder impedance and admittance function contain no poles at  $s = 0$ ,  $s = \infty$  or  $s = \pm j\omega_i$ .
3. Find the minimum value of the *real part* of the remainder impedance  $Z_R(j\omega)$  (or admittance  $Y_R(j\omega)$ ) and subtract this value, thereby realizing a series resistance (shunt conductance).

The above algorithm will only realize the original impedance function if, at all iterative steps, the real part of the remainder function  $Z(j\omega)$  has a minimum at  $\omega = 0$  or  $\omega = \infty$ . If the real part has a minimum at some finite non-zero frequency, poles will not have real residues and realization of physical components as in Figures 4.3 and 4.4 will be impossible; and removing a pole corresponding to a physical component will destroy the PR character of the remainder. If the minimum is removed via constant removal, the function will have a zero at some finite non-zero frequency. Such a function is termed a *minimum impedance*, and cannot be reduced in order by the iterative removal of poles as in the algorithm above while still keeping its PR property.

The algorithm was implemented in the *Matlab* environment to synthesize an impedance function found by using the curve fitting methods in Section 4.2.1. Using an impedance function from a low-order fit not including any resonance effects, resulted in successful synthesis of the impedance function by order reduction. The circuits synthesized consisted only of resistors and capacitors and were identical in form to the well known Cauer realizations of RC circuits [26]. These results will however not be shown at this stage, since there exist much simpler algorithms than iterative order reduction to synthesize circuits containing only two types of elements. This will be the subject of section 4.2.4.

Using high-order impedance functions that included resonance effects from the impedance data, the synthesis algorithm was always disrupted by the occurrence of minimum impedance functions at some stage in the iterative order-reduction process. Inclusion of resonance effects would hence require a method for synthesizing minimum impedance functions.

### Synthesis of minimum impedances

Brune solved the problem of synthesizing minimum impedances in his landmark 1931 paper [2]. His solution, synthesis of a so-called *Brune section*, is unfortunately very limited, since it involves the use of an ideal transformer. Synthesis of Brune sections

would not be a practical solution for our intended application, and hence the details of the method will not be entered into.

A synthesis method for minimum impedances that avoids use of ideal transformers was subsequently developed by Bott and Duffin [1], proving that arbitrary impedance functions are always synthesizable using only resistors, capacitors and inductors. The Bott-Duffin method and variants thereof unfortunately have a great disadvantage, in that a large number of elements are required for synthesis. The number of elements required increase exponentially with the order of the impedance function to be synthesized [9]. Inclusion of resonance effects require the use of high order impedance functions in the curve-fitting stage. As was seen in Figure 4.1, a 9<sup>th</sup> order impedance function is needed to fit the first few resonant peaks of the antenna impedance. The Bott-Duffin method is hence also not suited for this application.

Attempts to synthesize simple, transformerless networks with driving-port impedances that take resonance effects in the antenna input impedance over a wide frequency band into account, will thus be unsuccessful. The following sections will focus on simple synthesis methods that may be used when neglecting resonance effects.

### Network simplification on neglecting resonance effects

It was shown in the previous section that the synthesis process will only yield simple, transformerless circuits when the resonance effects in the antenna input impedance data are neglected. As noted in section 4.2.1, this may be accomplished by fitting an impedance function 4.3 with low-order numerator and denominator polynomials to the impedance data in the curve fitting stage.

A network of which the driving-port impedance may contain no resonance effects cannot be synthesized using both inductors and capacitors. Considering the simulated antenna input reactance in all boreholes is entirely negative and appear to exhibit the presence of a pole near  $\omega = 0$ , it is clear that, in this case, neglecting resonance must result in synthesis using only resistive and capacitive elements. This furthermore explains why synthesis from the general iterative order reduction algorithm using low-order impedance functions resulted in networks containing only resistors and capacitors.

The next section proposes a method for synthesizing RC networks much simpler than the general algorithm described in this section.

## 4.2.4 Synthesis of RC impedances

The term *RC impedance* denotes the driving-point impedance of a network constructed exclusively from resistors and capacitors. This section describes the properties of the driving-port impedance of RC networks and a simple algorithm for synthesis of impedance

functions that share these properties.

### Properties of RC impedances

An RC driving-point impedance  $Z(s)$  and the corresponding admittance  $Y(s) = \frac{1}{Z(s)}$  can be shown [26] to have the following properties:

- $Z(s)$  and  $Y(s)$  have simple poles and zeros alternating on the finite negative real axis of the  $s$ -plane.
- For  $Z(s)$  the lowest critical frequency is a pole, while for  $Y(s)$  it is a zero
- The residues of  $Z(s)$  at its poles are real and positive, while that of  $Y(s)$  are real and negative.

The residues of  $\frac{Y(s)}{s}$  at its poles can be shown to be real and positive, a fact that will be used in the synthesis scheme discussed in the next section.

For the impedance function obtained via curve-fitting to be realizable, it must satisfy the above conditions, which are clearly more strict than the PR requirement in section 4.2.1. It is found that since the curve fitting is done on the input impedance of a physical system that is approximately an RC impedance, the fitted impedance function shares these characteristics and as a rule does not violate the above conditions.

### Foster RC synthesis

A simple method for synthesizing circuits with only two kinds of elements, namely the Foster Type 2 method, will be used. Hereby the circuit is synthesized from the partial fraction expansion of  $Y(s) = \frac{1}{Z(s)}$ . Practically, the partial fraction expansion of  $\frac{Y(s)}{s}$  is computed, since, by the properties stated in the previous section, it always gives positive residues at its poles. Since all zeros of  $Y(s)$  are simple and poles are on the real negative  $s$ -plane axis, the partial fraction of  $\frac{Y(s)}{s}$  is as follows:

$$\frac{Y(s)}{s} = k_{\infty} + \frac{k_0}{s} + \sum_{i=1}^n \frac{k_i}{s + \sigma_i} \quad (4.10)$$

where  $k_i$  and  $\sigma_i$  are real and positive. Multiplication of 4.10 by  $s$  then gives a partial fraction expansion representation for  $Y(s)$  where all residues are positive:

$$Y(s) = k_{\infty}s + k_0 + \sum_{i=1}^n \frac{k_i s}{s + \sigma_i} \quad (4.11)$$

Each term in 4.11 may be identified with the admittance of simple lumped circuit elements: The terms  $k_{\infty}s$  and  $k_0$  respectively correspond to the admittance of a lumped

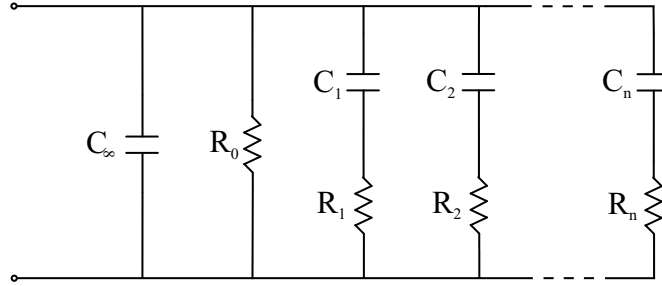


**Figure 4.5:** Network corresponding to the Foster 2 expansion of an RC admittance

capacitor and resistor. Considering the admittance of a resistor and capacitor connected in series:

$$\begin{aligned}
 Y(s)_i &= \frac{1}{R_i + \frac{1}{C_i s}} \\
 &= \frac{\frac{1}{R_i} s}{s + \frac{1}{R_i C_i}}
 \end{aligned} \tag{4.12}$$

it is clear that the terms in 4.11 correspond to series RC branches, with  $k_i = \frac{1}{R_i}$  and  $\sigma_i = \frac{1}{R_i C_i}$ .

It follows that the partial fraction expansion 4.11 corresponds to the circuit shown in Figure 4.5, where the lumped element values are given by:

$$C_\infty = k_\infty \tag{4.13}$$

$$R_0 = \frac{1}{k_0} \tag{4.14}$$

$$C_i = \frac{k_i}{\sigma_i}, \quad R_i = \frac{1}{k_i} \tag{4.15}$$

Since  $k_i$  and  $\sigma_i$  are assured positive by the stated properties of  $Y(s)$ , the values of  $R_i$  and  $C_i$  are assuredly real and positive.

Implementing the above synthesis process algorithmically is trivial in an environment such as *Matlab*. The poles and corresponding residues in the partial fraction expansion 4.10 is easily computed using the *Matlab* function **residue**.

### 4.3 Lumped element models for a range of different borehole environments

This section presents networks with driving point impedance approximately equal to that of an borehole antenna inside a range of borehole environments. These networks were synthesized using the Foster RC network synthesis methods presented in the previous section

from simulated antenna input impedance data from the parameter study simulation of Chapter 3.

Networks were synthesized using  $3^{rd}$  and  $2^{nd}$  order impedance functions, neglecting resonance effects in the input impedance data. Element values are not given in standard component values, but in their calculated form to 3 significant digits.

Caution must be taken in attempting to attach physical significance to the component values of the synthesized networks. It must be noted that the mapping of the band-limited input impedance data in complex space to the s-plane expression  $Z(s)$  of equation 4.1 is not one-to-one. Varying input parameters of the curve fitting algorithm may result in differing component values for the synthesized networks, however with driving-port impedances that are approximately equal. The equivalent network and its component values must hence only be seen as giving an approximation to the antenna input impedance in a specific environment and not to be characteristic of the borehole antenna as a system. Certain trends are however evident in the component values with changing borehole radius and these will be pointed out.

### 4.3.1 Equivalent circuits for water-filled boreholes

The set of simulation data from which the circuits are to be synthesized contain input impedance data not only from water-filled boreholes of different diameters, but also of varying water conductivity. As seen in Chapter 3, the effect of water conductivity is to damp resonance effects. Since the synthesis algorithm in its nature ignores resonance effects, a network synthesized for a borehole of certain diameter will hence not vary significantly as function of water conductivity. For this reason, networks were synthesized only for different borehole diameters; each being valid irrespective of the water conductivity.

Surprisingly, it was found that even a  $2^{nd}$  order impedance function gives an adequate approximation to the antenna input impedance. Using a  $3^{rd}$  order impedance functions however gives rise to a somewhat more accurate approximation. Both  $3^{rd}$  and  $2^{nd}$  order circuits are hence presented.

The  $3^{rd}$  order circuits, synthesized using  $m = n = 3$  in 4.3 appear as in Figure 4.6. The component values synthesized for water-filled boreholes of different diameter are shown in table 4.1.

The values of  $R_4$  are several orders larger than the other resistors and it may effectively be replaced by an open circuit.

The form of the synthesized network using a second-order impedance function  $Z(s)$  ( $m = n = 2$  in 4.3) appears as in Figure 4.7. The corresponding component values are shown in table 4.1.

The values of  $R_3$  are several orders larger than the other resistors and it may effectively be replaced by an open circuit.

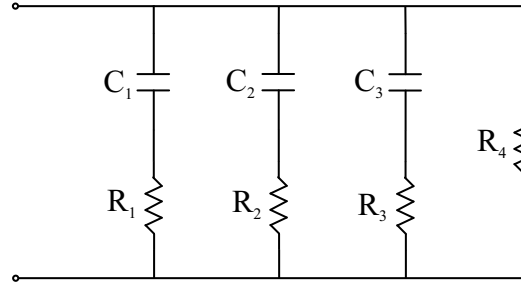


**Figure 4.6:** Network synthesized using a 3<sup>rd</sup> order impedance function

**Table 4.1:** Elements values in Figure 4.6 for a water-filled borehole

Borehole diameter (mm)	$R_1(\Omega)$	$R_2(\Omega)$	$R_3(\Omega)$	$R_4(\Omega)$	$C_1(\text{pF})$	$C_2(\text{pF})$	$C_3(\text{pF})$
50	110	512	2.02 k	45.4 k	5.20	15.0	20.3
60	112	546	2.25 k	51.6 k	5.21	14.9	19.2
75	110	553	2.17 k	69.9 k	5.67	15.5	22.2
100	113	573	1.87 k	107 k	6.14	15.1	26.1
140	111	558	1.40 k	181 k	6.73	14.3	34.6
200	124	529	1.13 k	268 k	5.95	11.6	35.6

A significant trend in the above data is the increase in the largest capacitance with increase in borehole diameter. This is intuitively satisfying if the radar antenna is viewed as essentially being a system of capacitances, some of which are heavily environmentally dependent. The environmentally sensitive capacitance increases as the water-filled borehole widens, since more material of high permittivity is in the antenna's immediate vicinity.

**Table 4.2:** Elements values in Figure 4.7 for a water-filled borehole

Borehole diameter (mm)	$R_1(\Omega)$	$R_2(\Omega)$	$R_3(\Omega)$	$C_1(\text{pF})$	$C_2(\text{pF})$
50	135	668	45.3 k	7.90	31.9
60	136	706	51.5 k	7.70	31.0
75	133	735	69.8 k	8.53	34.0
100	132	750	107 k	9.33	37.1
140	127	724	182 k	10.6	44.1
200	137	711	268 k	10.4	42.3

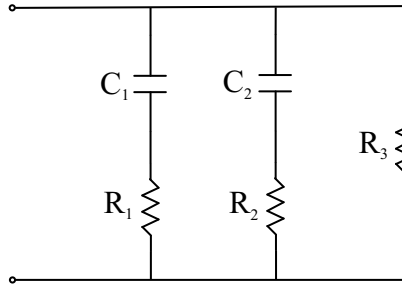


**Figure 4.7:** Network synthesized using a 2<sup>nd</sup> order impedance function

### 4.3.2 Equivalent circuits for air-filled boreholes

Circuits synthesized using 3<sup>rd</sup> order impedance functions for air-filled boreholes, realized lumped capacitances much smaller than 1 pF. Since capacitors with values of fractions of a picofarad are generally not available in the typical laboratory, no 3<sup>rd</sup> order networks for air-filled boreholes will be given.

The synthesized second order circuits however still give good approximations of antenna input impedance, and again appear as in Figure 4.7 with the corresponding component values given in table 4.3.

**Table 4.3:** Elements values in Figure 4.7 for an air-filled borehole

Borehole diameter (mm)	$R_1(\Omega)$	$R_2(\Omega)$	$R_3(\Omega)$	$C_1(\text{pF})$	$C_2(\text{pF})$
50	181	536	641 k	3.10	16.0
60	180	520	570 k	2.57	14.1
75	167	522	523 k	2.30	12.4
100	151	520	474 k	2.05	10.7
140	152	528	503 k	1.83	9.23
200	147	533	539 k	1.70	8.18

The values of  $R_3$  are again several orders larger than the other resistors and it may effectively be replaced by an open circuit.

In the element values of table 4.3, there is a clear trend in the decrease of capacitor values with the increase of borehole diameter. This is intuitively satisfying when again viewing the antenna as a system of environmentally sensitive capacitors. The capacitances decrease as the air-filled borehole widens, since there is less material of high electric permittivity in the antenna's immediate vicinity.

## 4.4 Evaluation of synthesized networks

Networks synthesized in the previous section using the Foster RC method for an air-filled and a water-filled borehole with 75 mm diameter will now be utilized to evaluate the accuracy of the equivalent loads. The network for the water-filled borehole, shown in Figure 4.6, has component values as indicated in table 4.1. The network for the air-filled borehole, shown in Figure 4.7, has component values as indicated in table 4.3.

The driving-port impedance of the two synthesized circuits are compared with the corresponding simulated antenna input impedances in Figures 4.8(a) to 4.8(d). The simulated feed-point currents from the ADS radar receiver circuit model discussed in Chapter 3 for the synthesized and simulated loads are shown in Figures 4.8(e) and 4.8(f). The simulated load was included in the circuit model as an equivalent load, using the ADS S-parameter block described in Chapter 3.

Neglecting resonance effects is clearly a better approximation in the case of a water-filled borehole, since the resonant peaks are narrower. Neglecting resonance furthermore has the consequence that the time-domain discharge current does not contain effects of current reflections from the antenna end-points as is seen in the discharge current of the simulated load. Figures 4.8(e) and 4.8(f) show that the discharge current from the synthesized and simulated loads correspond well with the exception of the absence of the effects of end-point current reflections in the current from the synthesized load.

Comparison of the discharge current from the synthesized load with measured current is possible in a limited sense with data from the on-board feed-point current probe described in Chapter 3. Probe measurements of the antenna discharge current were taken in a 200 mm water-filled borehole and in a 6 inch (152.4 mm) air- and water-filled borehole. As noted in Chapter 3, the probe suffers from strong EMI at the time of transmitter firing and useful data was only obtained in water-filled boreholes where the discharge current persists long after the EMI from the transmitter firing has subsided ( $\sim 40$  ns).

A network as in Figure 4.6, designed for a 140 mm diameter water-filled borehole using a  $3^{rd}$  order impedance function  $Z(s)$ , has component values as indicated in table 4.1. The discharge current of this load corresponds well to that measured with on-board probe in the slightly larger 6 inch water-filled borehole, as illustrated in Figure 4.9. The feed-point current was simulated without the inclusion of the T/R-switch in the circuit model to mimic the experimental current probe setup[28].

The synthesis of lumped element loads approximately equivalent to the borehole antenna input impedance is thus a success, with results being more accurate for water-filled boreholes, which is the main area of interest.

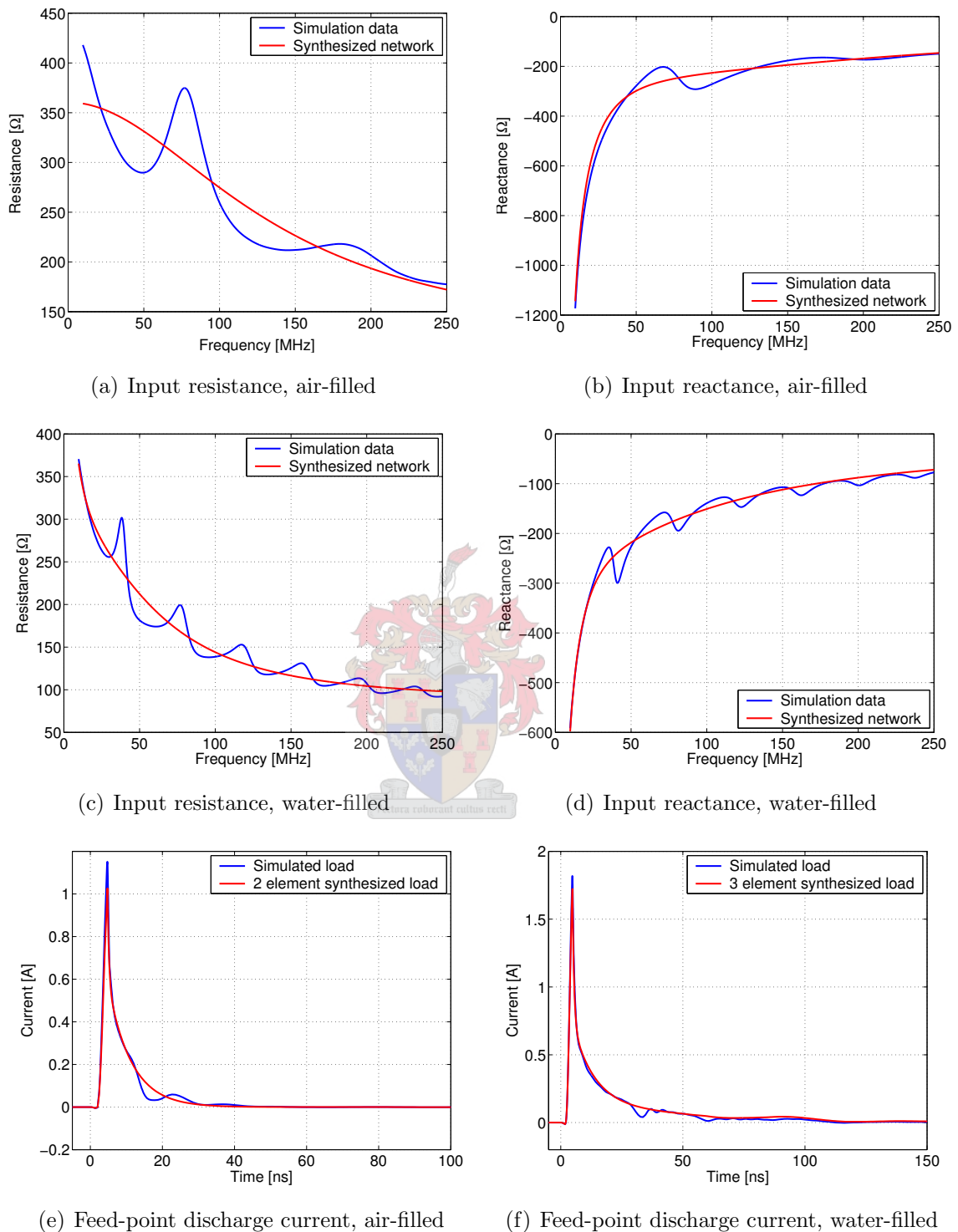


**Figure 4.8:** Comparison of input impedance and feed-point discharge current from the synthesized antenna load and the simulated load for an air- and water-filled 75 mm borehole

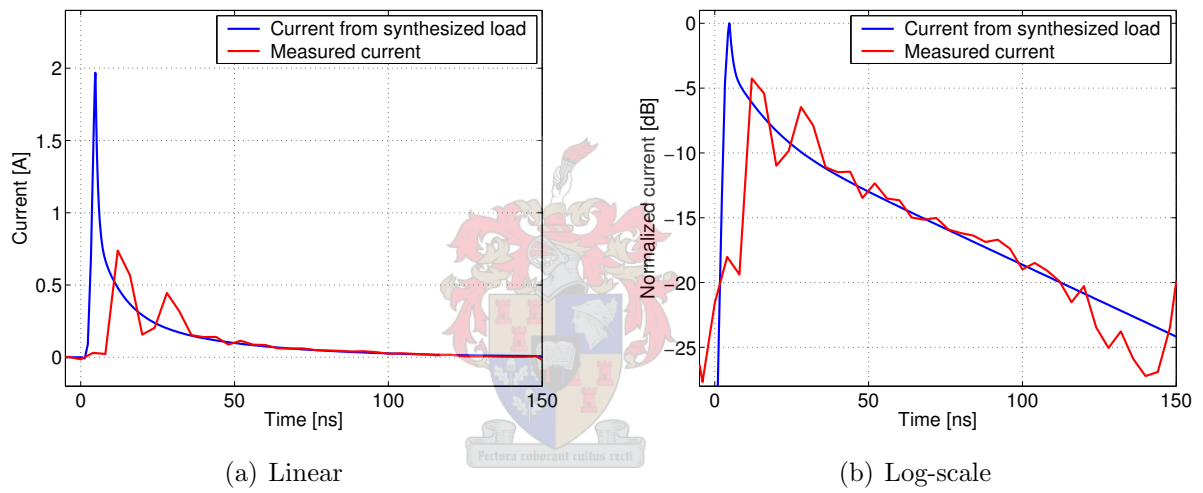


**Figure 4.9:** Comparison of current measured with an experimental current probe in 150 mm water-filled borehole with simulations using synthesized load

# Chapter 5

## Improved linear impedance loaded antennas for water-filled boreholes in hard rock

### 5.1 Introduction

Successful measures have been taken to reduce the prolonged saturation of the monostatic BHR receiver output in water-filled boreholes. The LNA and the STC amplifier stages were AC-coupled by placing a first-order diplexer between the two stages. The diplexer lets signals of 10 MHz and higher pass to the STC amplifier while dissipating signals below this band in a 200  $\Omega$  resistor. The STC amplifier timing was delayed so that the increase in gain from 11 to 46 dB does not occur until 144 ns later than on previous systems.

The current at the feed-point was furthermore filtered with the introduction of the modification to the receiver circuit as shown in Figure 5.1. The circuit effectively acts as a high-pass filter with a cut-off frequency at 10 MHz. A 47 pF capacitor is placed in series with the transformer, while a series RC section shunts the transformer. Figure 5.2(a) shows that slowly varying current passes through the shunt RC branch while higher frequency current signals pass through the transformer to the T/R-switch. Figure 5.2 shows the circuit's transfer function, or  $S_{21}$ , from the antenna terminals to the T/R-switch input.

Although solutions to the problem of prolonged saturation were hence already discovered, the underlying cause of the effect was not well understood. This chapter investigates the cause of the prolonged saturation and proposes an alternative solution through modifying the loading profile on the loaded arm of the BHR antenna.

Parametrical studies of Chapter 3 show that the resistive Wu-King loading profile implemented on the borehole radar antenna has a significant influence on its input impedance, causing it to remain capacitive over the entire frequency range of interest. The

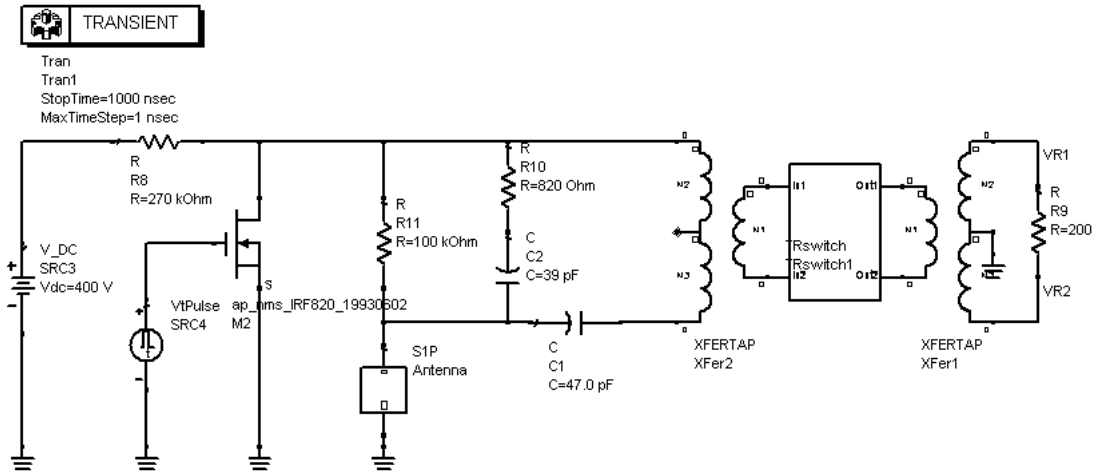
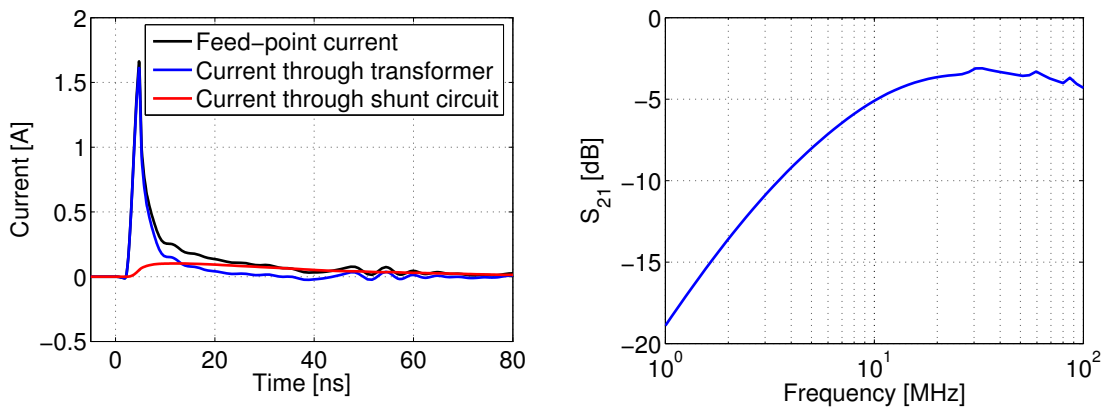


Figure 5.1: The simplified model of the antenna receiver circuit in ADS with the implemented high-pass filter at the feed-point



(a) Division of currents at the feed-point (b) Magnitude of the filter transfer function

Figure 5.2: Characteristics of the feed-point current filter

loading profile was hence suspected to be a major contributing cause to the poorly understood deterioration of feed-point current settling times in water-filled boreholes. In spite of this fact, no reference could be found specifying the original design parameters for the loading profile.

This chapter introduces the design procedure for a Wu-King loading profile, which reveals that the loading profile for the borehole antenna was designed for free space. It is subsequently shown that the use of profiles designed for free space in electrically dense media, such as water-filled boreholes, leads to a degraded feed-point current step response.

A resistive/capacitive profile is proposed as an improved impedance loading profile since it possesses reduced feed-point current settling times.

The non-trivial procedure for the design of a Wu-King profile for a wire in a cylindrically stratified medium is furthermore investigated, culminating in the creation of practical resistive/capacitive loading profiles for the borehole antenna. Results from simulations and field experiments are presented that confirm that the new antenna loading designs lead to significantly reduced feed-point current settling times in water-filled boreholes, thus substantially improving antenna performance in this environment.

## 5.2 The Wu-King non-reflecting impedance loading profile

The current distribution on short linear antennas exists essentially as a standing wave and the input impedance and radiation pattern are hence strong functions of frequency. A traveling-wave antenna however supports a solely outward traveling wave, leading to significant improvements in broadband and directional characteristics.

Wu and King have shown in their landmark 1965 paper [31] that a traveling wave linear antenna may be realized by impedance loading such that the impedance per unit length varies according to a specific function of length along the antenna. A short introduction to this impedance profile is now given, with emphasis on the antenna's feed-point characteristics. Whilst in the original paper the expressions were derived for an antenna in free space, they will be presented here generalized for an antenna in an ambient medium with relative permittivity  $\epsilon_r$ .

### 5.2.1 Profile definition

Wu and King [31, 32] showed that a dipole with half-length  $h$  and conductor radius  $a$  with an internal impedance per unit length given by

$$z^i(z) = \frac{\zeta_0 \Psi(\sqrt{\epsilon_r} k_0)}{2\pi \sqrt{\epsilon_r}} \frac{1}{h - |z|} \quad (5.1)$$

supports the current distribution

$$I(z) = \frac{2\pi\sqrt{\epsilon_r}V_0}{\zeta_0\Psi(1 - j/\sqrt{\epsilon_r}k_0h)} \left(1 - \frac{|z|}{h}\right) e^{-j\sqrt{\epsilon_r}k_0h} \quad (5.2)$$

when excited by a time-harmonic driving-port voltage  $V_0$ . Equation 5.2 represents an outward traveling wave of current with amplitude that decreases linearly to zero at the ends and no reflected wave in the opposite direction.  $\zeta_0 = \sqrt{\mu_0/\epsilon_0}$  is the impedance of free space,  $f_{des}$  the design frequency and  $k_0 = 2\pi f_{des}/c$  is the associated free space wavenumber. The function  $\Psi(k)$  is termed the complex expansion parameter and will be investigated in detail in section 5.2.2. A dipole with an impedance distribution given by 5.1 will be termed a *Wu-King dipole*.

The Wu-King dipole's radiation pattern features a virtual absence of minor sidelobes, even for electrically long antennas [31]. Its directional properties are hence a significant improvement over that of an unloaded dipole. A substantial loss in radiation efficiency due to the introduction of the lossy loading profile is however the trade-off for the improved directional properties, with an efficiency as low as 10% at  $h/\lambda = 0.25$  [32].

The input impedance at the design frequency

$$Z_{in} = \frac{\zeta_0\Psi}{2\pi\sqrt{\epsilon_r}} \left(1 - \frac{j}{\sqrt{\epsilon_r}k_0h}\right) \quad (5.3)$$

is represented by Wu and King [31] in the simple form of a resistor in series with a capacitor:

$$Z_{in} = R_{in} - j/\omega C_{in} \quad (5.4)$$

where

$$R_{in} = \frac{\zeta_0\Psi}{2\pi\sqrt{\epsilon_r}} \quad (5.5)$$

and<sup>1</sup>

$$C_{in} = \frac{2\pi}{\Psi}\epsilon_0\epsilon_r h \quad (5.6)$$

This representation assumes that the expansion parameter  $\Psi$  is real, while it will be shown in the following section that this is only approximately true at lower design frequencies. The analogy of the input impedance to a series RC circuit will however be seen to be valid over a wide frequency band, providing a useful model of the input impedance of the Wu-King dipole.

---

<sup>1</sup>The expression for  $C_0$  for the dipole in free space in Wu and King [31] is given incorrectly as  $C_0 = \epsilon_0 h$ .

### 5.2.2 The complex expansion parameter $\Psi$

The complex expansion parameter is formally defined as the ratio of the axial vector potential  $A_z(z)$  on the surface of the antenna to the axial current  $I(z)$  at  $z = 0$  [31]. Under the assumptions  $a \ll h$  and  $ka \ll 1$ , the expression for the expansion parameter is given approximately by

$$\Psi(k) \approx 2 \left[ \sinh^{-1} \left( \frac{h}{a} \right) - C(2ka, 2kh) - jS(2ka, 2kh) \right] + \frac{j}{kh} (1 - e^{-2jkh}) \quad (5.7)$$

where  $C(2ka, 2kh)$  and  $S(2ka, 2kh)$  are the generalized cosine and sine integrals defined in [31]. The factor  $\Psi$  is the only complex constant and frequency dependent parameter appearing in expression 5.1 for the Wu-King impedance profile. The profile is hence a complex impedance with the ratio of real to imaginary part identical to that of  $\Psi$ . The imaginary part of  $\Psi$  is found to be negative for all frequencies and the reactive component of the impedance profile must consequently be implemented as a distributed capacitance. The real and imaginary parts of  $\Psi$  are illustrated in Figure 5.3 for  $h = 0.6$  m and  $a = 1.5$  mm, the dimensions of the loaded arm of the borehole antenna.

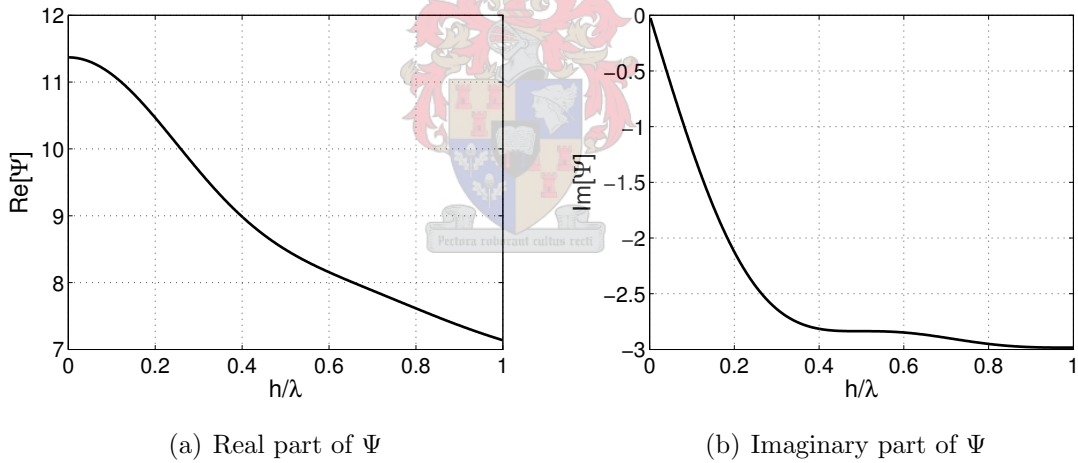


**Figure 5.3:** Real and imaginary parts of  $\Psi$  for  $h = 0.6$  m and  $a = 1.5$  mm

The real part of  $\Psi$  decreases slowly with frequency. The required distributed resistive loading of the impedance profile consequently also varies slowly with frequency – a property that leads to good wide-band performance. At shorter wavelengths the imaginary part remains relatively constant, while when  $h/\lambda < 0.25$  it drops linearly to zero. When designing a profile for low frequencies, where imaginary part is small compared to real part, the profile may hence be approximated as a distributed resistance. When the capacitive profile is neglected the current deviates from the distribution with linearly decreasing amplitude and phase as given in equation 5.2. In a numerical and experimental study by Kanda [13], it was found that when using a pure resistive profile, the measured current

distribution corresponds well with the desired theoretical current distribution of equation 5.2 when  $h/\lambda < 0.25$ . When  $h/\lambda < 0.25$  the loading profile may hence be successfully approximated as resistive, but for higher design frequencies the distributed capacitance needs to be taken into account for the current distribution to remain as in 5.2.

### 5.2.3 Wu-King profiles for wide-band applications

The Wu-King profile is often used to create antennas with good pulse reception and radiation properties [13, 14] due to its good wide-band characteristics.

When designing the Wu-King impedance loading for a wide-band antenna, the reactive component of the profile is generally neglected since the capacitive implementation thereof is heavily frequency dependent. The distributed series capacitive loading, implemented as

$$C^i(z) = \frac{1}{2\pi f_{des} \text{Im}[z^i(z)]} \quad (5.8)$$

leads to a much higher reactive loading than required by the Wu-King profile at frequencies below  $f_{des}$ , while the converse is true at frequencies higher than  $f_{des}$ . A parametrical study by Keller [15] showed that including a distributed capacitance results in worse wide-band performance than when it is neglected, especially if the level of capacitive loading is small.

The level of required resistive loading for the Wu-King profile was shown in the previous section to decrease slowly with frequency. Resistive loading implemented for a design frequency  $f_{des}$  will hence be valid over a wide frequency band, causing sufficient dissipation to give a non-reflective current distribution at all frequencies higher than  $f_{des}$ .

The choice of design frequency is not critical when designing a loading profile for a wide-band antenna. The method most used in practice and by several authors [20], [19] is to design the profile by taking the parameter  $\Psi(k)$  as its zero frequency value:

$$\Psi_0 = 2 \left[ \ln \left( \frac{2h}{a} \right) - 1 \right] \quad (5.9)$$

which is a real constant. Several authors took the value of  $\Psi$  as its real part at a resonant frequency of the antenna, notably the half-wave resonance frequency [13], [14], [19]. Since the required level of resistive loading drops with increasing frequency, the safest option is however to choose  $\Psi$  as its real value at the lowest frequency of interest, to ensure that the current distribution is non-reflective over the entire bandwidth.

### 5.2.4 Feed-point characteristics

The real part of the expansion parameter  $\Psi$  is seen in section 5.2.2 to be dominant when  $h/\lambda < 0.25$ . Wu and King's representation of the Wu-King dipole's input impedance as

a series RC circuit, discussed in section 5.2.1, is hence approximately valid if the design frequency falls in that range. However, due to the slow variation of the real part of  $\Psi$  with frequency, this simple model of the input impedance is approximately valid over a wide range of frequencies.

To illustrate the validity of the model, the resistance  $R_{in}$  and capacitance  $C_{in}$  was calculated for a Wu-King dipole in free space with  $h = 0.6$  m and  $a = 1.5$  mm, according to equations 5.5 and 5.6 at  $f_{des} = 100$  MHz.  $\Psi$  was taken as its real value at 100 MHz ( $\lambda_{des} = 3$  m), resulting in values of  $R_{in} = 627 \Omega$  and  $C_{in} = 3.19$  pF. The input impedance of the model  $Z_{in} = R_{in} - j/\omega C_{in}$  is shown in Figure 5.4 in comparison with the input impedance obtained from a FEKO MoM simulation of the corresponding Wu-King dipole<sup>2</sup> designed for free space at 100 MHz.

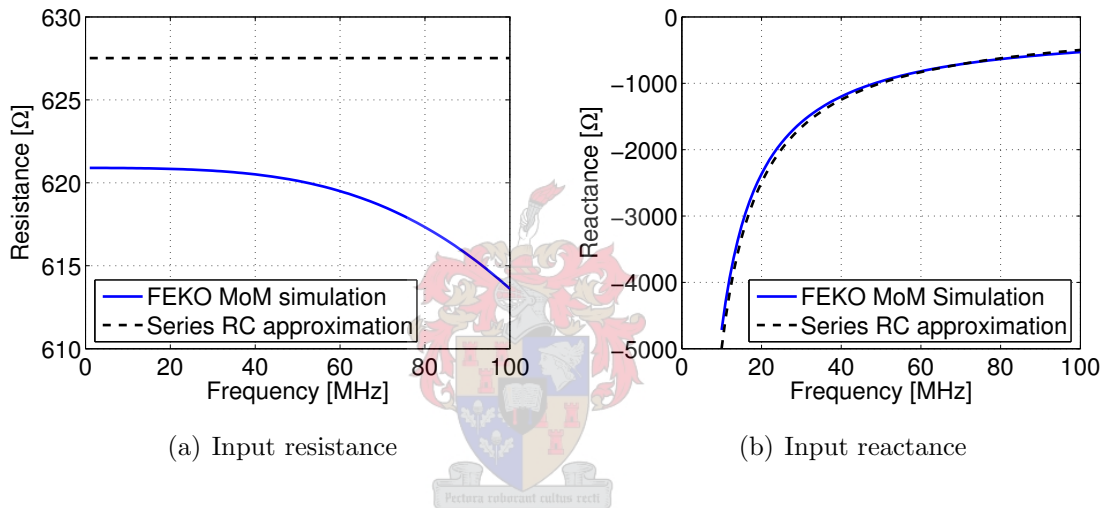


**Figure 5.4:** Comparison of RC approximation to input impedance with that of the MoM FEKO model for Wu-King dipole with  $h = 0.6$  m and  $a = 1.5$  mm in free space

The simple RC input impedance model and the MoM results clearly correspond well. The response of the feed-point current of loaded antennas to a step voltage is of some importance in this investigation, since the BHR antenna is essentially excited with step input voltage as the radar transmitter fires. The usefulness of the model also extends into the time domain. The time-domain current response of a series connected resistor and capacitor to a step voltage is well known and in terms of the Wu-King input impedance model is found as:

$$I = \frac{1}{R_{in}} e^{-t/\tau} = \frac{2\pi\sqrt{\epsilon_r}}{\zeta_0\Psi} e^{-t/\tau} \quad (5.10)$$

with

$$\tau = R_{in}C_{in} = \frac{\sqrt{\epsilon_r}h}{c} \quad (5.11)$$

<sup>2</sup>Distributed impedance in the MoM model implemented as discrete resistive loading with 12 elements

Note that the expression 5.11 for  $\tau$  is the time for a pulse to propagate a distance of  $h$  meters at the velocity of propagation in the ambient medium,  $c/\sqrt{\epsilon_r}$ .

The response of the Wu-King dipole's feed-point current to a step voltage is hence approximately given by a familiar exponential discharge curve with the time constant determined by the permittivity of the ambient medium and the length of the antenna. The conclusions from this simple model will be validated in numerical calculations of the step response in a following section.

It must be noted that the series R/C model is not however not intended as an accurate theoretical description of the wide-band feed-point characteristics of a Wu-King dipole. The predicted input impedance and current step response from equations 5.4 and 5.10 often diverge considerably from numerically calculated values, mainly due to the approximate nature of the expression for the expansion parameter  $\Psi$ . The usefulness of the model however lies therein that it allows predictions of how the feed-point characteristics of the Wu-King dipole varies with changes in environment or antenna length.

### 5.2.5 Level of loading on the borehole antenna

The original design parameters for the resistive Wu-King profile currently used on the borehole antenna remain unknown. Utilizing expression 5.1 for the loading profile, using the zero frequency value  $\Psi_0$  of the expansion parameter, it was however calculated that the profile corresponds to one designed for free space, with the level of resistive loading scaled furthermore by 150%. The profile is hence not designed for the electrically dense borehole environments in which the antenna is deployed.

The level of resistive loading on the antenna is much higher than required for the intended application of the antenna, with definite implications for the antenna's radiation efficiency and feed-point characteristics. This will be the subject of investigation in following sections.

## 5.3 Feed-point characteristics of Wu-King dipoles in electrically dense media

This section briefly investigates the feed-point characteristics of Wu-King dipoles designed for electrically dense media. The loading profile on the borehole antenna was found in the previous section to be designed for free space. The characteristics of a Wu-King dipole designed for free space but used in ambient media of relative permittivity  $\epsilon_r$  is hence also investigated. It is found that the resistive Wu-King dipole is not well suited for use as a wide-band antenna in electrically dense ambient media of varying permittivity.

### 5.3.1 Wu-King dipoles designed for electrically dense media

The series RC circuit model of the Wu-King dipole's input impedance, introduced in section 5.2.4, provides some insight into its feed-point characteristics. Equations 5.5 and 5.6 from the RC model give the input impedance of a Wu-King dipole designed for an ambient medium with relative permittivity  $\epsilon_r$  in relation to that of Wu-King dipole designed for free space. The frequency is scaled with  $\sqrt{\epsilon_r}$  and the input resistance with  $1/\sqrt{\epsilon_r}$ , while the input capacitance scales with  $\epsilon_r$ . This corresponds to a general theorem for antennas in homogeneous media that states that *the impedance normalized to that of the medium takes the same value at frequency  $\omega$  in a medium of index  $n$  as it does at frequency  $n\omega$  in a medium of index 1*, where the index  $n = (\mu\epsilon/\mu_0\epsilon_0)^{1/2}$  [7]. If, as in this case, only the permittivity is changed from  $\epsilon_0$  to  $\epsilon_r\epsilon_0$ , the relation may be expressed as:

$$Z(\omega, \epsilon_r\epsilon_0) = \frac{1}{\sqrt{\epsilon_r}} Z(\sqrt{\epsilon_r}\omega, \epsilon_0) \quad (5.12)$$

The input impedance from FEKO MoM simulations of three Wu-King dipoles of dimension  $h = 0.6$  m and  $a = 1.5$  mm respectively designed<sup>3</sup> for and simulated in ambient media of relative permittivity  $\epsilon_r = 1, 4$  and  $9$  are illustrated in Figure 5.5. The scaling of the input impedance is as predicted.

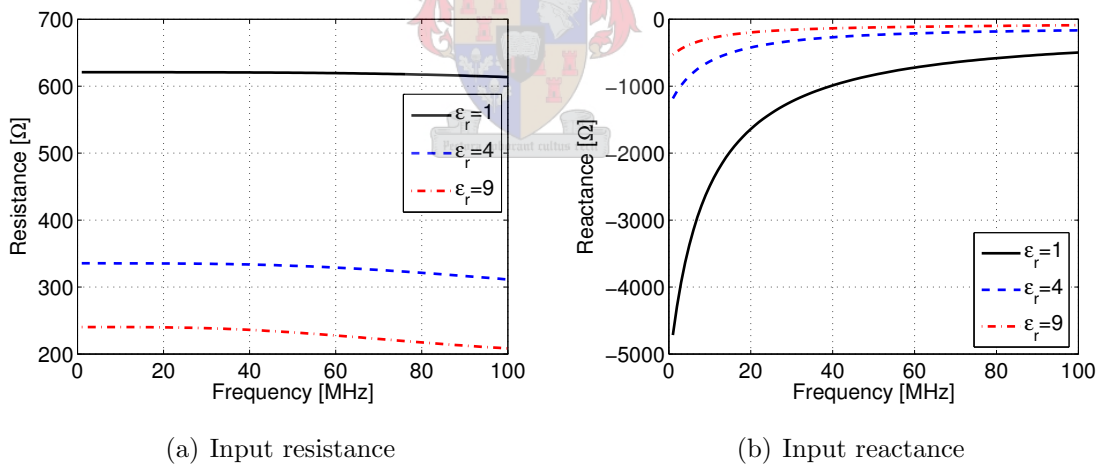


**Figure 5.5:** *Input impedance of Wu-King dipoles in different media from FEKO MoM calculations*

Equations 5.10 and 5.11 from the RC model furthermore predict an exponential discharge curve for the response of the feed-point current to a step input voltage with a current amplitude and time constant that scales with  $\sqrt{\epsilon_r}$ . The current step response

<sup>3</sup>Antenna designed for a wavelength of  $\lambda_{des} = 3$  m with the distributed loading profile implemented in the MoM model as discrete resistive loading in 12 steps.

may be computed numerically from simulated input impedance data as in Chapter 2 by viewing the input admittance,  $Y(\omega) = \frac{1}{Z(\omega)}$ , of the antenna as a linear system:

$$Y_{in}(\omega) = \frac{I_{in}(\omega)}{V_{in}(\omega)} \quad (5.13)$$

The time-domain current response may then be computed through application of the *Inverse Fourier Transform*:

$$i_{in}(t) = F^{-1} [Y_{in}(\omega)V_{in}(\omega)] \quad (5.14)$$

The above computation was carried out using Advanced Design System from Agilent EEsof (as introduced in Chapter 3), since it has the ability to produce better quality time-domain data through interpolation and extrapolation of the supplied discrete, band-limited numerical input admittance data. The numerical time-domain current step response computed from the FEKO input impedance data of the Wu-King dipoles for the respective media is shown in Figure 5.6.

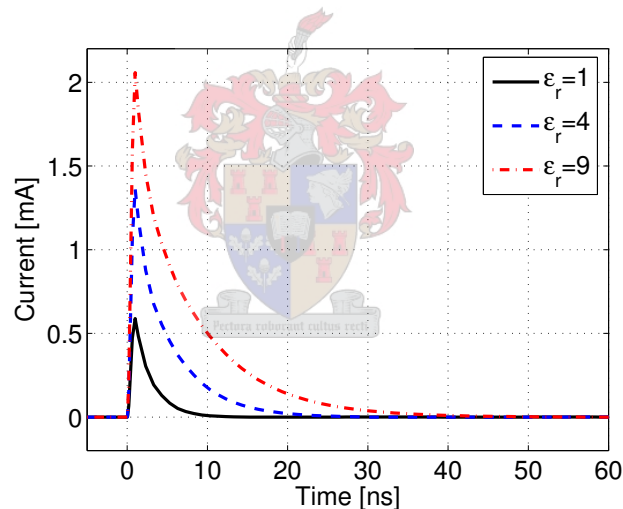


**Figure 5.6:** Feed-point current step response of resistive Wu-King dipoles in different ambient media computed numerically from simulated input admittance data

The current step response amplitudes scale with  $\epsilon_r$  as predicted. The settling times<sup>4</sup> of the dipoles for  $\epsilon_r = 1, 4,$  and  $9$  are  $t_s = 10.7$  ns,  $21.6$  ns and  $33.5$  ns respectively. The settling times predicted by equation 5.11 of the RC model<sup>5</sup>, namely  $9.2$  ns,  $18.4$  ns, and  $27.6$  ns, do not correspond to the simulated values very accurately, however the predicted scaling with  $\sqrt{\epsilon_r}$  in the simulated data is again apparent.

<sup>4</sup>Settling time is defined as the time at which the amplitude of the step response falls to 1% of its peak value

<sup>5</sup>Through the relation  $t_s = 4.6\tau$

These factors should be taken into account when replacing the Wu-King antenna on a borehole radar system with one designed for electrically dense media and operating the system in such a medium. The resulting changes in antenna feed-point matching, step response amplitude and settling times may have a negative influence on the system's performance.

### 5.3.2 The free space Wu-King dipole in electrically dense media

This section investigates the feed-point characteristics of a Wu-King dipole designed for free space, but used in an electrically dense ambient medium. The resulting feed-point current step response of such an antenna is shown to be substantially degraded compared to that of a Wu-King dipole designed for the dense medium.

A Wu-King dipole designed for free space, which will be termed a *free space Wu-King dipole*, has the following impedance loading profile

$$z^i(z) = \frac{\zeta_0 \Psi(k_0)}{2\pi} \frac{1}{h - |z|} \quad (5.15)$$

The free space Wu-King dipole is now however placed in an ambient medium with relative permittivity  $\epsilon_r$  to mimic the deployment of the borehole antenna in an electrically dense borehole environment. Of interest is how the simple RC model of the input impedance of the free space Wu-King dipole changes in this circumstance.

The correct Wu-King impedance loading to create the non-reflecting current distribution of equation 5.2 on a dipole in an ambient medium of relative permittivity  $\epsilon_r$ , is that of 5.1. The loading implemented on the free space Wu-King dipole and that required by equation 5.2 are however not dissimilar. A comparison shows that actual loading on the dipole, equation 5.15, is simply the required Wu-King profile for the electrically dense ambient medium, equation 5.1, scaled by a factor  $\alpha$ , where

$$\alpha = \frac{\Psi(k_0)}{\Psi(\sqrt{\epsilon_r} k_0)} \sqrt{\epsilon_r} \quad (5.16)$$

The free space Wu-King dipole in the electrically dense ambient medium is hence equivalent to a Wu-King dipole designed for the dense medium, but with the level of impedance loading scaled by the factor  $\alpha$ :

$$z^i(z) = \frac{\zeta_0 \Psi(\sqrt{\epsilon_r} k_0)}{2\pi \sqrt{\epsilon_r}} \frac{\alpha}{h - |z|} \quad (5.17)$$

Scaled Wu-King profiles of the form 5.17 have been investigated by several authors [15], mainly with  $\alpha < 1$  in an attempt to obtain a more efficient impedance profile. Most significantly, Shen and Wu [23] investigated the current distribution on a dipole with Wu-King impedance loading scaled by a factor  $\alpha$ . This antenna will be termed a *scaled*

*Wu-King dipole* for convenience. The input impedance of the scaled Wu-King dipole is derived in Appendix G, utilizing Shen and Wu's results. The result in Appendix G is derived for a dipole in free space, but is easily adapted for an ambient medium with relative permittivity  $\epsilon_r$ :

$$Z_{in}^\alpha = \frac{\zeta_0 \Psi(\sqrt{\epsilon_r} k_0)}{2\pi \sqrt{\epsilon_r}} \left[ 1 + \frac{1}{j\sqrt{\epsilon_r} k_0 h} - 2 \frac{\Phi'(-2j\sqrt{\epsilon_r} k_0 h)}{\Phi(-2j\sqrt{\epsilon_r} k_0 h)} \right] \quad (5.18)$$

$$= Z_{in} \left[ 1 - \frac{2j\sqrt{\epsilon_r} k_0 h}{1 + j\sqrt{\epsilon_r} k_0 h} \frac{\Phi'(-2j\sqrt{\epsilon_r} k_0 h)}{\Phi(-2j\sqrt{\epsilon_r} k_0 h)} \right] \quad (5.19)$$

where  $\Phi(x)$  is related to the confluent hypergeometric function, defined in Appendix G, by  $\Phi(x) = F_1(1 - \alpha, 2, x)$  and  $\Phi'(x)$  is its derivative with respect to  $x$ .  $Z_{in}$  is the input impedance of the unscaled Wu-King dipole ( $\alpha = 1$ ) as defined in equation 5.3.

Like the expression 5.3 for  $Z_{in}$ , the equation for  $Z_{in}^\alpha$  gives the input impedance only at the design frequency, but may be utilized to obtain wide-band approximations to the input impedance through the use of the series RC circuit model of the input impedance,  $Z_{in} = R_{in} + 1/(j\omega C_{in})$ , introduced in section 5.2.4. The factor  $Z_{in}$  is approximated over a wide band using the RC model and then simply scaled by the second factor in equation 5.19 at each frequency point to arrive at the approximation to the input impedance of the scaled Wu-King dipole.

The free space Wu-King dipole from section 5.2.4, dimensions  $h = 0.6$  m and  $a = 1.5$  mm for  $f_{des} = 100$  MHz, will be utilized to evaluate the approximation to the input impedance through placing it in ambient media with  $\epsilon_r = 4$  and  $\epsilon_r = 9$ . The value of  $\Psi$  in the equations 5.5 and 5.6 for  $R_{in}$  and  $C_{in}$  will again be taken as its real value at the antenna's design wavelength of  $\lambda_{des} = 3$  m. This yields values of  $R_{in} = 314 \Omega$  and  $C_{in} = 12.8$  pF for a Wu-King dipole designed for an ambient medium with  $\epsilon_r = 4$  and  $R_{in} = 209 \Omega$  and  $C_{in} = 28.7$  pF for  $\epsilon_r = 9$ .

The input impedance  $Z_{in}$  resulting from the above models are utilized in equation 5.19 to arrive at the wide-band approximations of the free space Wu-King dipole's input impedance in ambient media with  $\epsilon_r = 4$  and  $\epsilon_r = 9$ . When the scaling factor  $\alpha$  is a positive integer,  $Z_{in}^\alpha$  may be expressed in closed form. To simplify calculations it was hence assumed that  $\alpha \approx \sqrt{\epsilon_r}$  so that  $\alpha = 2$  and  $\alpha = 3$  results for  $\epsilon_r = 4$  and  $\epsilon_r = 9$  respectively. The formulas for the input impedance of a Wu-King dipole with a profile scaled by these factors are presented in Appendix G.

The approximations to the input impedance of the free space Wu-King dipole in free space,  $\epsilon_r = 4$  and  $\epsilon_r = 9$  are shown in Figure 5.7 in comparison with FEKO MoM simulated input impedance data for the antenna in the respective environments.

The approximate and simulated input impedance are in good agreement. The predicted input resistance values are within 10% of the simulated values, while the input reactance values correspond to greater accuracy. Modelling the free space Wu-King dipole

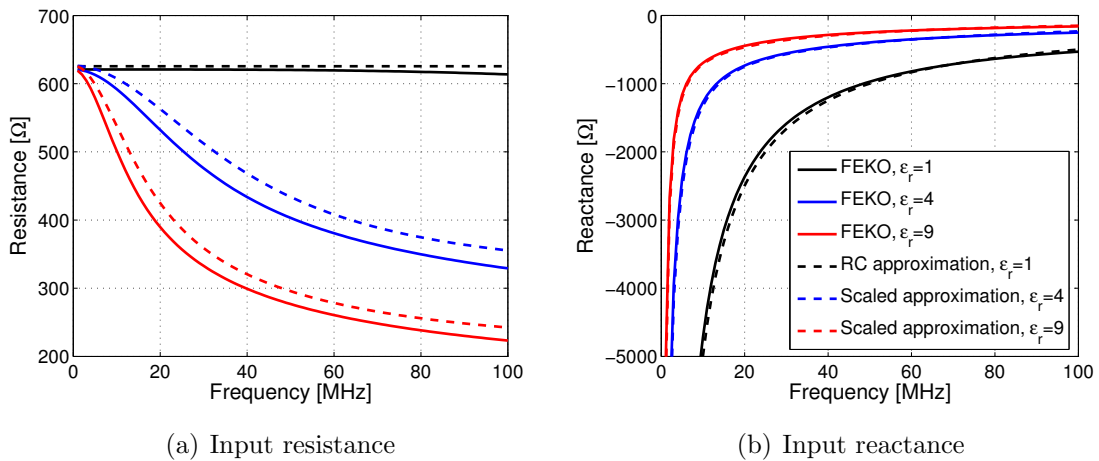


**Figure 5.7:** Comparison of approximations to input impedance of the free space Wu-King dipole of dimensions  $h = 0.6$  m and  $a = 1.5$  mm in free space and dense media with corresponding results from the FEKO MoM model

in an environment with relative permittivity  $\epsilon_r$  as a scaled Wu-King profile in that environment hence predicts the changes in input impedance with good accuracy.

The input impedance of the free space Wu-King dipole in  $\epsilon_r = 4$  and 9 is compared with that of Wu-King dipoles designed for the respective media in Figure 5.8 and the deviation from the RC model of input impedance is apparent. Due to its heavily frequency dependent input resistance and larger input reactance, the free space Wu-King dipole will not be matched as well as the correctly designed dipole and will generally have worse wide-band performance.

The feed-point current step response is expected to deviate from the exponential discharge curve seen in the previous section. The numerical time-domain current step response may be computed from the FEKO input impedance data of the free space Wu-King dipole in the respective media and is shown in Figure 5.9 in comparison with that of the correctly designed Wu-King dipoles of the previous section for  $\epsilon_r = 4$  and 9.

The current amplitudes again scale approximately with  $\sqrt{\epsilon_r}$  as in the previous section, however the settling times are longer. Quantitatively, the settling times are 29.5 ns and 56.5 ns for  $\epsilon_r = 4$  and 9 which respectively represent an increase of 37.5% and 68.7% over that of the correctly designed Wu-King dipoles.

This deterioration of the feed-point current step response is the direct cause of the use of a Wu-King dipole with a level of impedance loading higher than that required by the Wu-King distribution. The feed-point current step response of the borehole antenna will be susceptible to the same deterioration due to the dominant effect of the high level of resistive Wu-King loading implemented on the antenna input impedance. With the initial quick discharge and the slow current recovery thereafter seen in Figure 5.9, the

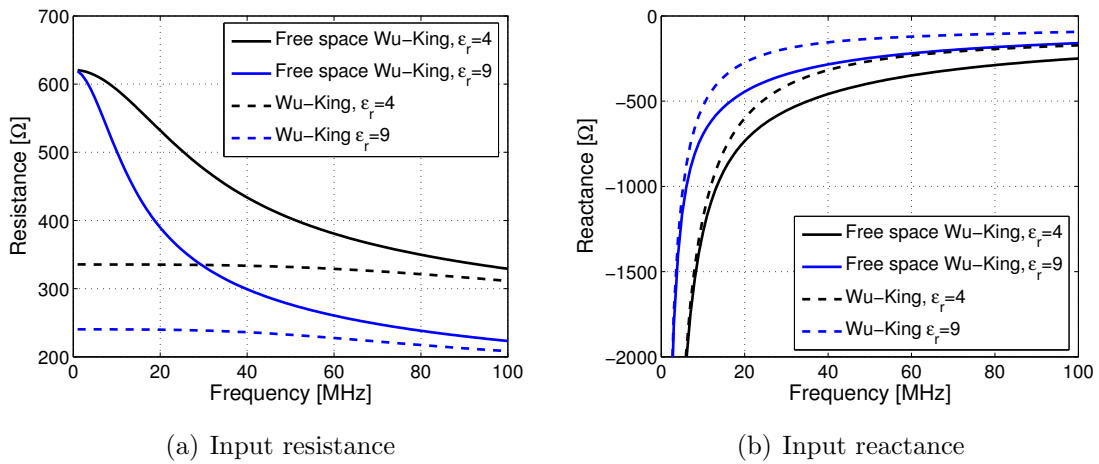


**Figure 5.8:** Comparison of the free space Wu-King dipole input impedance in  $\epsilon_r = 4$  and  $\epsilon_r = 9$  with that of correctly designed Wu-King dipoles for the corresponding media from FEKO MoM calculations

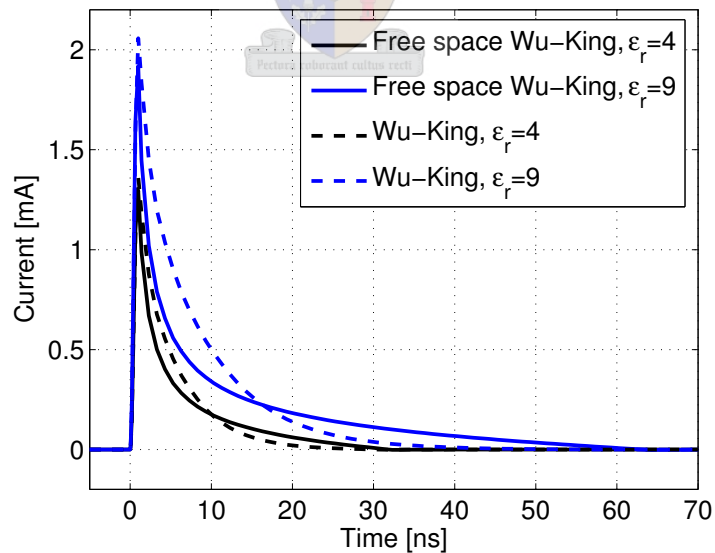


**Figure 5.9:** The feed-point current step response of a free space Wu-King dipole in  $\epsilon_r = 4$  and  $\epsilon_r = 9$  in comparison with Wu-King dipoles designed for the respective media computed numerically with ADS from input impedance data

step response of the free space Wu-King dipole in dense media clearly resembles the discharge current of the BHR antenna in water-filled boreholes, as shown in Figure 3.7.

### 5.3.3 Inadequacy of the resistive Wu-King profile

Monostatic borehole radar systems are required to operate in media of greatly varying electric permittivity. The most dramatic variation in electric properties of the surrounding medium commonly presents itself when a deployed radar system moves from an air-filled to a water-filled section of a borehole.

The magnitude of the impedance loading specified by the Wu-King profile in equation 5.1 is however environmentally dependent. The level of loading required for a profile designed for an electrically dense medium such as a water-filled borehole would be lower than that required for an air-filled borehole and the current distribution on the Wu-King antenna would hence not be non-reflective in the latter. Conversely, the level of loading for a profile designed for an air-filled borehole would be higher than that required for a water-filled borehole. In this case the antenna would display the degraded feed-point characteristics illustrated in the previous section.

Designing Wu-King profiles for deployment in specific environment is however not a solution due to the settling time of the feed-point current step response becoming very large with the scaling by the factor  $\sqrt{\epsilon_r}$  in electrically dense media. These long settling times place a limit on the performance of monostatic radar systems in environments such as wide water-filled boreholes.

The Wu-King dipole in its traditional resistive implementation as investigated thus far is hence not well suited for use as a wide-band antenna in electrically dense media or media with varying electromagnetic properties. An alternative implementation of the loading profile with shorter and less environmentally sensitive current step response settling times is proposed in the following section.

## 5.4 The resistive/capacitive Wu-King dipole as a loading profile for electrically dense media

The reactive component of the Wu-King distributed impedance profile is implemented as the distributed series capacitance given in equation 5.8. As mentioned in section 5.2.3, the distributed reactance is however neglected in the design of an antenna for wide-band applications, due to the frequency dependence of the capacitive implementation thereof. At frequencies well below that for which the capacitive profile 5.8 is implemented, the profile has an extremely high level of reactive loading that departs radically from that required by the Wu-King profile, with the resistive component becoming negligible.

The insertion of a distributed series capacitance along the antenna was expected to lower the *equivalent capacitance* of the antenna (or equivalently increase the input reactance), thereby reducing the time constant exponential recovery of the feed-point current step response.

Simulations by Keller [15] showed that the effect of high reactive loading is not only to increase the magnitude of the input reactance at lower frequencies, but also to decrease the input resistance. Keller furthermore illustrated that this effect wanes with higher levels of capacitive loading, hence smaller reactive loading.

It was hypothesized that the effect of inclusion of capacitive loading described above may be utilized to improve the feed-point characteristics of a free space Wu-King dipole that is operated in dense media, as described in section 5.3.2. The decrease in input resistance caused by the reactive loading at low frequencies counteracts the increase observed when placing the free space Wu-King dipole in an electrically dense medium.

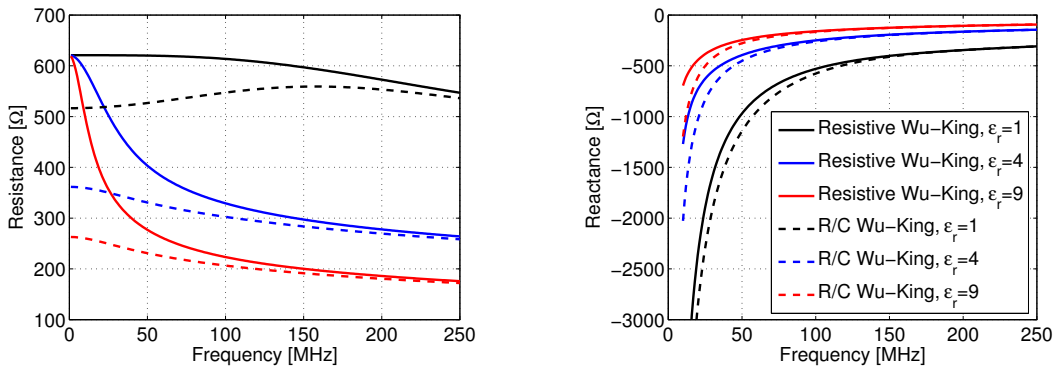
The effect of inclusion of a capacitive loading profile on a free space Wu-King dipole in dense media is investigated through use of FEKO MoM simulations. The free space Wu-King dipole with  $h = 0.6$  m and  $a = 1.5$  mm from section 5.3.2 with resistive loading resulting from taking  $\Psi$  as its real value at  $\lambda_{des} = 3$  m is again utilized. The reactive component of the profile at  $\lambda_{des} = 3$  m is now however also included on the dipole as a series capacitive loading<sup>6</sup>. A second loading profile, identical to the first but with the capacitive loading scaled by  $\frac{1}{3}$  is also investigated to observe the effects of a larger reactive loading. The FEKO input impedance results and numerically calculated feed-point current step response curves for the two antennas are shown in Figure 5.10 for ambient media with  $\epsilon_r = 1, 4$  and  $9$ . The input impedance of the antenna with pure resistive loading is also included for comparison.

The input resistance of the resistive/capacitive antennas decreases at lower frequencies as expected, with the effect being more pronounced in the electrically dense media. Input reactance is also larger at low frequencies than compared that of the free space Wu-King dipole. These effects are larger in the antenna with high reactive loading. Settling times for the antenna with low reactive loading in  $\epsilon_r = 1, 4$  and  $9$  are 7.2 ns, 13.7 ns and 18.5 ns respectively. The respective settling times for the antenna with high reactive loading is 4.98 ns, 7.02 ns and 9.95 ns. These settling times represent dramatic improvements over that of the free space Wu-King dipole investigated in section 5.3.2, namely 10.7 ns, 21.6 ns and 33.5 ns.

Due to the high reactive loading, a decrease in the antenna gain is intuitively expected at low frequencies and a comparison of the gain patterns of the antennas was performed

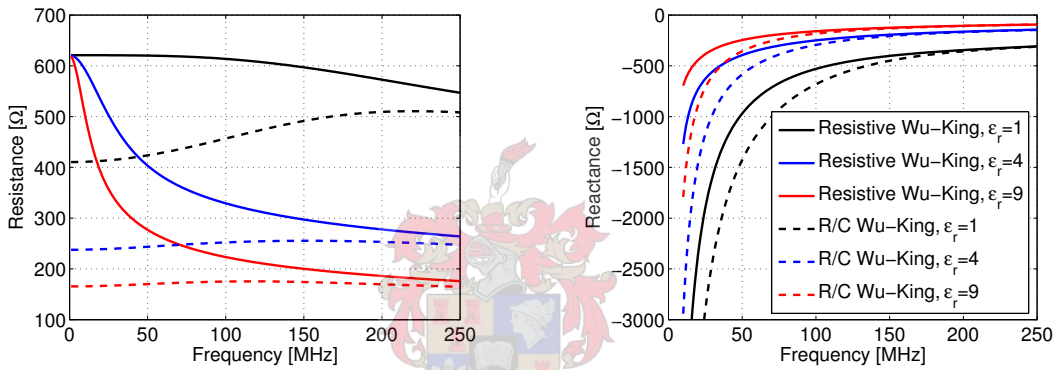
---

<sup>6</sup>Distributed series resistive and capacitive loading in the MoM model implemented as discrete loading with 12 elements.



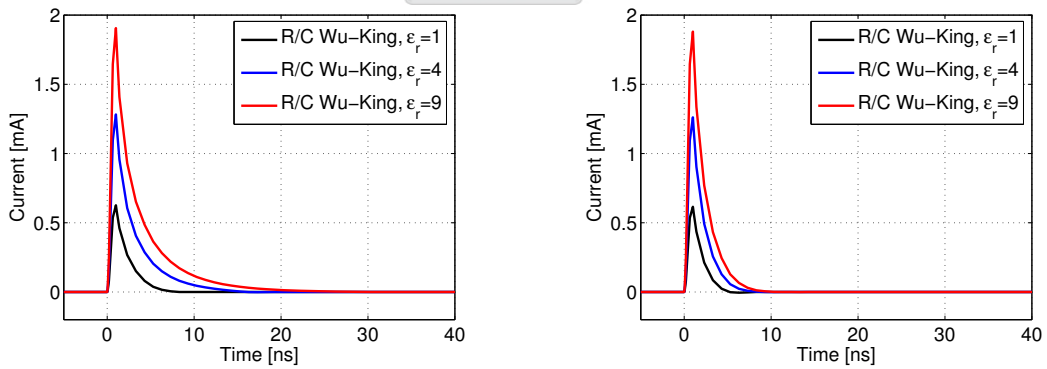
(a) Input resistance, low reactive loading

(b) Input reactance, low reactive loading



(c) Input resistance, high reactive loading

(d) Input reactance, high reactive loading



(e) Feed-point current step response, low reactive loading

(f) Feed-point current step response, high reactive loading

**Figure 5.10:** Comparison of feed-point characteristics of resistive/capacitive free space Wu-King dipoles to a resistive free space Wu-King dipole in media with  $\epsilon_r = 1, 4$  and  $9$ , from FEKO MoM and ADS simulations

over a range of frequencies. The difference in gain for all antennas in an ambient medium with  $\epsilon_r = 1$  was insignificant. Surprisingly the difference in gain patterns between the resistive dipole and the Wu-King dipole with low reactive loading were practically identical. The gain of the antenna with high reactive loading was however slightly lower at low frequencies. At a frequency of 20 MHz the second antenna had a broadside gain 0.84 dB lower in  $\epsilon_r = 4$  and 1.24 dB lower in  $\epsilon_r = 9$ .

The resistive/capacitive antennas hence improve the current step response in dense media dramatically while realizing an input impedance that is more wide-band in nature, without detracting significantly from the radiation efficiency of the antenna. A loading profile with an included capacitive loading will hence be investigated as an improvement over the resistive Wu-King profile current utilized on the borehole radar antenna.

## 5.5 Design of a resistive/capacitive loading profile for an insulated borehole antenna

An impedance loading profile for the loaded arm of the borehole radar antenna will now be designed and evaluated. The borehole antenna must have good performance in both air- and water-filled boreholes and it will be designed with a level of capacitive loading included.

Designing a loading profile for the insulated antenna in homogeneous rock or in a borehole is however not a trivial problem. The Wu-King impedance distribution of 5.1 is designed for a bare antenna in a homogeneous ambient medium, while the borehole radar antenna, due to the presence of the borehole and several insulation layers, is a conductor centered in a cylindrically stratified medium. The Wu-King profile is hence not directly applicable to the design of a loading profile for the borehole antenna.

### 5.5.1 The Wu-King profile modified for insulated antennas

The profile is however still approximately valid, given the following considerations. The parameter  $\epsilon_r$  occurs in the Wu-King profile of equation 5.1 as the relative permittivity of the ambient medium. However, reviewing the derivation of the profile, it is clear the the factor  $1/\sqrt{\epsilon_r}$  in 5.1 originates from the propagation speed of the zeroth order current wave along the antenna. When designing a profile for a stratified medium,  $\epsilon_r$  must hence be set to correspond to the wave propagation speed along the antenna, namely  $v = c/\sqrt{\epsilon_r}$ . The parameter  $\epsilon_r$  corresponding to the propagation speed will be termed the *equivalent permittivity*.

The propagation speed of axial current may be determined from  $v = \omega/Re[k_L]$ , where  $k_L$  is the wavenumber of the zeroth order current wave, that may be calculated from

equation 2.7 of Chen and Warne’s transmission line model of insulated antennas presented in Chapter 2. The wavenumber of equation 2.7 is accurate when the external medium is electrically dense relative to the insulation, or, labeling the different media as in Figure 2.6, when  $|k_4|^2 \geq 2|k_2|^2$ . The practical implications of this inequality is that the wavenumber may be determined accurately for the borehole antenna in homogeneous rock or an air-filled borehole<sup>7</sup>. The exact propagation constant may also be determined for any antenna with a single insulation layer in a homogeneous medium from the transcendental equation B.22 presented in Appendix B.

The parameter  $\Psi$  in equation 5.1 is however strictly not valid in a stratified medium, since it is computed from an integral equation for the current utilizing the Green’s function for a homogeneous medium.  $\Psi$  computed for a bare antenna in a homogeneous medium is however still a fair approximation when the cross-section of the insulation and borehole layers around the antenna is electrically small in the external medium, in other words, if  $k_4 b \ll 1$  and  $k_4 c \ll 1$ . The latter inequalities generally hold at lower frequencies and with narrower boreholes.

The Wu-King profile may hence be considered approximately valid for design of an impedance profile for the borehole antenna in homogeneous rock and in air-filled boreholes, when the parameter  $\epsilon_r$  corresponds to the propagation speed  $c/\sqrt{\epsilon_r}$  of zeroth order current waves along the antenna.

The scaling of the feed-point characteristics of a Wu-King antenna with changing  $\epsilon_r$  investigated in section 5.3.1 and the conclusion from section 5.3.2 that a degraded step response results from using a Wu-King loaded antenna in a medium with  $\epsilon_r$  higher than for which it was designed, remain valid. However, the parameter  $\epsilon_r$  now corresponds to the axial wave propagation speed and not to the relative permittivity of the ambient medium. The feed-point current step response hence has a longer settling time when the equivalent  $\epsilon_r$  is high, or equivalently, when the propagation speed is low.

The equivalent permittivity for the loaded arm of the borehole radar antenna, calculated using the transmission line theory, is illustrated in Figure 5.11 for the antenna in 100 mm and 50 mm air-filled boreholes, homogeneous rock ( $\epsilon_{r4} = 9$ ) and homogeneous water ( $\epsilon_{r4} = 81$ ). The latter two geometries may respectively be viewed as a water-filled borehole with a radius of zero and infinity. The value of equivalent  $\epsilon_r$  for a water-filled borehole with a finite radius must hence lie in between the two curves.

The resistive loading profile on the borehole radar antenna still corresponds to a profile designed for  $\epsilon_r = 1$ , and scaled furthermore by 150%. The loading will cause the deterioration of the feed-point current step response settling time illustrated in section 5.3 when

---

<sup>7</sup>The transmission line model cannot model antennas in a water-filled borehole, as explained in section 2.3.1

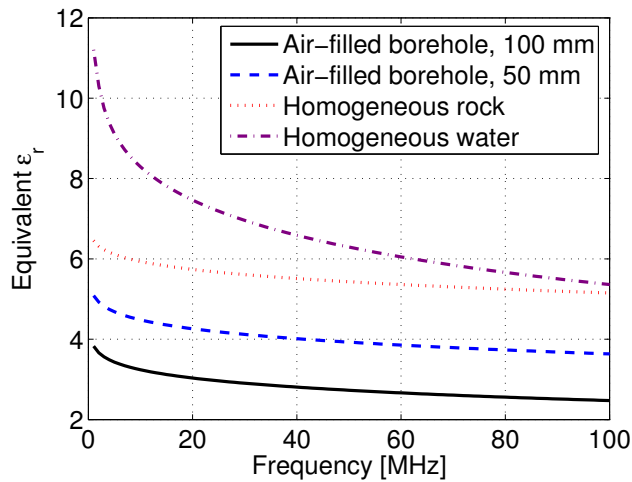


**Figure 5.11:** *The effective relative permittivity corresponding to the propagation speed of zeroth order current waves along the borehole antenna loaded arm in several borehole environments*

placed in environments with high effective permittivities as illustrated in Figure 5.11. This effect, namely a quick initial discharge followed by prolonged late-time discharge, is clearly visible in the feed-point current data of the borehole radar antenna presented in Chapter 3.

The equivalent permittivity is furthermore frequency dependent, notably for electrically dense media, increasing at low frequencies as the electrical size of the insulation around the antenna becomes smaller. The required resistive loading for the Wu-King profile according to equation 5.1 hence decreases at lower frequencies. Figure 5.12 shows the required resistive loading for the borehole antenna loaded arm in homogeneous rock ( $\epsilon_{r4} = 9$ ) and water ( $\epsilon_{r4} = 81$ ) at  $z = 0$ .

A property of the Wu-King dipole in homogeneous media that gives it good wide-band performance is the slow variation of required resistive loading with frequency at low frequencies. The decrease in required resistive loading for antenna in a cylindrically stratified medium, although relatively small, inherently leads to degraded wide-band performance since a profile designed for a specified frequency will have a level of loading either too high or insufficient at other frequencies. A Wu-King loaded antenna in a stratified medium hence has inherently worse wide-band performance than a Wu-King antenna in an homogeneous medium.

### 5.5.2 A Wu-King profile for a cylindrically stratified medium

The modified Wu-King profile presented in the previous section is only approximately valid, and a better design approach would be the use of a non-reflective impedance loading

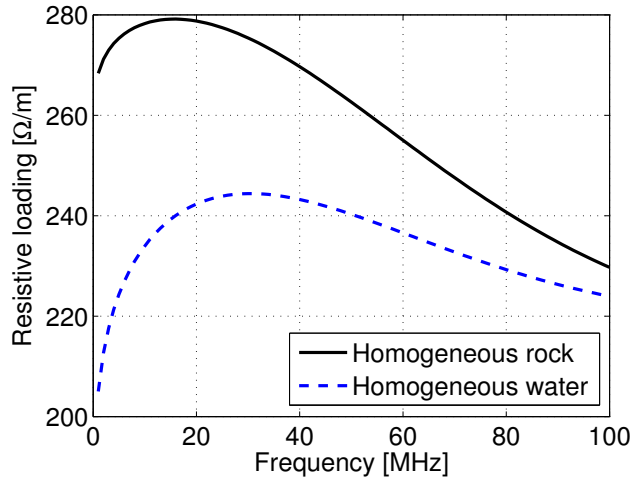


**Figure 5.12:** The required resistive loading at  $z = 0$  for the borehole antenna loaded arm in homogeneous rock ( $\epsilon_{r4} = 9$ ) and homogeneous water ( $\epsilon_{r4} = 81$ )

profile derived specifically for an antenna in a cylindrically stratified medium. Such a profile is derived in Appendix H for a wire with a single insulation layer in a homogeneous medium. The loading profile as a function of length along the antenna is given by

$$z^i(z) = \frac{2\zeta_2\Psi_s}{h - |z|} \quad (5.20)$$

with

$$\Psi_S = \frac{k_L}{2\pi k_2} \left[ \ln\left(\frac{b}{a}\right) + \frac{k_2^2}{k_4^2} \frac{H_0^2(k_4 b)}{k_4 b H_1^2(k_4 b)} \right] \quad (5.21)$$

where  $\zeta_2$  is the wave impedance in the insulation, region 2, again labeling the geometry of the insulated antenna as in Figure 2.6. While the expression for the impedance distribution 5.20 is valid in general, the expression for  $\Psi_s$  is only valid when  $|k_4|^2 \geq 2|k_2|^2$ , since it was derived by King and Smith [16, p. 508] using an approximation to the kernel for the stratified medium that holds given the latter inequality. Although the profile is designed for a conductor with a single insulation layer, the effect of several layers may be incorporated into a single equivalent insulation layer, using the transmission line model of Chapter 2. Due to its dependence on the transmission line model, this loading profile is also practically valid for the borehole antenna in homogeneous rock and air-filled boreholes.

The two profiles for the design of loading profiles in cylindrically stratified media, respectively referred to as the *modified Wu-King* and the *stratified Wu-King* profiles, will be compared by investigating the level of impedance loading for the borehole antenna loaded arm, with  $h = 0.6$  m and cross-sectional geometry as in Figure 2.6, at  $z = 0$  over a range of frequencies. Figure 5.13 illustrates the level of impedance loading for the

borehole antenna in homogeneous rock for the two different profiles. The transmission line model was implemented to calculate the value of  $\epsilon_r$  corresponding to the propagation speed along the antenna for the modified Wu-King profile, and to define a single insulation layer equivalent to the borehole antenna's three layers for the stratified Wu-King profile.

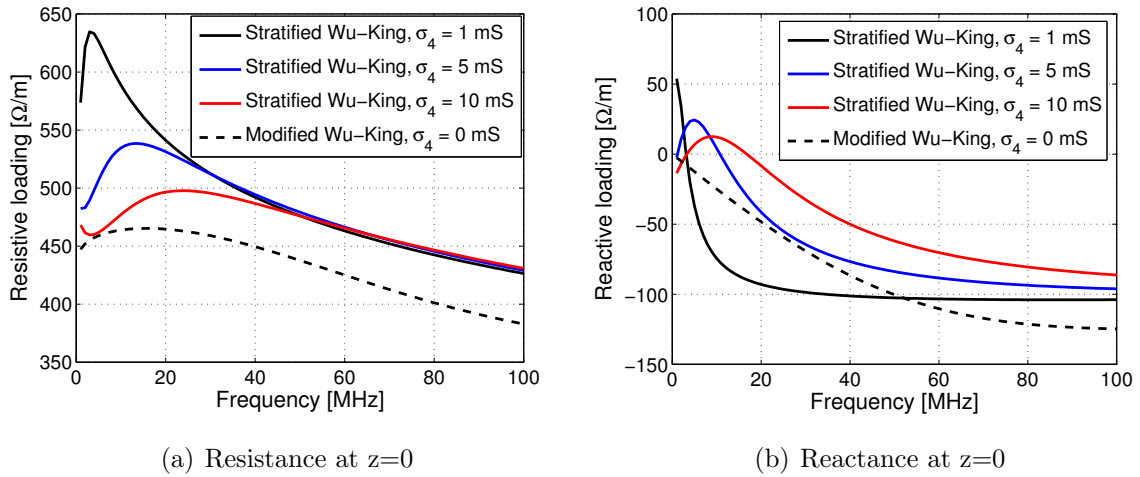


**Figure 5.13:** Comparison of the required loading at  $z = 0$  for the homogeneous and stratified Wu-King profiles for a insulated dipole with the cross-sectional geometry of the borehole antenna loaded arm and  $h = 0.6$  m in homogeneous rock ( $\epsilon_r = 9$ )

The approximate expression for  $\Psi_S$  in equation 5.21, derived by Smith and King in [16, p. 508], unfortunately shows the same sensitivity to ambient medium conductivity as encountered in Chapter 2 in Smith and King's as well as Chen and Warne's accurate transmission line models of insulated antennas. To illustrate this effect, the required impedance loading for the stratified profile is shown in Figure 5.13 for a range of ambient medium conductivities. At higher frequencies the stratified Wu-King profile's required impedance loading for different conductivities converges to values that are comparable (within 10%) to that of the modified Wu-King profile, creating some confidence in the validity of both profiles. The conductivity dependent variation in required resistive loading and the change of the reactive profile from capacitive to inductive at low frequencies is however unexpected and greatly diverges from the behaviour of the modified Wu-King profile.

The derived profile for the stratified medium can hence not be used reliably. It is suspected that this behaviour of the approximation to the parameter  $\Psi_S$  is closely related to the unphysical conductivity dependent behaviour observed in the transmission line model approximations to the input impedance considered in Chapter 2. Deeper investigation into the approximation to the kernel for the current integral equation for an insulated antenna derived by Smith and King [16] and Chen and Warne [4] was unfortunately restricted by the scope and time limits of this project.

### 5.5.3 Practical design considerations

This section shortly outlines relevant issues in the practical design of an impedance loading profile and proposes designs for use on the borehole radar antenna loaded arm. The modified Wu-King profile, discussed in section 5.5.1, will be utilized in the profile calculation since the loading profile derived specifically for stratified media in the previous section requires further investigation.

Two profiles will be designed for eventual evaluation on the borehole radar antenna, both with series capacitive loading included to obtain a current step response with a reduced settling time. Firstly, an antenna will be designed for the electrically dense borehole environment with a large capacitive loading included to investigate both the environmental sensitivity of the antenna and possible gains in radiation efficiency. Secondly, a profile with resistive loading designed for free space and small capacitive (large reactive) loading will be designed, as results from section 5.4 suggest that such a design will have adequate performance in environments ranging from free space to water-filled boreholes.

The design medium for the first profile is arbitrarily chosen as homogeneous rock ( $\epsilon_{r4} = 9$ ), as a middle ground between an air-filled and water-filled borehole. As a first iteration, the design frequency is chosen as the highest frequency of interest for radar operation, namely 100 MHz, ensuring a higher than required reactive loading over the entire bandwidth and that the reactive loading at lower frequencies will be substantially higher than required. The transmission line model predicts an equivalent permittivity of  $\epsilon_r = 5.1$  for the borehole antenna loaded arm at 100 MHz. Using these parameters in equation 5.1 yields the impedance profile for the antenna in a borehole environment.

It was discovered that scaling the impedance profile calculated above for the electrically dense borehole environment by a factor of  $\alpha = 4$ , the level of resistive loading is similar to that currently implemented on the loaded arm of the borehole antenna. This profile, with the associated capacitive loading included is hence used as the second design. The two designed impedance profiles will be respectively referred to as the 100% and the 400% Wu-King profiles.

An impedance profile may be practically implemented as a discrete approximation of the continuous Wu-King loading profile by placing  $N$  lumped impedances at regular intervals  $\Delta h = \frac{h}{N}$  along the antenna. The value for the  $n^{th}$  lumped impedance  $Z_n$  for  $n = 1 \dots N$  is calculated as

$$Z_n = z^i(z_n)\Delta h \quad (5.22)$$

where  $z^i$  is the expression for the continuous loading profile and  $z_n = z_0 + n(\Delta h)$  is the position of the  $n^{th}$  lumped element along the antenna, measured from the feed-point. The approximation to the continuous Wu-King profile is better if the number of lumped impedances  $N$  is large. However, previous studies [15] have shown that small but

significant improvements in radiation efficiency are possible when using smaller numbers of lumped elements to implement the continuous profile. A study by Popović [21] placed a lower limit on the number of elements required to create a traveling wave current distribution on an antenna. Popović found that when  $\Delta h \geq 0.15\lambda$ , the antenna current distribution of the discrete implementation of the loading profile is no longer non-reflective. Keller arrived at a similar result, namely  $\Delta h \geq \frac{1}{6}\lambda$  [15].

A small gain in efficiency from using less lumped elements is however secondary to upholding a traveling wave current distribution on the antenna up to a frequency higher than that of interest for radar operation. The number of lumped elements was hence chosen as  $N = 8$  giving  $\Delta h = 75$  mm, which according to the relation  $\Delta h \leq 0.15\lambda$ , would uphold the traveling wave current distribution up to a frequency of 200 MHz for a worst case scenario of  $\epsilon_r = 9$ .

The component values and distances from the feed-point for the 8 lumped elements of the 100% and 400% discrete resistive/capacitive Wu-King profiles designed in the described manner is presented in Table 5.1.

**Table 5.1:** *Proposed loading profiles for the insulated borehole antenna*

n	Position from feed [mm]	100% Wu-King		400% Wu-King	
		$R_n$ [ $\Omega$ ]	$C_n$ [pF]	$R_n$ [ $\Omega$ ]	$C_n$ [pF]
1	37.5	30.9	158	123	39.6
2	112.5	35.6	137	142	34.3
3	187.5	42.1	116	168	29.0
4	262.5	51.5	95.0	206	23.7
5	337.5	66.2	73.8	265	18.5
6	412.5	92.8	52.7	371	13.2
7	487.5	155	31.6	620	7.89
8	562.5	469	10.4	1.86k	2.61

## 5.6 Evaluation of the resistive/capacitive profile

The performance of the borehole radar antenna with loaded arm implemented using the resistive/capacitive profiles proposed in the previous section was evaluated in numerical simulations and in field experiments, the results of which are presented in this section.

### 5.6.1 Simulations

#### Input impedance

Simulations using the CST Microwave Studio model of the borehole antenna with resistive/capacitive loading profiles given in Table 5.1 were carried out in 3 different borehole environments, namely 75 mm air-filled, 75 mm water-filled and 200 mm water-filled boreholes. These environments were chosen to correspond to boreholes in which field experiments were to be performed.

The CST Microwave Studio model of the borehole antenna utilized in the simulations is as described in Chapter 2, with all but the loading profile remaining unchanged. The electric parameters of the ambient medium were again taken as  $\epsilon_r = 9$  with negligible conductance while water was modelled with  $\epsilon_r = 81$  and  $\sigma = 10$  mS/m.

The input impedance of the antenna with the original resistive, 100% R/C and 400% R/C loading when deployed in the mentioned environments is illustrated in Figure 5.14. The effects of inclusion of capacitive loading and lowering of the resistive profile are as expected, corresponding to those observed in the investigation of Wu-King dipoles in sections 5.3 and 5.4.

The antenna with 400% R/C Wu-King loading, with resistive loading similar to the original resistive profile, has decreased input resistance and increased input reactance at lower frequencies in all environments in comparison with the resistive profile. The antenna with 100% R/C Wu-King loading shows similar behaviour at lower frequencies, while having a substantially lower input reactance due to the lower level of resistive loading.

#### Feed-point current

The ADS circuit model of the borehole radar system T/R-switch, receiver circuit and antenna as introduced in Chapter 3 was utilized to accurately simulate the feed-point current of the different antennas in the respective borehole environments after the transmitter fires. The ADS feed-point model of the antenna utilized the input impedance from the CST simulations as displayed in Figure 5.14.

The resulting feed-point current data is displayed in Figure 5.15. Alongside the linear plot of the current data, a plot of the instantaneous power level ( $I(t)^2 R$ ) corresponding to the residual current is shown in a logarithmic scale. The logarithmic instantaneous power data, normalized with respect to the resistively loaded antenna's maximum instantaneous power, is included to illustrate the levels of residual feed-point current long after the transmitter has fired.

The feed-point discharge current in a 75 mm air-filled borehole, illustrated in Figure 5.15(a), for the antenna with 400% R/C loading is largely similar to that of the antenna

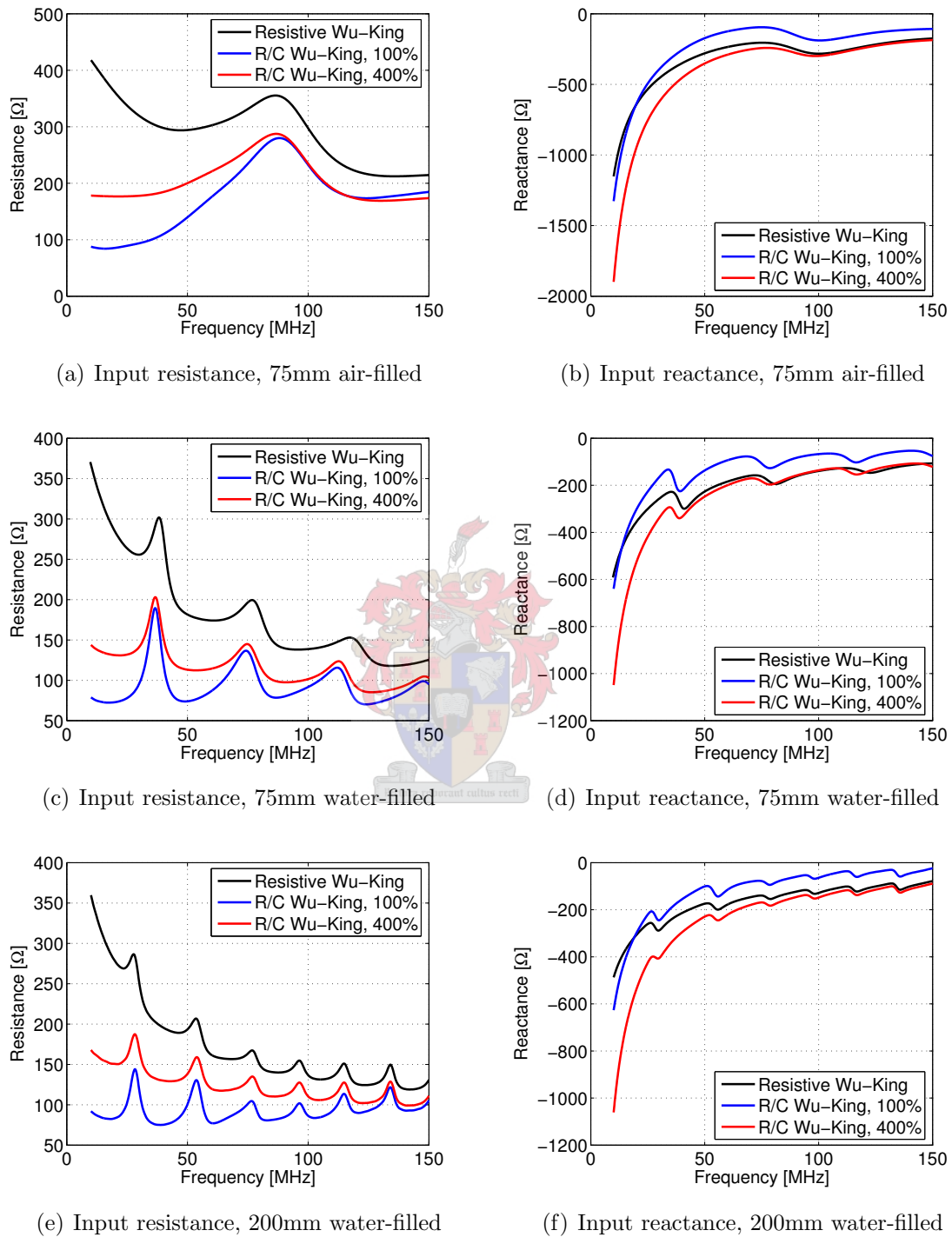


**Figure 5.14:** Comparison of borehole antenna input impedance with different impedance loading profiles from CST Microwave Studio simulations

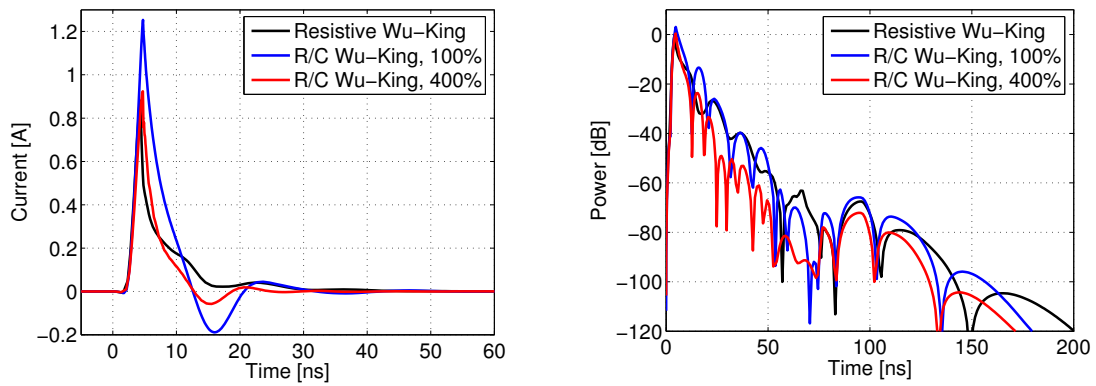
with the original resistive loading, although with a shorter settling time. The antenna with 100% R/C loading is seen to have a slightly larger peak amplitude. The feed-point current settling times for the resistive, 100% R/C and 400% R/C loaded antennas are 37.2 ns, 29.3 ns and 23.1 ns respectively. Although it has a shorter settling time, the residual current on the 100% R/C antenna is of the same order as that on the resistive antenna, as seen in Figure 5.15(b) due to its increased amplitude. The residual power on the 400% R/C antenna is 10–20 dB lower than the other antennas.

In the 75 mm water-filled borehole, the settling times of the resistive/capacitive antennas' initial feed-point current discharge are substantially improved compared to that of the resistively loaded antenna, as illustrated in Figure 5.15(c). Settling times for resistive, 100% R/C and 400% R/C loading are 92.4 ns, 72.9 ns and 42.5 ns respectively. The 100% R/C loaded antenna has a significantly increased peak amplitude and a significant increase in radiation efficiency is hence expected in this environment. The increased amplitude is however again a contributing factor to the relatively high level of residual current on the 100% R/C antenna compared with that of the 400% R/C loaded antenna. The latter antenna maintains a level of residual power that is on average 20 dB lower than that of the resistively loaded antenna.

The resistive/capacitive antennas also have substantially shorter feed-point current settling times in the 200 mm water-filled borehole compared to that of the resistively loaded antenna, as illustrated in Figure 5.15(e). The 100% R/C antenna now has performance similar to 400% R/C antenna, since its implemented resistive profile is higher than required for the wide water-filled borehole. Settling times for the respective antennas are 103 ns, 58.9 ns and 53.1 ns. The antenna with 400% R/C loading still gives the best performance in terms of residual power levels, with the current remaining several decibels below that of the resistively loaded antenna.

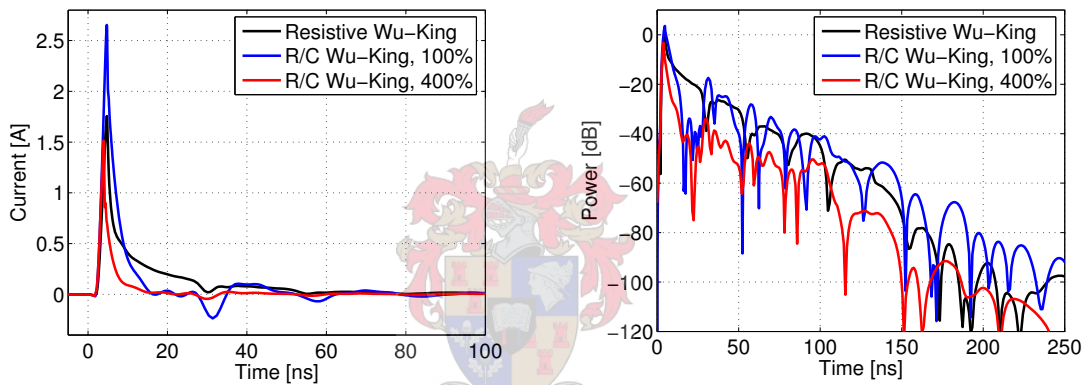
As in Chapter 3, the effects of current pulse reflections from the end-point of the unloaded arm of the borehole antenna, or *late-time ringing*, are clearly visible in the feed-point current data of Figure 5.15. These late-time ringing effects are however clearly more prominent in the antenna with 100% R/C loading, with the relative amplitudes (compared to the peak current value) of the reflected current pulses being substantially larger than for the other two antennas. The increased amplitude of the reflected pulses is a major cause of the longer settling times and high residual current levels in the 75 mm boreholes. The effect is not as prominent in the 200 mm water-filled borehole since the reflected current pulses are damped by the increased radiation efficiency of the antenna in this environment.

It is suspected that the cause of the resistive and 400% R/C antennas' decreased sensitivity to the late-time ringing effects compared to the 100% R/C antenna is due to their high level of resistive loading. As seen in Figure 5.14, these antennas have a higher



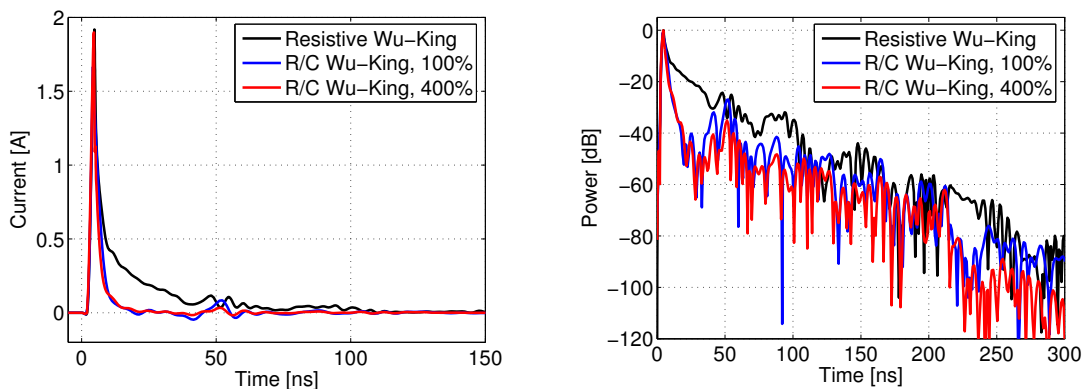
(a) Linear current, 75 mm air-filled

(b) Instantaneous power, 75 mm air-filled



(c) Linear current, 75 mm water-filled

(d) Instantaneous power, 75 mm water-filled



(e) Linear current, 200 mm water-filled

(f) Instantaneous power, 200 mm water-filled

**Figure 5.15:** Comparison of borehole antenna feed-point current discharge curves for different impedance loading profiles shown in linear and logarithmic scales

level of input resistance and reactance compared to the 100% R/C antenna, and hence the mismatch at the feed-point is more severe over the entire frequency band of interest. In the time-domain, current pulses propagating inward from the loaded arm end-point are partially reflected at the feed-point of the antenna. The amplitude of the reflected current will be larger, and that of the transmitted current lower, the more severe the wide-band mismatch at the feed-point. Hence, in this sense, a high resistive loading contributes in the lowering of the effects of late-time ringing in the antenna feed-point current.

The times at which the feed-point current on the R/C antennas fall below levels that cause receiver saturation are however longer than expected and not proportional to the observed settling times of the feed-point current for the different loading profiles. The recovery times<sup>8</sup> of the receiver output voltage, shown in Table 5.2, are also longer than expected when compared to settling times. The settling time for the 400% R/C antenna for example is calculated as 52% that of the resistive antenna in a 200 mm borehole, while the recovery time is 80% that of the resistive antenna.

**Table 5.2:** *Recovery times for antennas with different loading profiles in several borehole environments*

Borehole type	Recovery time [ns]		
	100% R/C Wu-King	400% R/C Wu-King	Resistive Wu-King
75 mm, Air-filled	156	147	173
75 mm, Water-filled	353	210	278
200 mm, Water-filled	407	334	407

The 400% R/C antenna nevertheless has substantially shorter recovery times in all media compared to other antennas. The 100% R/C antenna has recovery times longer than the 400% R/C antennas, especially in the 75 mm water-filled borehole, due to its larger peak current and sensitivity to current end-point reflections. The 400% R/C antenna is hence superior in terms of quick recovery of residual feed-point current.

### Gain and radiated field

The effect of the introduction of capacitive loading on the borehole antenna's gain pattern was investigated in the CST Microwave Studio simulation environment at frequencies of 10 MHz, 70 MHz and 100 MHz. Results are shown in Figure 5.16.

The gain at 10 MHz remains very low in all environments, due to the antennas' large input reactance at low frequencies. The gain from the R/C antennas is however up to

---

<sup>8</sup>Defined in section 3.3.2

10 dB higher than that of the antenna with resistive loading. At higher frequencies in the 75 mm air-filled borehole, the gain patterns of the antennas are practically identical. In the 75 mm water-filled borehole at 70 and 100 MHz, the resistive and 400% R/C antenna have identical gain patterns, while the 100% R/C antenna gives up to 10 dB higher gain at these frequencies. At 70 and 100 MHz in the 200 mm water-filled borehole, the gain pattern of the antenna with resistive loading differs markedly from that of the resistive/capacitive antennas, though its amplitude is generally of the same order as that of the 400% R/C antenna. The antenna with 100% R/C loading once again gives gain up to 10 dB higher than the 400% R/C antenna.

The use of the proposed resistive/capacitive profiles hence does not have a detrimental effect on the gain patterns of the borehole antenna. The use of the 100% R/C profile on the contrary was seen to lead to significant improvements in gain amplitude.

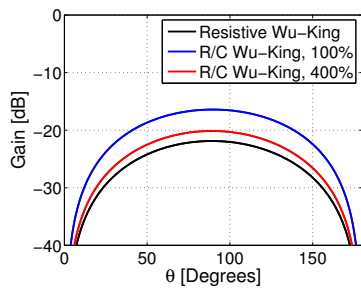
The increase in radiation efficiency due to the use of the 100% R/C profile is however best illustrated in the time domain. The time-domain radiated field was calculated as in Chapter 2 by feeding the CST Microwave Studio model of the borehole antenna with discrete voltage port with a voltage waveform similar to that across the antenna terminals when the transmitter fires. The resulting broadside radiated electric field at a distance of 10 m for the antennas in a 75 mm air-filled and water-filled borehole is shown in Figure 5.17.

The radiated field for the resistive and 400% R/C antennas are, as expected, practically identical, while the radiated field amplitude of the 100% R/C antenna is substantially larger than the other antennas in both environments. Figure 5.17 furthermore illustrates that the use of resistive/capacitive profiles is not detrimental to the time-domain radiated waveform.

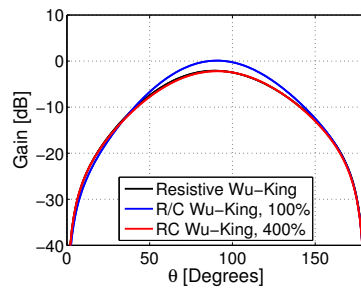
## 5.6.2 Field experiments

The 100% and 400% resistive/capacitive antennas were constructed for conducting field experiments to evaluate the effects of the inclusion of distributed capacitive loading. The loaded conductor on the antenna is implemented as a narrow conducting copper strip interrupted by lumped impedances at specified intervals, ohmically connected to the feed-point through a  $50 \Omega$  TNC connector. Changing the loading profile on the borehole antenna's loaded arm is hence simply a process of replacing the existing loaded copper strip with another.

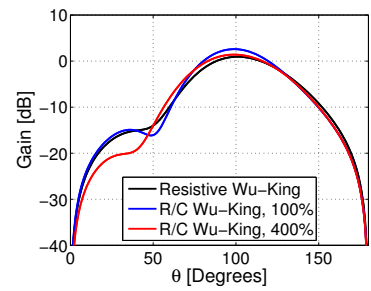
Practically the resistors and capacitors used to implement the series R/C loading cannot both be placed at the specific positions listed in Table 5.1 and have to be offset from one another. The positions of the resistors were offset 5 mm towards and those of the capacitors 5 mm away from the feed-point. This modification has a negligible effect on the performance of the antenna in the frequency band of interest for the radar operation.



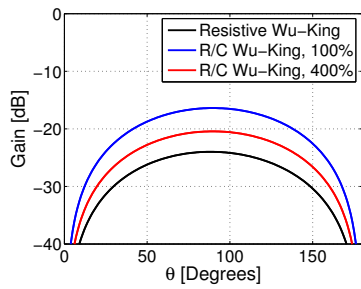
(a) 75 mm air-filled, 10 MHz



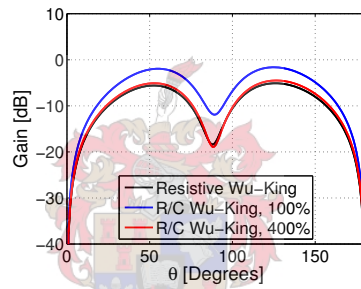
(b) 75 mm air-filled, 70 MHz



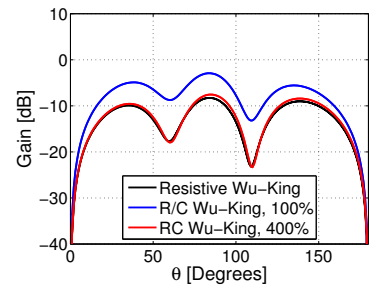
(c) 75 mm air-filled, 100 MHz



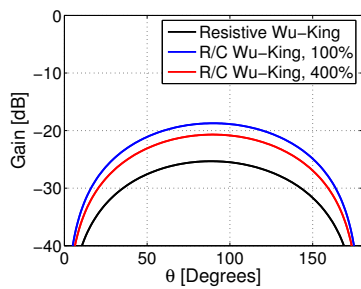
(d) 75 mm water-filled, 10 MHz



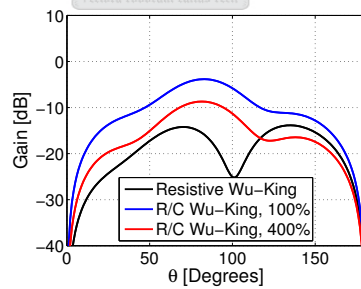
(e) 75 mm water-filled, 70 MHz



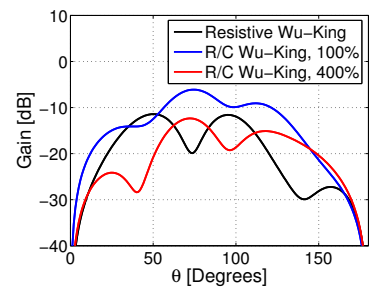
(f) 75 mm air-filled, 100 MHz



(g) 200 mm water-filled, 10 MHz



(h) 200 mm water-filled, 70 MHz



(i) 200 mm water-filled, 100 MHz

**Figure 5.16:** Comparison of borehole antenna gain patterns for different impedance loading profiles in different borehole environments

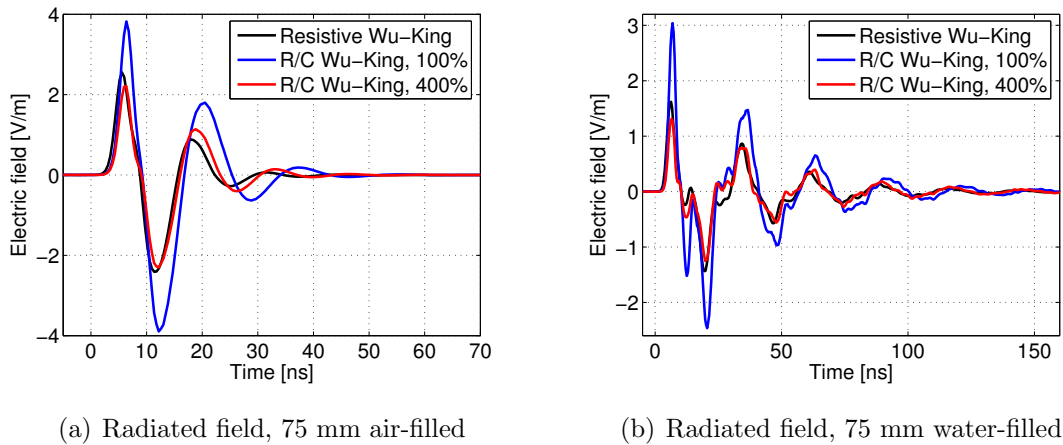


**Figure 5.17:** Comparison of borehole antenna time-domain radiated electric field at broadside at a range of 10 m for differing loading profile for 75 mm air- and water-filled boreholes

Due to initial calculation errors, the resistor and capacitor values on the constructed antennas diverged from those presented in Table 5.1 for the elements farthest away from the antenna feed-point. The difference in performance resulting from this error will however be negligible since the value of the Wu-King conductivity profile near the antenna end-points, where the values of the discrete loading diverge, is close to zero.

### Skuifraam experiment

Initial experiments with the constructed resistive/capacitive antennas were conducted in the Department Water Affairs and Forestry geohydrology borehole SRGT09 on the Skuifraam Dam construction site near Franschoek in August 2005. SRGT09 is a 203 mm diameter borehole with granite as the host rock and is water-filled below its metal casing with water conductivity of 16 mS/m.

For this experiment an Iqua monostatic radar system (IQ314) was modified by removing the current filter implemented to prevent saturation in water-filled boreholes, as described in section 5.1, and the resistively loaded antenna arm was replaced by an antenna arm with 400% R/C loading before deployment in the SRGT09 borehole.

The radar system performed as expected with no prolonged receiver saturation occurring due to residual current, confirming that the use of the resistive/capacitive profile leads to greatly reduced feed-point current settling times in water-filled boreholes. A radar trace from this and a previous experiment using the resistive antenna and included feed-point current filter are shown in Figure 5.18. Data obtained from the SRGT09 borehole is clearly of degraded quality due to a superimposed resonance at 92 MHz, predicted by simulation in Chapter 3 and believed to be of environmental origin, making comparison

of the unprocessed data from the respective antennas difficult. After processing the data obtained using the 400% R/C antenna was found to be of similar quality as that obtained using the current borehole radar system with the resistive antenna.

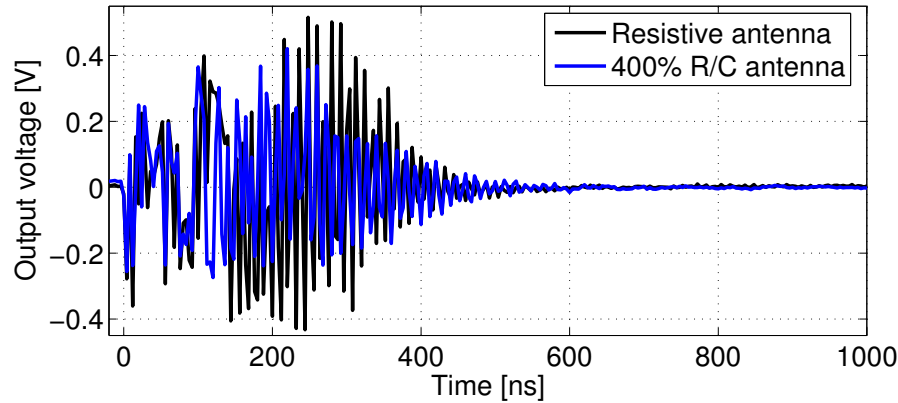


**Figure 5.18:** *Radar traces from the SRGT09 borehole for the resistive and 400% R/C antenna configurations*

An experiment was conducted to investigate the 100% R/C antenna’s predicted increase in radiation efficiency by comparing the amplitude of pulses reflected from radar targets in the unprocessed (*raw*) data from radar systems using the respective antennas. Reflections from targets visible in the raw data when the 100% R/C antenna was used could only be isolated in data from systems that used the resistive and 400% R/C antenna after signal processing, making direct comparisons impossible. An increase in the amplitude of the radiated field with the 100% R/C antenna is hence suspected but could not be directly confirmed or quantified.

### Finsch Diamond Mine experiment

A second experiment was carried out in September 2005 using the 400% R/C antenna at the De Beers Finsch Diamond Mine in borehole F304, utilizing the same radar system (IQ314) and configuration in the initial Skuifraam experiment. Borehole F304 is a NQ (75 mm) water-filled borehole with water conductivity of  $\sim 50$  mS/m and dolomite as the host rock.

Numerous experiments with earlier versions of the monostatic radar system and antenna were carried out in borehole F304. The original unmodified monostatic radar system was deployed in borehole 304 in October 2004 where it experienced severe receiver saturation. The radar system with the implemented high-pass current filter at the feed-point using a resistive antenna was also tested on the same day as the resistive/capacitive antenna. Radar traces from these three experiments at a specific location in the borehole are shown in Figure 5.19.

The inclusion of the current filter at the feed-point with the resistive antenna is clearly an effective solution to the receiver saturation experienced in October 2004. The resistive/capacitive antenna however performs slightly better due to a smaller feed-point current settling time. The inclusion of the feed-point filter or the use of the R/C antenna can not be identified as the sole cause of the reduced prolonged saturation. The modifications to the receiver gain stage as described in section 5.1 may also contribute to reducing the recovery time of the output voltage.

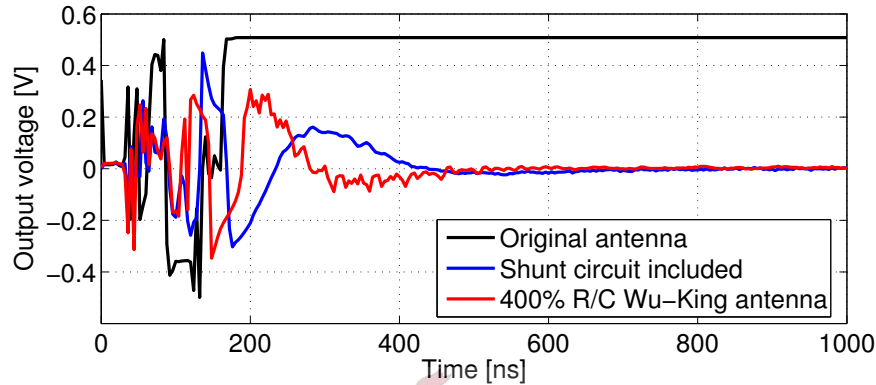


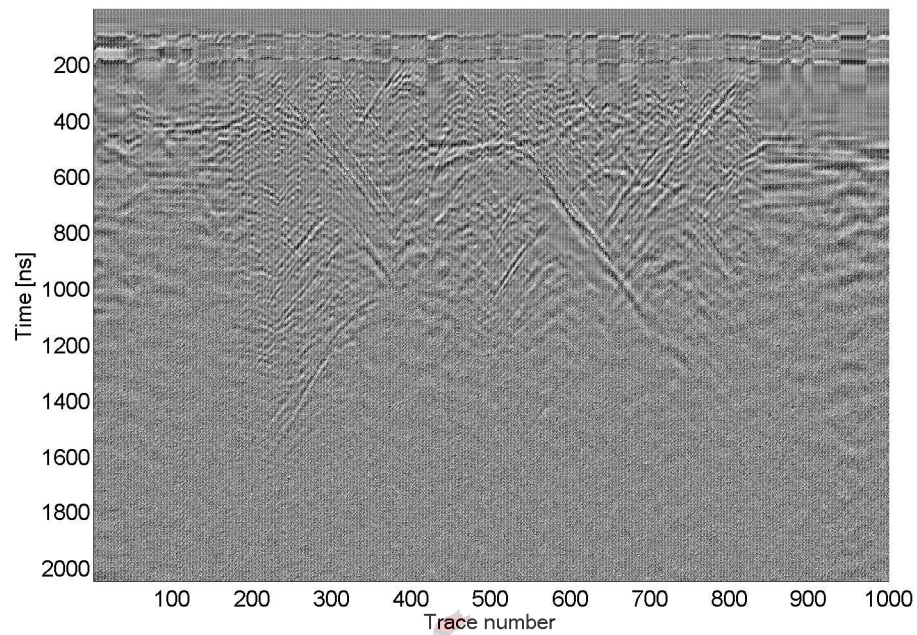
**Figure 5.19:** *Radar traces from the Finch 304 borehole for the different antenna configurations*

The quality of the radar data obtained using the current filter implementation and that using the R/C antenna is compared in Figure 5.20. The data from the two experiments was cropped and processed using identical filter parameters. The quality of the data is clearly comparable, however with the R/C antenna slightly more structure is seen soon after transmitter firing due to the receiver voltage leaving initial saturation earlier.

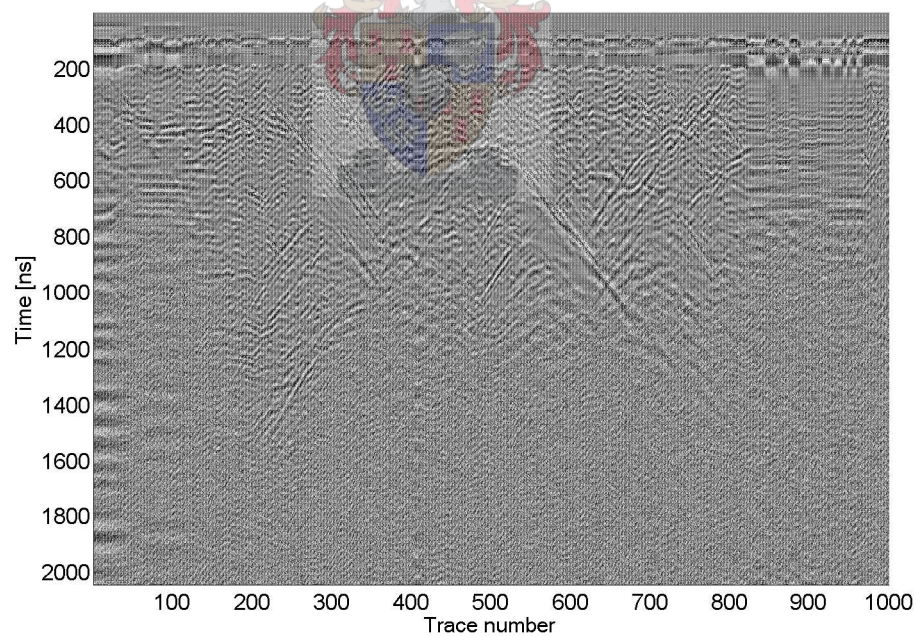
### 5.6.3 Conclusions

The 400% resistive/capacitive antenna's reduced feed-point discharge current settling time was illustrated through numerical simulations and confirmed through experiments in water-filled boreholes. The antenna was shown to reduce prolonged receiver saturation in water-filled boreholes without the need for feed-point current filtering, while producing radar data comparable and in some respects slightly superior to that of the resistive antenna with feed-point current filtering.

Simulations showed the 100% R/C antenna to give an environmentally dependent increase in radiated field amplitude that could unfortunately not be confirmed by experiments. The trade-off for the increased radiation efficiency was seen to be an increased sensitivity of the antenna's feed-point current to late-time ringing on the unloaded antenna arm. Further experiments are needed to assess the quality of data obtained using the 100% R/C antenna.



(a) Radar with feed-point current filter implementation



(b) Radar with R/C antenna

**Figure 5.20:** Comparison of the quality of the radar data obtained using the feed-point current filter implementation with that using the R/C antenna from the 75 mm water-filled borehole F304 at De Beers Finsch Diamond Mines

# Chapter 6

## Conclusions and future work

### 6.1 Conclusions

#### Modelling

The transmission line model of insulated antennas was implemented to compute the current distribution, input impedance and radiated field of the monostatic BHR antenna. Radiated field predictions from the model corresponded well to that of trusted numerical simulation packages. Input impedance results were however found to be inaccurate, since a requirement that the wavenumber in the ambient medium must be much larger than that in the antenna insulation is not met. Transmission line parameters given by Chen and Warne [4] and King and Smith [16] were furthermore shown give to unphysical input impedance in non-conductive ambient media. Although it was utilized in previous projects to model borehole antennas, the transmission line model was hence found to be inadequate for this purpose. Investigations into the monostatic BHR antenna relied solely on numerical simulation.

#### Antenna performance

Electromagnetic field simulation software was utilized to study the BHR antenna's performance in a range of different borehole environments. The interaction of the antenna with radar circuitry was modelled by including the antenna input impedance in an accurate circuit simulation of the radar receiver circuit as an equivalent load. The simulations illustrated a drastic deterioration in performance of the BHR antenna in water-filled boreholes.

The simulated feed-point discharge current after the firing of the transmitter has a much longer settling time than that in air-filled boreholes, confirming results from experimental measurements of the current in water-filled boreholes. The simulated receiver output voltage showed that the longer discharge current settling times in water-filled boreholes leads to prolonged saturation of gain stage amplifiers and data loss.

The radiated electric field waveform was furthermore shown to be drastically degraded and stretched in water-filled boreholes. The antenna hence has poor broadband pulse radiating capabilities in water filled boreholes, impacting negatively on radar resolution.

The monostatic BHR antenna is hence not well suited for deployment in water-filled boreholes.

### Network synthesis

Lumped element networks with driving-point impedances approximately equivalent to the antenna input impedance were successfully synthesized for a range of air-filled and water-filled boreholes. Measured and simulated feed-point discharge current curves for a water-filled borehole corresponded very well to the discharge current obtained by replacing the antenna with the equivalent lumped element network for the corresponding borehole.

### Reduction of feed-point current settling time

The use of a resistive/capacitive loading profile on the BHR antenna loaded arm was proposed as a method for reducing the settling time of the feed-point discharge current. The receiver output voltage of an antenna with an R/C loading profile deployed in a water-filled borehole did not exhibit prolonged saturation as seen in previous experiments. The recovery time of the output voltage was furthermore shorter than when a resistively loaded antenna was used together with an implementation of the feed-point current filter discussed in section 5.1. The use of the R/C loading profile is hence superior to utilizing the feed-point current filter as a solution to the feed-point current problem.

Simulations showed that quantities such as the gain patterns and time-domain radiated field of the antenna are not adversely affected by the introduction of the R/C-profile.

## 6.2 Future work

The following items may be investigated further to improve antenna performance or to gain more insight into the behaviour of the antenna in different media.

- The resistive/capacitive profiles in Chapter 5, Table 5.1 were proposed as first iterations in a design, as a proof of concept that an RC loading profile reduces the feed-point current settling time. Improvement upon the performance of the antennas is almost certainly possible and further investigation into the optimum levels of resistive and capacitive loading for a certain application is needed.
- A quantitative study of the influence of the BHR antenna's degraded time domain radiated field in water-filled boreholes is needed to determine its impact on quantities like the spacial resolution of the radar system.

- The monostatic BHR antenna was shown to be not well suited for use in water-filled boreholes. The antenna's radiated field in water-filled boreholes is severely degraded due to reflections of current at the end-point and the feed-point of the antenna. A solution would be the construction of antenna that is non-resonant in the relevant frequency band, such as a Wu-King dipole.
- In this project a deployed BHR antenna was always modelled as being positioned in the center of a borehole, corresponding to a borehole that is entirely vertical. Practically boreholes are often non-vertical and in this instance a deployed antenna will be offset to the side, making contact with the borehole wall. It is hence also of importance to study the feed-point and radiation characteristics of the antenna in such an environment.
- The ambient medium surrounding the antenna was assumed to be non-conductive in this project. The effects of varied ambient medium conductivity need to be investigated.

Certain theoretical issues not directly related to improving the performance of the BHR antenna were also uncovered and require further investigation:

- A non-reflective impedance profile for an antenna in a 2-layered cylindrically stratified medium was derived in Chapter 5 for the special case of an insulated antenna in a dense medium where the wavenumber in the insulation is much smaller than that in the ambient medium. The profile however shows unexpected large variation at low frequencies due to changes in the ambient medium conductivity. Further investigation as to the cause of this effect and the validity of the profile is needed.
- The unknown propagation mode appearing in wide water-filled boreholes needs to be investigated as it causes a substantial increase in the antenna recovery time, as seen in the Skuifraam experiments in Chapter 5.
- The discovery that the transmission line model of insulated antennas gives unphysical input impedance results in environments of low conductivity was surprising. Further investigation as to the cause of the effect is needed.
- The transmission line model in its current state cannot model antennas in water-filled boreholes. An attempt may be made to extend the model from approximate field solutions of a infinite wire in a 3-layer cylindrically stratified medium, by analogy with the derivation for a 2-layer stratified medium given in appendix B.

# Bibliography

- [1] BOTT, R. and DUFFIN, R., “Impedance synthesis without use of transformers.” *Journal of Applied Physics*, August 1949, Vol. 20, No. 8, p. 816.
- [2] BRUNE, O., “Synthesis of a finite two-terminal network whose driving-point impedance is a prescribed function of frequency.” *Journal of Mathematical Physics*, 1931, Vol. 10, pp. 191–236.
- [3] BUTLER, C. M., “The equivalent radius of a narrow conducting strip.” *IEEE Transactions on Antennas and Propagation*, July 1982, Vol. 30, No. 4, pp. 755–758.
- [4] CHEN, K. C. and WARNE, L. K., “A uniformly valid loaded antenna theory.” *IEEE Transactions on Antennas and Propagation*, November 1992, Vol. 40, No. 11, pp. 1313–1323.
- [5] CLAASSEN, D. M., *Electromagnetic characterization of a wideband borehole radar imaging system*. PhD thesis, University of Oxford, 1995.
- [6] Computer Simulation Technology. *CST Microwave Studio 5 - Advanced topics user manual*, 2003. [www.cst.com](http://www.cst.com).
- [7] DESCHAMPS, G. A., “Impedance of an antenna in a conducting medium.” *IRE Transactions on Antennas and Propagation*, September 1962, Vol. 10, pp. 648–650.
- [8] EMSS, Technopark, Stellenbosch, 7600, South Africa. *FEKO - User's Manual, Suite 5.0*, 2005. [www.feko.info](http://www.feko.info).
- [9] GUILLEMIN, E. A., *Synthesis of passive networks*. Huntington, New York: Robert E. Krieger Publishing Co., 1977.
- [10] HARGREAVES, J., *A Multichannel borehole radar for three dimensional imaging*. PhD thesis, University of Oxford, 1995.
- [11] HARRINGTON, R. F., *Time-Harmonic Electromagnetic Fields*. New York: McGraw-Hill Book Company, Inc., 1961.

- [12] HERSELMAN, P. Le R., *Borehole radar system analysis in stratified geological systems applied to imaging of platiniferous reefs in the Bushveld Igneous Complex*. PhD thesis, University of Stellenbosch, 2003.
- [13] KANDA, M., "A relatively short cylindrical broadband antenna with tapered resistive loading for picosecond pulse measurements." *IEEE Transactions of Antennas and Propagation*, May 1978, Vol. 26, No. 3, pp. 439–447.
- [14] KANDA, M., "Time domain sensors for radiated impulsive measurements." *IEEE Transactions of Antennas and Propagation*, May 1983, Vol. 31, No. 3, pp. 438–444.
- [15] KELLER, S., "Design of impedance loaded antennas for borehole radar applications." Master's thesis, University of Karlsruhe, 2000.
- [16] KING, R. W. P. and SMITH, G. S., *Antennas in Matter*. Cambridge, Massachusetts: MIT Press, 1981.
- [17] KING, R. W. P., TREMBLY, B. S., and STROHBEHN, J. W., "The electromagnetic field of an insulated antenna in a conducting or dielectric medium." *IEEE Transactions on Microwave Theory and Techniques*, July 1983, Vol. 31, No. 7, pp. 574–583.
- [18] LEVI, E. C., "Complex curve fitting." *IRE Trans. on Automatic Control*, 1959, pp. 37–44.
- [19] MALONEY, J. and SMITH, G., "A study of transient radiation from the Wu-King resistive monopole - FDTD analysis and experimental measurements." *IEEE Transactions of Antennas and Propagation*, May 1993, Vol. 41, No. 5, pp. 668–676.
- [20] MONTOYA, T., "A study of pulse radiation from several broad-band loaded monopoles." *IEEE Transactions of Antennas and Propagation*, August 1996, Vol. 44, No. 8, pp. 1172–1182.
- [21] POPOVIĆ, B. D., "Theory of cylindrical antennas with lumped impedance loadings." *The Radio and Electronic Engineer*, April 1973, Vol. 43, No. 4, pp. 243–248.
- [22] RÜTSCHLIN, M., *Non-destructive measurement of the radio frequency properties of hard rock borehole cores*. PhD thesis, University of Stellenbosch, 2005.
- [23] SHEN, L. and WU, T. T., "Cylindrical antenna with tapered resistive loading." *Radio Science*, February 1967, Vol. 2, No. 2, pp. 191–201.

- [24] SPIEGEL, M. R. and LIU, J., *Mathematical handbook of formulas and tables*. New York: McGraw-Hill, 1999.
- [25] STUTZMAN, W. L. and THIELE, G. A., *Antenna theory and design*. New York: John Wiley and Sons, Inc., 1998.
- [26] TEMES, G. C. and LAPATRA, J. W., *Introduction to circuit synthesis and design*. McGraw-Hill, 1995.
- [27] VAN DER MERWE, P. J., “The design of a monostatic, ultra wide band, VHF pulse radar for detection of close-in targets.” Master’s thesis, University of Stellenbosch, 2003.
- [28] VAN DER MERWE, P. J., “Eliminating saturation in the monostatic radar.” Private communication, March 2005.
- [29] VAN WYK, M. D., “An active antenna for borehole pulsed radar applications.” Master’s thesis, University of Stellenbosch, 2001.
- [30] WOODS, B. K., “Development of an active pulsed radar receiver for a mono-static borehole-radar tool.” Master’s thesis, University of Stellenbosch, 2003.
- [31] WU, T. T. and KING, R. W. P., “The cylindrical antenna with nonreflecting resistive loading.” *IEEE Transactions on Antennas and Propagation*, May 1965, Vol. 13, No. 3, pp. 369–373.
- [32] WU, T. T. and KING, R. W. P., “The cylindrical antenna with nonreflecting resistive loading - corrections.” *IEEE Transactions on Antennas and Propagation*, November 1965, Vol. 13, p. 998.
- [33] WU, T. T., KING, R. W. P., and GIRI, D. V., “The insulated dipole antenna in a relatively dense medium.” *Radio Science*, July 1973, Vol. 8, No. 7, pp. 699–709.

# Appendix A

## Borehole antenna geometry

This section describes the geometry and material properties of the monostatic BHR probe, as modeled in this project.

The antenna is an asymmetric dipole with a conductive and a loaded arm, as illustrated in Figure A.1. When deployed in a borehole, the antenna is insulated by a PVC tube encasing of outer diameter 32 mm, shown in Figure A.1.

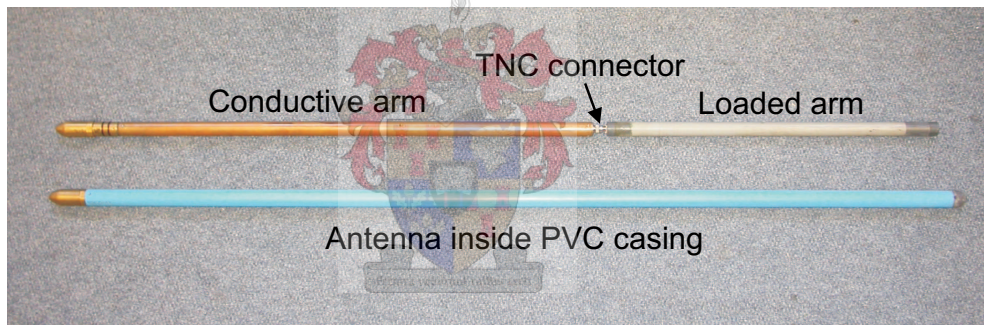


**Figure A.1:** *The monostatic borehole radar system with and without PVC casing*

The conductive arm is a copper cylinder that acts as housing for the receiver and transmitter electronics. A loaded arm of which the insulation layers have been cut open is shown in Figure A.2. The loaded arm is a narrow conducting strip, width 6 mm, seen in Figure A.2 with an implementation of a discrete resistive Wu-King impedance loading profile. The values and positions of the resistors on the loaded arm is shown in Table A.1. The loaded arm is furthermore immersed in a potting material encased in a perspex cylinder, as may also be seen in Figure A.2.

The dimensions of the antenna as modeled in this project is shown in Figures A.3 to A.5. Diagrams are not to scale. The conductive arm is taken as a solid PEC cylinder instead of a hollow copper cylinder since the skin depth of copper at the frequencies of interest several orders smaller than the thickness of the hollow copper cylinder.

All insulation materials on the antenna are good dielectrics at VHF and are hence assumed to be non-conductive for modeling purposes. The relative permittivities of the

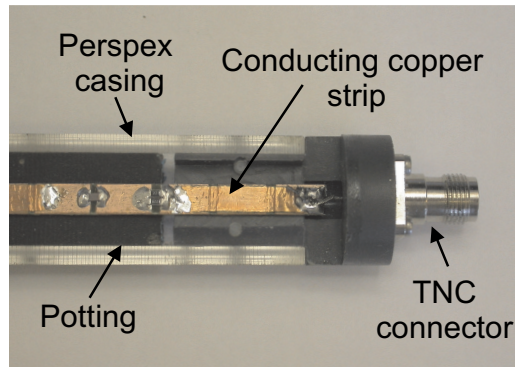


**Figure A.2:** Detail of the loaded arm near the feed-point with insulation layers cut open

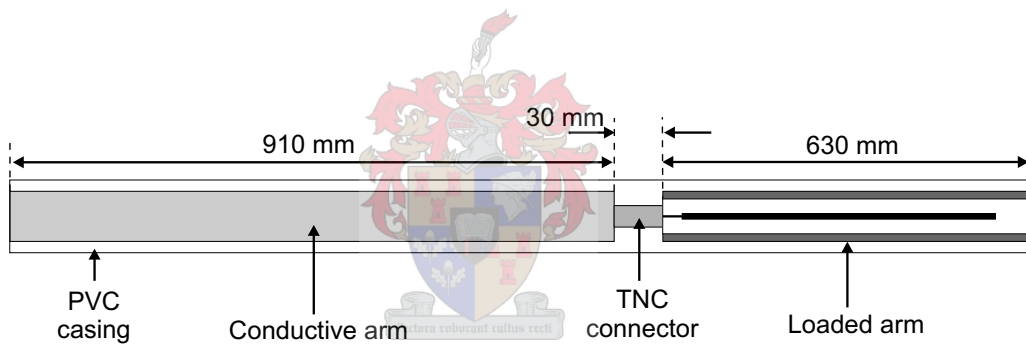


**Figure A.3:** A longitudinal cross-section of the modeled BHR antenna

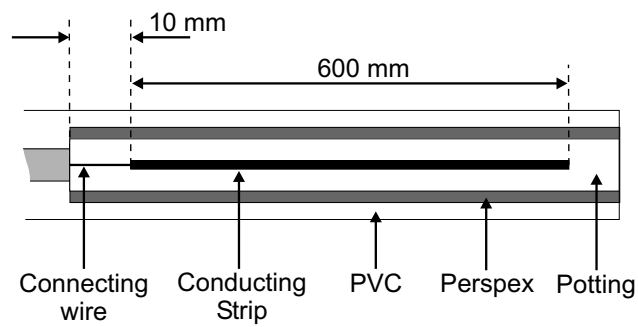


**Figure A.4:** Detail of the longitudinal cross-section of the loaded arm

**Table A.1:** *The resistor values and positions for the 12-element discrete implementation of the resistive Wu-King loading profile*

Element number	Position from feed [mm]	Resistance [ $\Omega$ ]
1	25	77.6
2	75	83.1
3	125	93.8
4	175	103.1
5	225	118.3
6	275	136.2
7	325	160.7
8	375	196
9	425	248.1
10	475	348.8
11	525	563.4
12	575	1918.6

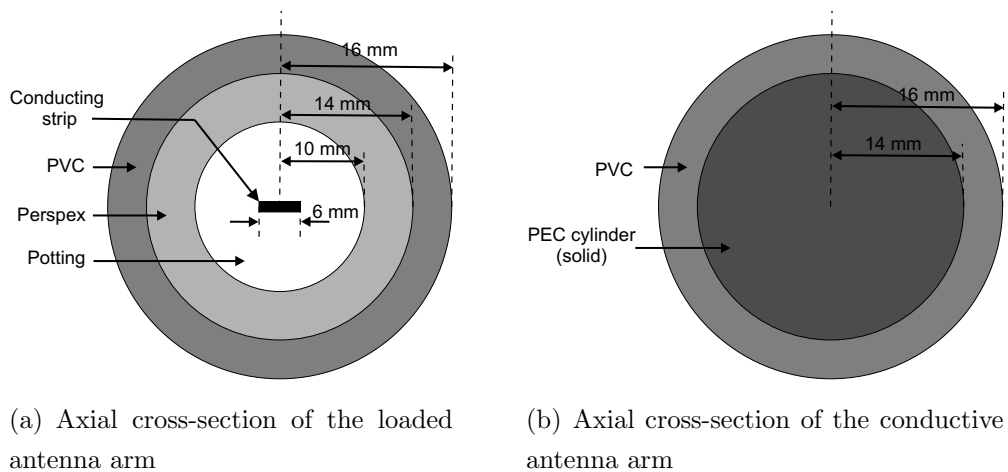


**Figure A.5:** *Cross sections of the loaded and conductive antenna arms*

insulation materials as used for modeling purposes are 3.1 for PVC; 2 for perspex and 3.7 for the potting material<sup>1</sup>.



---

<sup>1</sup>As measured by P. Le R. Herselman [12]

# Appendix B

## Transmission line model derivations

The wavenumber and characteristic impedance of the transmission line model of insulated antennas will now be derived. Both an exact and an approximate solution will be presented. The exact solution gives rise to some computational difficulties since it requires the wavenumber to be solved numerically from a transcendental equation. An approximate, yet direct solution to the field is obtained by assuming a TEM field distribution in the insulation region surrounding the central conductor. The transmission line parameters found using this field solution correspond exactly to those as proposed by Chen and Warne [4], King and Smith [16], *et al.*

### B.1 Exact solution

#### B.1.1 Electromagnetic field of the insulated antenna

The derivation will be carried out for an insulated dipole antenna of half-length  $h$ , with cross-sectional geometry as in figure 2.6. The antenna is positioned at the origin of a standard cylindrical coordinate system, pictured in figure B.1, with its longitudinal axis aligned with the  $z$ -axis. Region 1 in figure 2.6 is assumed to be a PEC conductor, region 2 is a good dielectric, while region 4 is homogeneous, isotropic and infinite in extent. The second insulation layer, region 3, is omitted in the exact field solution for simplicity, and hence  $b = c$ . A permittivity  $\epsilon_i$ , permeability  $\mu_i$  and conductivity  $\sigma_i$  is associated with each region; as well as a complex wavenumber as defined in equation 2.4.

The field is assumed transverse magnetic to  $z$  in anticipation of approximations that will be made at a later stage. For a TM field, the electromagnetic field may be completely described using a magnetic vector potential  $\mathbf{A} = \psi \mathbf{u}_z$ , where  $\mathbf{u}_z$  is the unit vector in the  $z$ -direction [11].  $\psi$  is a scalar potential that satisfies the scalar Helmholtz equation:

$$\frac{1}{\rho} \frac{\partial}{\partial \rho} \left( \rho \frac{\partial \psi}{\partial \rho} \right) + \frac{1}{\rho^2} \frac{\partial^2 \psi}{\partial \phi^2} + \frac{\partial^2 \psi}{\partial z^2} + k^2 \psi = 0 \quad (\text{B.1})$$

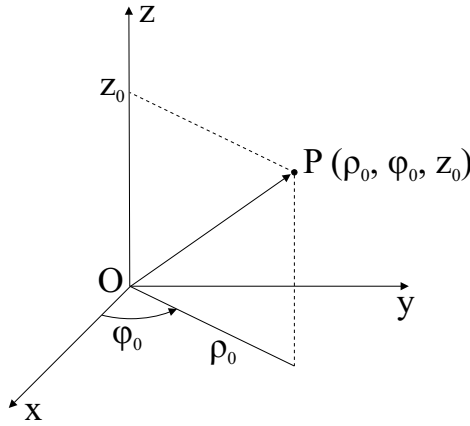


**Figure B.1:** *Circular cylindrical coordinate system*

The method of separation of variables is applied to find solutions of the form:

$$\psi = R(\rho)\Phi(\phi)Z(z) \quad (\text{B.2})$$

Using the definition of  $\psi$  as above, the Helmholtz equation may be separated into the following three equations [11]:

$$\rho \frac{d}{d\rho} \left( \rho \frac{dR}{d\rho} \right) + [(k_\rho \rho)^2 - n^2]R = 0 \quad (\text{B.3})$$

$$\frac{d^2\Phi}{d\phi^2} + n^2\Phi = 0 \quad (\text{B.4})$$

$$\frac{d^2Z}{dz^2} + k_z^2 Z = 0 \quad (\text{B.5})$$

where  $k_\rho$  is defined by

$$k_\rho^2 + k_z^2 = k^2 \quad (\text{B.6})$$

The radial differential equation, equation B.3, is *Bessel's equation* of order  $n$  and its solutions are termed *Bessel functions* of order  $n$ . The differential equations in  $\phi$  and  $z$  are both simple harmonic differential equations.

The ambient region is assumed to be relatively electrically dense with respect to the insulation region:

$$|k_4^2| \gg |k_2^2| \quad (\text{B.7})$$

and the usual transmission line conditions for electrically small cross sections are also assumed to hold:

$$h \gg b > a, \quad k_2 b \ll 1 \quad (\text{B.8})$$

The consequence of these assumptions are that higher propagation modes along the central conductor and end effects are assumed negligible. Only the fundamental propagation mode is present, hence  $n = 0$  in equation B.4 and the field is independent of  $\phi$ .

The potential functions for regions 2 and 4 are chosen to be solutions to the separated Helmholtz equation that are well behaved in accordance to the respective boundary conditions of each region:

$$\psi_2 = \left[ AJ_0(k_{2\rho}\rho) + BH_0^2(k_{2\rho}\rho) \right] e^{-jk_z z} \quad (\text{B.9})$$

$$\psi_4 = DH_0^2(k_{4\rho}\rho) e^{-jk_z z} \quad (\text{B.10})$$

$J_n(x)$  is the Bessel function of the first kind of order  $n$ , while  $H_n^2(x)$  is the Hankel function of the second kind of order  $n$ .  $k_z$  is the yet undetermined axial component of the complex wavenumber for the dominant propagation mode. In the above equation we have assumed identical  $z$ -variation for regions 2 and 4, in anticipation of the phase continuity condition at  $\rho = b$ .

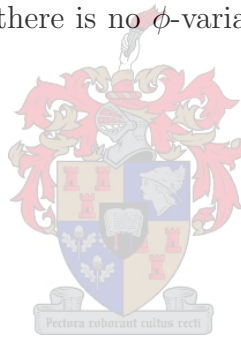
Under the assumption that there is no  $\phi$ -variation, the electromagnetic field is given by [11]:

$$E_\rho = \frac{\omega\mu}{jk^2} \frac{\partial^2 \psi}{\partial \rho \partial z} \quad (\text{B.11})$$

$$E_z = \frac{\omega\mu}{jk^2} \left[ \frac{\partial^2}{\partial z^2} + k^2 \right] \psi \quad (\text{B.12})$$

$$H_\phi = -\frac{\partial \psi}{\partial \rho} \quad (\text{B.13})$$

$$H_z = H_\rho = E_\phi = 0 \quad (\text{B.14})$$



The potential expressions are substituted into equations B.11 to B.14 to obtain the electromagnetic field in each region. The fields are then subject to the following boundary conditions:

- Tangential electric field must be zero at  $\rho = a$
- Tangential electric and magnetic fields must be continuous at  $\rho = b$

If the magnetic field in region 2 is related to the current on the inner conductor through the relation  $I = 2\pi\rho H_\phi$  and the boundary conditions listed above are applied, the solution to the fields are found as follows:

In the insulation, region 2:

$$H_{\phi 2} = \frac{I}{2\pi a} \frac{H_0^2(k_{2\rho}a)J_1(k_{2\rho}\rho) - J_0(k_{2\rho}a)H_1^2(k_{2\rho}\rho)}{H_0^2(k_{2\rho}a)J_1(k_{2\rho}a) - J_0(k_{2\rho}a)H_1^2(k_{2\rho}a)} e^{-jk_z z} \quad (\text{B.15})$$

$$E_{\rho 2} = \frac{\omega\mu I}{2\pi a k_2^2} k_{2z} \frac{H_0^2(k_{2\rho}a)J_1(k_{2\rho}\rho) - J_0(k_{2\rho}a)H_1^2(k_{2\rho}\rho)}{H_0^2(k_{2\rho}a)J_1(k_{2\rho}a) - J_0(k_{2\rho}a)H_1^2(k_{2\rho}a)} e^{-jk_z z} \quad (\text{B.16})$$

$$E_{z2} = \frac{-j\omega\mu I}{2\pi a k_2^2} k_{2\rho} \frac{H_0^2(k_{2\rho}a)J_0(k_{2\rho}\rho) - J_0(k_{2\rho}a)H_0^2(k_{2\rho}\rho)}{H_0^2(k_{2\rho}a)J_1(k_{2\rho}a) - J_0(k_{2\rho}a)H_1^2(k_{2\rho}a)} e^{-jk_z z} \quad (\text{B.17})$$

In the ambient medium, region 4:

$$H_{\phi 4} = \frac{I}{2\pi a} K_{ab} \frac{k_4^2 k_{2\rho} H_1^2(k_{4\rho}\rho)}{k_2^2 k_{4\rho} H_0^2(k_{4\rho}b)} e^{-jk_z z} \quad (\text{B.18})$$

$$E_{\rho 4} = \frac{\omega\mu I}{2\pi a} K_{ab} \frac{k_{2\rho} k_{2z} H_1^2(k_{4\rho}\rho)}{k_2^2 k_{4\rho} H_0^2(k_{4\rho}b)} e^{-jk_z z} \quad (\text{B.19})$$

$$E_{z4} = \frac{-j\omega\mu I}{2\pi a} K_{ab} \frac{k_{2\rho} H_0^2(k_{4\rho}\rho)}{k_2^2 H_0^2(k_{4\rho}b)} e^{-jk_z z} \quad (\text{B.20})$$

where

$$K_{ab} = \frac{H_0^2(k_{2\rho}a)J_0(k_{2\rho}b) - J_0(k_{2\rho}a)H_0^2(k_{2\rho}b)}{H_0^2(k_{2\rho}a)J_1(k_{2\rho}a) - J_0(k_{2\rho}a)H_1^2(k_{2\rho}a)} \quad (\text{B.21})$$

Note that the fields obey the characteristic  $z$ -directed wave impedance for TM waves:  $Z_{TM} = \frac{H_\phi}{E_\rho} = \frac{\omega\mu k_z}{k^2}$ . In the application of the continuity conditions for the fields at  $\rho = b$ , two different values result for the constant  $D$  in equation B.10. The equality of these two values for  $D$  gives rise to a transcendental equation from which the unknown wavenumber  $k_z$  may be solved.

$$\begin{aligned} & \frac{k_2^2}{k_{2\rho}} \left[ H_0^2(k_{2\rho}a)J_1(k_{2\rho}b) - J_0(k_{2\rho}a)H_1^2(k_{2\rho}b) \right] H_0^2(k_{4\rho}b) \\ & - \frac{k_4^2}{k_{4\rho}} \left[ H_0^2(k_{2\rho}a)J_0(k_{2\rho}b) - J_0(k_{2\rho}a)H_0^2(k_{2\rho}b) \right] H_1^2(k_{4\rho}b) = 0 \end{aligned} \quad (\text{B.22})$$

The above expression corresponds exactly to the equation defining the exact solution to the wavenumber for an insulated antenna of infinite length given by King and Smith [16, eq. 3.12, p. 499].

### B.1.2 Transmission line parameters

The electromagnetic fields for the insulated antenna are now solved and it is possible to derive the series impedance and shunt admittance per unit length for the transmission line model. The series impedance per unit length may be derived by considering Faraday's equation in cylindrical coordinates, from which the following relation holds:

$$\frac{\partial E_\rho}{\partial z} - \frac{\partial E_z}{\partial \rho} = -j\omega\mu H_\phi \quad (\text{B.23})$$

By the assumption that the field is TM to  $z$ , there is no  $z$ -directed magnetic field and therefore an electric potential may be defined between two points on an equiphase surface, namely a plane of constant  $z$ -value. The potential on the PEC central conductor, denoted by  $V$ , is defined with respect to  $\rho = \infty$  as

$$V = \int_a^\infty E_\rho d\rho \quad (\text{B.24})$$

Integrating equation B.23 from  $\rho = a$  to  $\rho = \infty$  on a curve of constant  $z$  (chosen as  $z = 0$  for convenience), the following results:

$$\frac{dV}{dz} + j\omega\mu \int_a^\infty H_\phi d\rho = 0 \quad (\text{B.25})$$

The integral of the magnetic field over  $\rho$  has the following result:

$$\int_a^b H_{\phi 2}(z=0) d\rho = \frac{-I}{2\pi a k_{2\rho}} K_{ab} \quad (\text{B.26})$$

$$\int_b^\infty H_{\phi 4}(z=0) d\rho = \frac{I}{2\pi a} \frac{k_4^2 k_{2\rho}}{k_2^2 k_{4\rho}^2} K_{ab} \quad (\text{B.27})$$

On substitution of equations B.26 and B.27, equation B.25 takes on the familiar form of the differential equation for the voltage variation in a transmission line.

$$\frac{dV}{dz} + z_L I = 0 \quad (\text{B.28})$$

where

$$z_L = \frac{j\omega\mu}{2\pi a} K_{ab} \left( \frac{k_4^2 k_{2\rho}}{k_2^2 k_{4\rho}^2} - \frac{1}{k_{2\rho}} \right) \quad (\text{B.29})$$

The shunt admittance per unit length will now be derived. From Ampere's equation in cylindrical coordinates, the following holds:

$$\frac{\partial H_\phi}{\partial z} = \frac{k^2}{j\omega\mu} E_\rho \quad (\text{B.30})$$

The electric potential as defined in equation B.24 is again assumed to exist. Integrating equation B.30 from  $\rho = a$  to  $\rho = \infty$ , we find:

$$V = j\omega\mu \frac{\partial}{\partial z} \int_a^\infty \frac{1}{k^2} H_\phi d\rho \quad (\text{B.31})$$

On substitution of equations B.26 and B.27, equation B.31 takes on the form of the differential equation for current variation in an transmission line:

$$\frac{dI}{dz} + y_L V = 0 \quad (\text{B.32})$$

where

$$y_L = \frac{2\pi a}{j\omega\mu} K_{ab} \frac{k_2^2 k_{4\rho}^2 k_{2\rho}}{k_{4\rho}^2 - k_{2\rho}^2} \quad (\text{B.33})$$

The wavenumber and characteristic impedance of the transmission line model for the insulated antenna is finally given by:

$$k_L = \sqrt{-z_L y_L} \quad (\text{B.34})$$

$$Z_c = \sqrt{\frac{z_L}{y_L}} \quad (\text{B.35})$$

On substitution of the expressions for  $z_L$  and  $y_L$  into B.34,  $k_L$  reduces to  $k_z$ , conforming to the expectation that  $k_L$  must be identical to the wavenumber of the fields' axial propagation. The wavenumber  $k_L$  may hence be solved from the transcendental equation B.22.

## B.2 Approximate field solution

### B.2.1 Approximate electromagnetic field of the insulated antenna

The exact solution for the field requires that  $k_L$  be solved numerically from a transcendental equation, which is inconvenient. Furthermore, the exact equations for  $z_L$  and  $y_L$  derived in the previous section differ from that given by Chen and Warne, King and Smith, *et al.* This section illustrates that under certain reasonable assumptions concerning the electromagnetic field distribution, a direct algebraic solution for  $k_L$  and  $Z_c$  is possible.

The electromagnetic field is again assumed to be TM to  $z$  and hence to be uniquely described by the scalar potential  $\psi$ , as in the previous section. The second insulation layer with outer radius  $c$ , region 3, is now assumed to be present. Assuming that the ambient medium is electrically dense relative to the insulation layers, the following must hold:

$$|k_4^2| \gg |k_3^2|, \quad |k_4^2| \gg |k_2^2| \quad (\text{B.36})$$

In addition to the above inequalities and conditions B.8, it is required that  $k_3 c \ll 1$  for higher propagation modes and end effects to be negligible. By the previous assumption, the wavenumber of region 3 is of the same order as that of region 2.

As a first approximation it is now assumed that waves propagate along the central conductor near the speed of light in the surrounding insulation; and hence  $k_z \approx k_2$ .

Under these approximations the radial component of the wavenumber in the different regions becomes:

$$k_{2\rho} = \sqrt{k_2^2 - k_z^2} \approx 0 \quad (\text{B.37})$$

$$k_{3\rho} = \sqrt{k_3^2 - k_z^2} \approx 0 \quad (\text{B.38})$$

$$k_{4\rho} = \sqrt{k_4^2 - k_z^2} \approx k_4 \quad (\text{B.39})$$

The consequences of these assumptions are that the field in regions 2 and 3 is approximately TEM. The solutions to Bessel's equation B.3 for  $k_\rho = 0$  is the degenerate Bessel function  $\ln(\rho)$  [11]. The scalar potentials  $\psi$  for the different regions are hence chosen as:

$$\psi_2 = A \ln(\rho) e^{-jk_2 z} \quad (\text{B.40})$$

$$\psi_3 = B \ln(\rho) e^{-jk_2 z} \quad (\text{B.41})$$

$$\psi_4 = DH_0^2(k_4 \rho) e^{-jk_2 z} \quad (\text{B.42})$$

The  $z$ -variation of the scalar potential  $\psi$  are again assumed identical in each region in anticipation of the phase continuity conditions at  $\rho = b$  and  $\rho = c$

Relating the current in the inner conductor to the magnetic field in region 2 by  $2\pi\rho H_\phi = I$  and applying continuity of  $H_\phi$  at  $\rho = b$  and  $\rho = c$ , the unknown constants are solved in terms of the current  $I$ . The electromagnetic field in regions 2 to 4 is then given by

$$H_{\phi 2} = \frac{I}{2\pi\rho} e^{-jk_2 z} \quad (\text{B.43})$$

$$E_{\rho 2} = \frac{I}{2\pi} \frac{\omega\mu}{k_2} e^{-jk_2 z} \quad (\text{B.44})$$

$$E_{z 2} = \frac{I}{2\pi} \frac{j\omega\mu}{k_2^2} k_{2\rho}^2 e^{-jk_2 z} \approx 0 \quad (\text{B.45})$$

$$H_{\phi 3} = \frac{I}{2\pi\rho} e^{-jk_2 z} \quad (\text{B.46})$$

$$E_{\rho 3} = \frac{I}{2\pi} \frac{\omega\mu}{k_3} e^{-jk_2 z} \quad (\text{B.47})$$

$$E_{z 3} = \frac{I}{2\pi} \frac{j\omega\mu}{k_3^2} k_{3\rho}^2 e^{-jk_2 z} \approx 0 \quad (\text{B.48})$$

$$H_{\phi 4} = \frac{I}{2\pi b} \frac{H_1^2(k_4 \rho)}{H_1^2(k_4 b)} e^{-jk_2 z} \quad (\text{B.49})$$

$$E_{\rho 4} = \frac{I}{2\pi b} \frac{k_2}{k_4^2} \frac{H_1^2(k_4 \rho)}{H_1^2(k_4 b)} e^{-jk_2 z} \quad (\text{B.50})$$

$$E_{z 4} = -j\omega\mu \frac{I}{2\pi b} \frac{k_2}{k_4^2} \frac{H_0^2(k_4 \rho)}{H_1^2(k_4 b)} e^{-jk_2 z} \quad (\text{B.51})$$

Assuming that  $k_{2p} \approx k_{3p} = 0$  and hence that the fields in the insulation regions are TEM, over-specifies the solution. The consequence is that it appears as if continuity of tangential electric field fails at  $\rho = c$ , since  $E_z$  is zero in the insulation, but non-zero in the ambient medium. It must be remembered that a TEM field is only a first approximation to the field distribution in the insulation, hinged on the assumptions  $E_{z2} \ll E_{\rho2}$  and  $E_{z3} \ll E_{\rho3}$ , and that practically  $E_z$  in the insulation will be non-zero.

## B.2.2 Transmission line parameters

The derivation of the transmission line parameters using the approximate field parallels the corresponding derivation in section B.1.2. The definition of the potential  $V$  as in B.24 is again assumed to hold. The relation B.23 from Faraday's equation is again used to compute the series impedance per unit length. Integrating the magnetic field defined in equations B.43, B.46 and B.49 over  $\rho$ , we find

$$\int_a^b H_{\phi2} d\rho = \frac{I}{2\pi} \ln\left(\frac{b}{a}\right) \quad (\text{B.52})$$

$$\int_b^c H_{\phi3} d\rho = \frac{I}{2\pi} \ln\left(\frac{c}{b}\right) \quad (\text{B.53})$$

$$\int_c^\infty H_{\phi4} d\rho = \frac{I}{2\pi c k_4} \frac{H_0^2(k_4 c)}{H_1^2(k_4 c)} \quad (\text{B.54})$$

and on substitution into equation B.25 we find

$$\frac{d}{dz} V + \left[ \frac{j\omega\mu}{2\pi} \ln\left(\frac{b}{a}\right) + \frac{j\omega\mu}{2\pi} \ln\left(\frac{c}{b}\right) + \frac{j\omega\mu}{2\pi} \frac{H_0^2(k_4 c)}{k_4 c H_1^2(k_4 c)} \right] I = 0 \quad (\text{B.55})$$

which is in the form of equation B.28, the differential equation for voltage variation in a transmission line, with

$$z_L = z_2 + z_3 + z_4 \quad (\text{B.56})$$

where

$$z_2 = \frac{j\omega\mu}{2\pi} \ln\left(\frac{b}{a}\right) \quad (\text{B.57})$$

$$z_3 = \frac{j\omega\mu}{2\pi} \ln\left(\frac{c}{b}\right) \quad (\text{B.58})$$

$$z_4 = \frac{j\omega\mu}{2\pi} \frac{H_0^2(k_4 c)}{k_4 c H_1^2(k_4 c)} \quad (\text{B.59})$$

The series impedance per unit length of the insulation regions 2 and 3 resemble that of a traditional coaxial transmission line. The impedance per unit length of region 4, the ambient medium, represents losses per unit length due to radiation or conduction. If the ambient medium is conductive,  $z_4$  may also be viewed as the internal impedance per

unit length of the tubular conductor extending from  $\rho = c$  to  $\infty$ . The expression for  $z_4$  presented above may in fact also be derived from the definition of internal impedance. When the ambient medium is highly conductive,  $k \rightarrow \infty$  and the contribution from  $z_4$  goes to zero. Note that when  $z_4 = 0$  and  $b = c$ , the series impedance per unit length  $z_L$  is identical to that of a traditional co-axial transmission line.

The relation B.30 from Ampere's equation is again utilized in the computation of the shunt admittance. On substitution of the integral of the magnetic field over  $\rho$  into equation B.31, we find

$$\frac{dI}{dz} - \left[ \frac{j\omega\mu}{2\pi k_2^2} \ln\left(\frac{b}{a}\right) + \frac{j\omega\mu}{2\pi k_3^2} \ln\left(\frac{c}{b}\right) + \frac{j\omega\mu}{2\pi k_4^2} \frac{H_0^2(k_4 c)}{k_4 c H_1^2(k_4 c)} \right]^{-1} V = 0 \quad (\text{B.60})$$

which is in the form of equation B.32, the differential equation for current variation in a transmission line, where

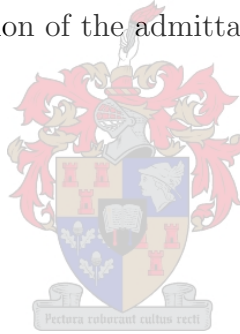
$$y_L = \left[ \frac{1}{y_2} + \frac{1}{y_3} + \frac{1}{y_4} \right]^{-1} \quad (\text{B.61})$$

which is the series combination of the admittances of region 2 to 4, with

$$y_2 = \frac{2\pi j k_2^2}{\omega\mu \ln\left(\frac{b}{a}\right)} \quad (\text{B.62})$$

$$y_3 = \frac{2\pi j k_3^2}{\omega\mu \ln\left(\frac{c}{b}\right)} \quad (\text{B.63})$$

$$y_4 = \frac{2\pi j k_4^2}{\omega\mu} \frac{k_4 c H_1^2(k_4 c)}{H_0^2(k_4 c)} \quad (\text{B.64})$$



When the ambient medium is highly conductive ( $k_4 \rightarrow \infty$ ) and  $b = c$ , the shunt admittance  $y_L$  is identical to that of a traditional co-axial transmission line.

The expressions for  $z_L$  and  $y_L$  derived above match those proposed by Chen and Warne [4]. The derived expressions also match those proposed by Wu, King and Giri [33], with the difference that in the latter it was seemingly assumed that  $y_4 \gg y_2$  and  $y_4 \gg y_3$  and hence that the contribution of  $y_4$  to the combined shunt admittance  $y_L$  is negligible.

The wavenumber  $k_L$  and characteristic impedance  $Z_c$  of the line are computed with equations B.34 and B.35 respectively. Note that  $k_i = \sqrt{z_i y_i}$ ,  $i = 2, 3, 4$  holds for each region.

### B.3 Combined effects of multiple insulation layers

The transmission line model of an insulated antenna containing several dielectric insulation layers may be simplified by combining the respective layers into a single effective insulation layer. This process was used in Chapter 2 to simplify the FEKO model of the borehole antenna through use of equation 2.1, which will now be derived.

As in the previous section, two insulation layers are assumed present with outer radii of  $b$  and  $c$  respectively, with  $c > b$ . The analysis of the previous section showed that the effective series impedance per unit length of the transmission line is simply the impedances of the regions 2 to 4 added in series. It was shown that, if  $k_3c \ll 1$  holds, the series impedance of region 3 is:

$$z_3 = \frac{j\omega\mu}{2\pi} \ln(c/b) \quad (\text{B.65})$$

The impedance of regions 2 and 3 combined is hence simply  $z_2$  and  $z_3$  added in series:

$$z_2 + z_3 = \frac{j\omega\mu}{2\pi} \ln(c/a) \quad (\text{B.66})$$

The above is simply the original expression for  $z_2$ , with  $b$ , the outer radius of region 2, replaced by  $c$ , the outer radius of region 3. Furthermore, the previous section illustrated that the shunt admittance of the transmission line is also just the series combination of that of region 2 to 4. Region 3's shunt admittance was found to be:

$$y_3 = \frac{j2\pi k_3^2}{\omega\mu \ln(c/b)} \quad (\text{B.67})$$

and the combined shunt admittance of regions 2 and 3 is hence:

$$y_L = y_2 y_3 / (y_2 + y_3) \quad (\text{B.68})$$

$$= y_2 \left[ \frac{\ln(b/a)}{\ln(b/a) + n_{23}^2 \ln(c/b)} \right] \quad (\text{B.69})$$

$$= \frac{2\pi\tilde{\epsilon}_2}{\ln(\frac{c}{a})} \left[ \frac{\ln(c/a)}{\ln(b/a) + n_{23}^2 \ln(c/b)} \right] \quad (\text{B.70})$$

where  $n_{23} = k_2/k_3$ . The expression B.70 for the combined shunt admittance resembles that of a insulation layer with outer radius  $c$ . Expressions B.66 and B.70 may hence be seen to effectively absorb the effects of regions 2 and 3 into a single equivalent dielectric insulation layer (labeled as region 2<sub>e</sub>) with outer radius  $c$  and an equivalent permittivity given by:

$$\epsilon_{2_e} = \epsilon_2 \left[ \frac{\ln(c/a)}{\ln(b/a) + n_{23}^2 \ln(c/b)} \right] \quad (\text{B.71})$$

This equation may be applied iteratively to absorb any number of insulation layers, as long as the cross section of the absorbed insulation layer is electrically small. It must be remembered that these expressions are strictly only valid when the inequalities  $|k_4^2| \gg |k_2^2|$  and  $|k_4^2| \gg |k_3^2|$  hold.

# Appendix C

## Current distribution on an insulated dipole

The following derivation assumes that the current distribution on the antenna resembles that of a transmission line, as motivated by the transmission line model of insulated antennas. Using the notation of chapter 2, the following holds for a general transmission line:

$$\frac{dV}{dz} = -z_L I \quad (\text{C.1})$$

$$\frac{dI}{dz} = -y_L V \quad (\text{C.2})$$

which yield the differential equation for current on the transmission line:

$$\left( \frac{d^2}{dz^2} + k_L \right) I(z) = 0 \quad (\text{C.3})$$

As shown in figure 2.8, the insulated dipole is modeled as two transmission line sections, each of length  $h$ , representing the arms of the antenna. A potential difference is created between the two arms by a voltage source  $V_O$ . Solutions for current and voltage distributions that satisfy the above equations are:

$$I(z) = A \cos[k_L(h - |z|)] + B \sin[k_L(h - |z|)], \quad -h < z < h \quad (\text{C.4})$$

$$V(z) = \begin{cases} jZ_c(A \sin[k_L(h - z)] - B \cos[k_L(h - z)]), & 0 \leq z < h \\ -jZ_c(A \sin[k_L(h + z)] - B \cos[k_L(h + z)]), & -h < z < 0 \end{cases} \quad (\text{C.5})$$

where the relation  $k_L/y_L = -j\sqrt{z_L/y_L} = -jZ_c$  was used.

The boundary conditions are

$$I(z = \pm h) = 0 \quad (\text{C.6})$$

$$V(0^+) - V(0^-) = V_O \quad (\text{C.7})$$

which are utilized to solve for the unknown constants in  $A$  and  $B$ . We find:

$$A = 0 \tag{C.8}$$

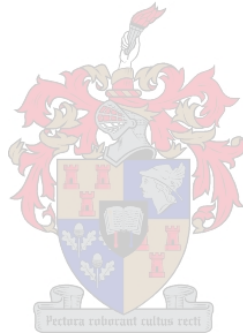
$$B = \frac{jV_O}{2Z_c \cos(k_L h)} \tag{C.9}$$

The current distribution is hence given by

$$I(z) = \frac{jV_O \sin[k_L(h - |z|)]}{2Z_c \cos(k_L h)} \tag{C.10}$$

and the input impedance by

$$Z_{in} = -2jZ_c \cot(k_L h) \tag{C.11}$$



# Appendix D

## Current distribution on a general insulated antenna

When the transmission line model applies, the current distribution on an insulated antenna containing sections of different cross-sectional geometry that are connected through series impedances, may be computed by treating the antenna as a discontinuous transmission line. The model of the borehole antenna will have to be treated in such a manner, to implement the different antenna arm geometries and the discrete Wu-King impedance profile on the loaded arm.

As seen in figure 2.9, the antenna is modelled as  $N$  transmission line sections connected in series, each with its associated complex number  $k_{Lm}$  and characteristic impedance  $Z_{cm}$ . The  $z = 0$  axis is chosen to correspond with left-hand tip of the antenna. The  $m^{\text{th}}$  section starts at  $z = h_{m-1}$  and ends at  $z = h_m$ , having length  $\Delta h_m = h_m - h_{m-1}$ . The current and voltage distribution in each section satisfies equations C.1 to C.3, and, as in appendix C it follows that:

$$I_m(z) = A_m \cos[k_{Lm}(h_m - z)] + B_m \sin[k_{Lm}(h_m - z)] \quad (\text{D.1})$$

$$V_m(z) = jA_m Z_{cm} \sin[k_{Lm}(h_m - z)] - jB_m Z_{cm} \cos[k_{Lm}(h_m - z)] \quad (\text{D.2})$$

with  $m = 1 \dots N$  and  $h_{m-1} < z < h_m$ .

Boundary conditions and current and voltage continuity conditions are applied to solve for the unknown coefficients. Firstly, the current at the ends of the antenna must be zero:

$$I_1(0) = 0 \quad \rightarrow \quad A_1 \cos(k_{L1}h_1) + B_1 \sin(k_{L1}h_1) = 0 \quad (\text{D.3})$$

$$I_N(h_N) = 0 \quad \rightarrow \quad A_N = 0 \quad (\text{D.4})$$

Current continuity between the adjacent ends of transmission line segments,  $I_{m+1}(h_m^+) = I_m(h_m^-)$ , must hold. This yields:

$$A_{m+1} \cos(k_{L(m+1)}\Delta h_{m+1}) + B_{m+1} \sin(k_{L(m+1)}\Delta h_{m+1}) - A_m = 0 \quad (\text{D.5})$$

for  $m = 1 \dots N - 1$ . A very general voltage continuity condition is imposed on the ends of the adjacent transmission lines. It is assumed that a voltage generator  $V_m^e$  and series impedance  $Z_m$  exists between all adjacent ends:

$$V_{m+1}(h_m^+) - V_m(h_m^-) = V_m^e - I_m(h_m)Z_m \quad (\text{D.6})$$

for  $m = 1 \dots N - 1$ , which implies

$$\begin{aligned} jA_{m+1}Z_{cm+1} \sin(k_{L(m+1)}\Delta h_{m+1}) - jB_{m+1}Z_{c(m+1)} \cos(k_{L(m+1)}\Delta h_{m+1}) \\ + jB_m Z_{cm} = V_m^e - A_m Z_m \end{aligned} \quad (\text{D.7})$$

Equations D.3, D.5 and D.7, form a set of  $2N - 1$  simultaneous linear equations with unknowns  $A_m$  and  $B_m$ , with  $A_N$  excluded since  $A_N = 0$  is known. It may be written in matrix form:

$$\mathbf{M}\mathbf{U} = \mathbf{S} \quad (\text{D.8})$$

where  $\mathbf{U} = [A_1 B_1 A_2 B_2 \dots A_{N-1} B_{N-1} B_N]$  is the vector of  $2N - 1$  unknowns.  $\mathbf{S}$  is the source vector and  $\mathbf{M}$  is the boundary condition matrix. The unknown coefficients are solved by computing  $\mathbf{U} = \mathbf{M}^{-1}\mathbf{S}$  in a numerical package such as Matlab.

An example of the boundary condition matrix and source matrix is given below for the simple case of  $N=3$ . Using the notation  $C_i = \cos(k_{Lm}\Delta h_m)$  and  $S_m = \sin(k_{Lm}\Delta h_m)$ , and placing the boundary condition D.3 in the top row, followed by the current and voltage continuity equations for  $m = 1, 2$  and 3:

$$\mathbf{M} = \begin{bmatrix} C_1 & S_1 & 0 & 0 & 0 \\ -1 & 0 & C_2 & S_2 & 0 \\ Z_1 & jZ_{c1} & jZ_{c2}S_2 & -jZ_{c2}C_2 & 0 \\ 0 & 0 & -1 & 0 & S_3 \\ 0 & 0 & Z_2 & jZ_{c2} & -jZ_{c3}C_3 \end{bmatrix} \quad (\text{D.9})$$

The corresponding source vector and vector of unknown is:

$$\mathbf{S} = [0 \ 0 \ V_1^e \ 0 \ V_2^e]^T \quad (\text{D.10})$$

$$\mathbf{U} = [A_1 \ B_1 \ A_2 \ B_2 \ B_3]^T \quad (\text{D.11})$$

Substituting the solved unknowns  $A_m$  and  $B_m$  into equation D.1 gives the current distribution for each section. The input impedance seen by a voltage source  $V_m^e$  at  $h_m$  is simply

$$Z_{in} = \frac{V_m^e}{I_m(h_m)} = \frac{V_m^e}{A_m} \quad (\text{D.12})$$

# Appendix E

## The radiated field of a general insulated antenna

This section derives the radiated field of a general insulated antenna, containing multiple sections, based on a corresponding derivation by Smith and King for an insulated dipole antenna [16].

The radiated electric field of the insulated antenna may be determined from the field distribution on the surface of the insulation [16]:

$$E_{\Theta}^r = \frac{-b}{2r} e^{-jk_4 r} \int_{z'=h_0}^{h_N} e^{jk_4 z' \cos \Theta} \left[ -j\omega B_{4\phi'}(b, z') \sin \Theta J_0(k_4 b \sin \Theta) - k_4 E_{4z'}(b, z') J_1(k_4 b \sin \Theta) \right] dz' \quad (\text{E.1})$$

where

$$B_{4\phi'}(b, z') = B_{2\phi'}(b, z') = \frac{\mu_0}{2\pi b} I(z') \quad (\text{E.2})$$

$$E_{4z'}(b, z') = E_{2z'}(b, z') = \int_{r'=a}^b \left[ \frac{\partial E_{2r}(r', z')}{\partial z'} + j\omega B_{2\phi'}(r', z') \right] dr' \quad (\text{E.3})$$

$$E_{2r}(r', z') = \frac{1}{2\pi r \tilde{\epsilon}_2} q(z') \quad (\text{E.4})$$

and  $q(z')$  is the charge distribution on the antenna. Considering that the charge distribution is related to the current distribution through the law of conservation of charge:

$$q(z) = \frac{-1}{j\omega} \frac{dI(z)}{dz} \quad (\text{E.5})$$

the radial electric field becomes

$$E_{2r} = \frac{j\omega\mu_0}{2\pi k_2^2} \frac{dI(z')}{dz'} \quad (\text{E.6})$$

The differential equation for transmission line current holds

$$\frac{d^2 I(z)}{dz^2} = -k_L^2 I(z') \quad (\text{E.7})$$

so that on substitution of E.6, the axial electric field becomes

$$E_{4z'}(b, z') = \int_a^b \left[ \frac{-j\omega\mu_0 k_L^2}{2\pi r k_2^2} + \frac{j\omega\mu_0}{2\pi r} \right] I(z') dr' \quad (\text{E.8})$$

and after performing the integration

$$E_{4z'}(b, z') = \frac{-j\omega\mu_0}{2\pi} \ln\left(\frac{b}{a}\right) \left[ \frac{k_L^2}{k_2^2} - 1 \right] I(z') \quad (\text{E.9})$$

Note that the inner conductor radius  $a$ ,  $k_2$  and  $k_L$  may be piecewise discontinuous functions of  $z'$ , as it may take on a different value for different sections of the antenna. Substituting E.2 and E.9 into the radiated field equation, we find:

$$E_\Theta^r = \frac{j\omega\mu_0}{4\pi r} e^{-jk_4 r} \int_{h_0}^{h_N} \left[ \sin\Theta J_0(k_4 b \sin\Theta) - k_4 b \ln\left(\frac{b}{a}\right) \left(\frac{k_L^2}{k_2^2} - 1\right) \times J_1(k_4 b \sin\Theta) \right] e^{jk_4 z' \cos\Theta} I(z') dz' \quad (\text{E.10})$$

The integral may be written as the sum of the integrals over each section:

$$E_\Theta^r = \frac{j\omega\mu_0}{4\pi r} e^{-jk_4 r} \sum_{m=1}^N \left[ \sin\Theta J_0(k_4 b \sin\Theta) - k_4 b \ln\left(\frac{b}{a_m}\right) \left(\frac{k_{Lm}^2}{k_{2m}^2} - 1\right) \times J_1(k_4 b \sin\Theta) \right] \int_{h_{m-1}}^{h_m} e^{jk_4 z' \cos\Theta} I_m(z') dz' \quad (\text{E.11})$$

The current  $I_m(z')$  is given by equation D.1 and it follows that the integral over the current in the previous equation is given by

$$\int_{h_{m-1}}^{h_m} e^{jk_4 z' \cos\Theta} I(z') dz' = \frac{e^{jk_4 h_{m-1} \cos\Theta}}{k_{Lm}^2 - k_4^2 \cos^2\Theta} \left[ e^{jk_4 \Delta h_m \cos\Theta} (A_m j k_4 \cos\Theta + B_m k_{Lm}) - j k_4 \cos\Theta (A_m \cos[k_{Lm} \Delta h_m] + B_m \sin[k_{Lm} \Delta h_m]) + k_{Lm} (A_m \sin[k_{Lm} \Delta h_m] - B_m \cos[k_{Lm} \Delta h_m]) \right] \quad (\text{E.12})$$

The constants  $A_m$  and  $B_m$  are taken from the solution from the current distribution as solved in appendix D.

The radiated field of an antenna is usually computed with the source of the antenna at the origin. The source may be placed at the origin by subtracting  $h_s$  from all section lengths, where  $h_s$  is the distance of the source to the origin. Equivalently, a factor  $e^{jk_4 h_s \cos\Theta}$  may be multiplied with equation E.11.

# Appendix F

## Failure of Chen and Warne's transmission line model

Numerical calculations of insulated antenna input impedance using the transmission line model proposed by Chen and Warne [4] produces unphysical input impedance results when the modelled ambient medium is of low conductivity. Input resistance becomes negative at low frequencies and near resonant frequencies for when the ratio of insulation to conductor outer radius  $\frac{b}{a}$  is low.

This section serves to analytically confirm the suspicious numerical results by showing that the expression for input resistance of a insulated dipole in a non-conductive medium becomes negative at low frequencies. Effectively, the failure of Chen and Warne's model will be shown by example.

The ambient medium is assumed to be non-conductive, so that  $k_4$  is real. Furthermore, it is assumed that frequencies are low enough such that  $k_4b \ll 1$  holds. The  $0^{th}$  and  $1^{st}$  order Hankel functions that occur in the expressions for  $z_4$  and  $y_4$  may then be written in terms of their small argument approximations:

$$H_0^2 = 1 + j\frac{2}{\pi} \ln\left(\frac{2}{\tilde{\gamma}k_4b}\right) \quad (\text{F.1})$$

$$H_1^2 = \frac{k_4b}{2} + j\frac{2}{\pi k_4b} \quad (\text{F.2})$$

where  $\tilde{\gamma} = 1.78107^1$ . Substituted into the expression for  $y_4$ , this gives

$$y_4 = \frac{k_4^2}{\omega\mu\left(1 + \frac{4}{\pi^2} \ln^2\left(\frac{2}{\tilde{\gamma}k_4b}\right)\right)} \left\{ \left[ 2(k_4b)^2 \ln\left(\frac{2}{\tilde{\gamma}k_4b}\right) - 4 \right] + j \left[ \pi(k_4b)^2 + \frac{8}{\pi} \ln\left(\frac{2}{\tilde{\gamma}k_4b}\right) \right] \right\} \quad (\text{F.3})$$

---

<sup>1</sup>Related to *Euler's constant*,  $\gamma = 0.57721$ , by  $\tilde{\gamma} = e^\gamma$

The real part of the shunt admittance becomes negative when

$$2(k_4b)^2 \ln\left(\frac{2}{\tilde{\gamma}k_4b}\right) < 4 \quad (\text{F.4})$$

or

$$\frac{2}{\tilde{\gamma}^2} \ln(x) < x^2 \quad (\text{F.5})$$

where  $x = \frac{2}{\tilde{\gamma}k_4b}$ . The above equation holds for all values of  $x$  and hence the real part of the ambient medium shunt admittance  $y_4$  is always negative in the limit  $k_4b \ll 1$ . This singles the expression for  $y_4$  out as a definite contributing cause to the unphysical input impedance results.

The series impedance of the ambient medium,  $z_4$ , using the small argument approximations of the Hankel functions, is:

$$z_4 = \frac{\omega\mu}{\pi^2(k_4b)^4 + 16} \left\{ \left[ 4 - 2(k_4b)^2 \ln\left(\frac{2}{\tilde{\gamma}k_4b}\right) \right] + j \left[ \pi(k_4b)^2 + \frac{8}{\pi} \ln\left(\frac{2}{\tilde{\gamma}k_4b}\right) \right] \right\} \quad (\text{F.6})$$

A comparison of the real part of  $z_4$  with that of  $y_4$  shows that it is always positive in the limit  $k_4b \ll 1$ .

An expression for the approximate input resistance of an insulated dipole antenna of half-length  $h$  will now be derived. The input impedance of a insulated dipole is, from section 2.3.2

$$Z_{in} = -2jZ_c \cot(k_L h) \quad (\text{F.7})$$

The Taylor expansion of  $\cot(k_L h)$  is [24]:

$$\cot(k_L h) = \frac{1}{k_L h} - \frac{k_L h}{3} - \frac{(k_L h)^3}{45} - \dots \quad (\text{F.8})$$

At lower frequencies,  $k_L h \ll 1$  holds and we may neglect the contributions from the 3<sup>rd</sup> and higher order terms. Hence, the input impedance becomes approximately:

$$Z_{in} \approx -2jZ_c \left[ \frac{1}{k_L h} - \frac{k_L h}{3} \right] \quad (\text{F.9})$$

Using the relations  $k_L Z_c = -jZ_L$  and  $\frac{Z_c}{k_L} = \frac{1}{-jY_L}$ , we find

$$Z_{in} = 2 \left[ \frac{1}{hY_L} + \frac{h}{3} Z_L \right] \quad (\text{F.10})$$

Substituting  $y_L = \frac{y_2 y_4}{y_2 + y_4}$  and  $z_L = z_2 + z_4$ , and assuming the impedance and admittance of region 2 is pure imaginary,  $y_2 = j\omega C$  and  $z_2 = j\omega L$ :

$$Z_{in} = \frac{2}{h} \frac{\omega C y_4^* - j|y_4|^2}{\omega C |y_4|^2} + \frac{2h}{3} [j\omega L + z_4] \quad (\text{F.11})$$

of which the real part is

$$Re[Z_{in}] = \frac{2Re[y_4]}{h|y_4|^2} + \frac{2h}{3}Re[z_4] \quad (\text{F.12})$$

It is known that  $Re[y_4] < 0$  and  $Re[z_4] > 0$ , hence the expression for the input resistance of the antenna may become negative in a certain frequency range. This occurs when:

$$\frac{2Re[y_4]}{h|y_4|^2} > -\frac{2h}{3}Re[z_4] \quad (\text{F.13})$$

After some algebraic manipulation and neglecting higher order terms, the above expression simplifies considerably to:

$$k_4^2 < \frac{3}{h^2} \quad (\text{F.14})$$

Rewritten in terms of frequency, the modelled input resistance of the insulated dipole antenna is negative when:

$$f < \frac{\sqrt{3}c}{2\pi h\sqrt{\epsilon_{r4}}} \quad (\text{F.15})$$

where  $c$  is the speed of light in vacuum and  $\epsilon_{r4}$  is the relative permittivity of the ambient medium. This thus proves by example the failure of the transmission line model as proposed by Chen and Warne [4]. The formulation proposed by Smith and King [16] that is equivalent to that of Chen and Warne, given by equations 2.17 and 2.18, is hence also shown to be flawed.

In spite of all the approximations made, equation F.15 gives fairly accurate predictions of the frequency at which the numerically calculated resistance becomes negative.

Only electrical parameters of the ambient medium occurs in equation F.15, which isolates the negative resistance flaw to the expressions for  $z_4$  and  $y_4$ . The  $\frac{1}{h}$  factor in F.15 furthermore implies that this flaw in the model is only present for transmission lines of finite length. This is also suggested by the inaccuracies of the model that occur near resonant frequencies.

# Appendix G

## The scaled Wu-King impedance profile

Wu and King [31] found that a purely outward traveling current wave exists on a dipole antenna of half-length  $h$  with an internal impedance given by

$$z^i(z) = \frac{\zeta_0 \Psi}{2\pi} \frac{\alpha}{h - |z|} \quad (\text{G.1})$$

when  $\alpha = 1$ . The current distribution and input impedance of a Wu-King dipole with  $\alpha$  not equal to unity is of also interest. When the Wu-King loading distribution is scaled by a factor  $\alpha$ , the differential equation governing the current distribution on the antenna becomes

$$\left( \frac{d^2}{dz^2} + k^2 - \frac{2j\alpha k}{h - |z|} \right) I(z) = -\frac{j4\pi k}{\zeta_0 \Psi} V_0 \delta(z) \quad (\text{G.2})$$

The solutions to this differential equation are examined in an article by Shen and Wu [23]. The current distribution for  $\alpha \neq 1$  is found to be

$$I(z) = Ae^{-jkz}(h - z)\Phi[-2jk(h - z)] \quad (\text{G.3})$$

The function  $\Phi(x)$  is related to the confluent hypergeometric function  $F_1(a, b, x)$ , also known as Kummer's function of the first kind, by

$$\Phi(x) = F_1(1 - \alpha, 2, x) \quad (\text{G.4})$$

The confluent hypergeometric function is defined as

$$F_1(a, b, x) = 1 + \frac{a}{b} \frac{x}{1!} + \frac{a(a+1)}{b(b+1)} \frac{x^2}{2!} + \dots = \sum_{k=0}^{\infty} \frac{(a)_k}{(b)_k} \frac{x^k}{k!} \quad (\text{G.5})$$

where  $(a)_n = a(a+1)(a+2)\dots(a+n-1)$  is the rising factorial, also known as the Pochhammer symbol. When  $\alpha$  is a positive integer,  $\Phi(x)$  and the expression for current may hence be expressed in closed form.

From [23], the constant  $A$  is found through the relation

$$\left. \frac{dI(z)}{dz} \right|_{z=0} = -\frac{1}{2} \frac{4\pi jkV_0}{\zeta_0\Psi} \quad (\text{G.6})$$

which results in

$$A = -\frac{1}{2} \frac{4\pi jkV_0}{\zeta_0\Psi} \frac{1}{2jkh\Phi'(-2jkh) - (1 + jkh)\Phi(-2jkh)} \quad (\text{G.7})$$

where  $\Phi'(x)$  denotes the derivative of  $\Phi(x)$  with respect to  $x$ . The input impedance of an antenna with  $\alpha \neq 1$  is given by

$$Z_{in}^\alpha = V_0/I(0)$$

After substitution of the expressions for  $I(0)$  and  $A$ , and simplification

$$Z_{in}^\alpha = \frac{\zeta_0\Psi}{2\pi} \left[ 1 + \frac{1}{jkh} - 2 \frac{\Phi'(-2jkh)}{\Phi(-2jkh)} \right] \quad (\text{G.8})$$

Substituting  $\alpha = 1$  into the above equation gives the input impedance of the original unscaled Wu-King profile as calculated in [31]:

$$Z_{in} = \frac{\zeta_0\Psi}{2\pi} \left[ 1 + \frac{1}{jkh} \right] \quad (\text{G.9})$$

The expression for the original input impedance  $Z_{in}$  may be factored out of equation G.8 to find

$$Z_{in}^\alpha = Z_{in} \left[ 1 - \frac{2jkh}{1 + jkh} \frac{\Phi'(-2jkh)}{\Phi(-2jkh)} \right] \quad (\text{G.10})$$

Hence input impedance for a Wu-King profile scaled by a factor  $\alpha$  is simply that of the original Wu-King profile (for  $\alpha = 1$ ) scaled by a constant factor, as illustrated in equation G.10.

For the special cases of  $\alpha = 2$  and  $\alpha = 3$  utilized in chapter 5, we find:

$$\Phi(-2jkh) = \begin{cases} 1 + jkh, & \alpha = 2 \\ 1 + 2jkh - \frac{2}{3}(kh)^2, & \alpha = 3 \end{cases} \quad (\text{G.11})$$

$$\Phi'(-2jkh) = \begin{cases} -\frac{1}{2}, & \alpha = 2 \\ -1 - \frac{2}{3}jkh, & \alpha = 3 \end{cases} \quad (\text{G.12})$$

This gives

$$Z_{in}^{\alpha=2} = Z_{in} \left[ 1 + \frac{jkh}{(1 + jkh)^2} \right] \quad (\text{G.13})$$

$$Z_{in}^{\alpha=3} = Z_{in} \left[ 1 + \frac{2jkh}{1 + jkh} \frac{1 + \frac{2}{3}jkh}{1 + 2jkh - \frac{2}{3}(kh)^2} \right] \quad (\text{G.14})$$

# Appendix H

## A non-reflecting impedance loading profile for insulated antennas

The non-reflecting impedance loading proposed by Wu and King in their landmark 1965 paper [31] is derived for a bare antenna in free space. The profile is hence not directly applicable for the design of loading profiles for antennas in stratified media. A loading profile for a insulated dipole will hence now be derived by analogy with the derivation presented in Wu and King's 1965 paper.

A insulated dipole antenna of half-length  $h$  will be considered with a cross-sectional geometry as in figure 2.6. The dipole has a central conductor radius  $a$  and a single insulation layer with outer radius  $b$ . The second insulation layer with outer radius  $c$  shown in figure 2.6 will be considered absent for this derivation. The electrical parameters of the insulation and ambient medium is respectively labeled by indexes 2 and 4, following King and Smith's notation in [16].

The integral equation for the current on the insulated dipole, derived by Smith and King [16, Chapter 8], has the form

$$\int_{-h}^h I(z')M(z-z')dz' = E_z(a_+, z) \quad (\text{H.1})$$

where  $I(z)$  is the total axial current and the kernel  $M(z-z')$  is a complex function of the cross-sectional geometry and electrical parameters of the insulated antenna, given in [16, p. 494, eqs. 1.18]<sup>1</sup>.  $E_z(a_+, z)$  is the z-directed electric field along the surface of the conductor. Assuming that the antenna is driven by a delta-gap voltage  $V_0$  at the origin and has an internal impedance per unit length  $z^i(z)$ , the integral equation for current becomes:

$$\int_{-h}^h I(z')M(z-z')dz' = z^i(z)I(z) - V_0\delta(z) \quad (\text{H.2})$$

---

<sup>1</sup>Note that a sign error occurs in equation 1.18b

To simplify the solution to the above equation, Smith and King introduce a function  $K(z - z')$ , defined as:

$$M(z - z') = \frac{-j\zeta_2}{k_L} \left( \frac{d^2}{dz^2} + k_L^2 \right) K(z - z') \quad (\text{H.3})$$

where  $k_L$  is the yet undetermined complex propagation constant of the zeroth order current wave along the antenna. The propagation constant  $k_L$  may be determined from the transmission line theory of insulated antennas, subject to the condition  $|k_4|^2 \gg |k_2|^2$ , or numerically from the transcendental equation B.22 in appendix B. On substitution of H.3, the integral equation for the current becomes:

$$\left( \frac{d^2}{dz^2} + k_L^2 \right) \int_{-h}^h I(z') K(z - z') dz' = \frac{jk_L}{\zeta_2} [z^i(z) I(z) - V_0 \delta(z)] \quad (\text{H.4})$$

The similarity between the integral equation for current on a insulated antenna and that of a bare antenna, as in [31, eq. 1], is apparent and the derivation of a non-reflecting loading profile now parallels that presented in Wu and King's paper. A numerical study of the kernel  $K(z - z')$  [16, p. 503] shows that it has a strong peaking property near  $z = z'$ , with the consequence that a relation of form

$$\int_{-h}^h I(z') K(z - z') dz' = I(z) \Psi_S \quad (\text{H.5})$$

may be established, where  $\Psi_S$  is a complex constant. Smith and King derive an approximate expression for  $\Psi_S$  [16, eq. 414]:

$$\Psi_S = \frac{k_L}{2\pi k_2} \left[ \ln\left(\frac{b}{a}\right) + \frac{k_2^2}{k_4^2} \frac{H_2(k_4 b)}{k_4 b H_1^2(k_4 b)} \right] \quad (\text{H.6})$$

which is valid when  $|k_4|^2 \geq 2|k_2|^2$ . Substituting the relation H.5 into the integral equation, we find

$$\left( \frac{d^2}{dz^2} + k_L^2 \right) I(z) = \frac{jk_L}{\zeta_2 \Psi_S} [z^i(z) I(z) - V_0 \delta(z)] \quad (\text{H.7})$$

Following the derivation in [31], a function  $f(z)$  is defined

$$f(z) = \frac{1}{\zeta_2 \Psi_S} z^i(z) \quad (\text{H.8})$$

and on substitution into equation H.7 it follows that:

$$\left[ \frac{d^2}{dz^2} + k_L^2 - jk_L f(z) \right] I(z) = -\frac{jk_L}{\zeta_2 \Psi_S} V_0 \delta(z) \quad (\text{H.9})$$

Except at the driving point, the current on the antenna hence satisfies the differential equation

$$\left[ \frac{d^2}{dz^2} + k_L^2 - jk_L f(z) \right] I(z) = 0 \quad (\text{H.10})$$

It may be shown through direct substitution into H.10 that if

$$f(z) = \frac{2}{h - |z|} \quad (\text{H.11})$$

a solution to the current is

$$I(z) = C(h - |z|)e^{-jk_L z} \quad (\text{H.12})$$

and that solutions of the form  $e^{jk_L z}$  do not satisfy the differential equation H.10. Equation H.12 hence represents a non-dispersive current wave that travels away from the source, in the direction of increasing  $|z|$ . By the relation H.8, the impedance loading profile that gives rise this current distribution is:

$$z^i(z) = \frac{2\zeta_2 \Psi_S}{h - |z|} \quad (\text{H.13})$$

The resultant non-reflective impedance profile for insulated antennas is identical in form to that of bare antennas, in the sense that the the associated admittance  $1/z^i(z)$  decreases linearly to zero from the feed-point to  $z = h$ .

